MAGNETIC RESONANCE ELECTRICAL IMPEDANCE TOMOGRAPHY BASED ON THE SOLUTION OF THE CONVECTION EQUATION AND 3D FOURIER TRANSFORM-MAGNETIC RESONANCE CURRENT DENSITY IMAGING

A THESIS

SUBMITTED TO THE DEPARTMENT OF ELECTRICAL AND

ELECTRONICS ENGINEERING

AND THE GRADUATE SCHOOL OF ENGINEERING AND SCIENCES

OF BILKENT UNIVERSITY

IN PARTIAL FULFILLMENT OF THE REQUIREMENTS

FOR THE DEGREE OF

MASTER OF SCIENCE

By

Ömer Faruk Oran

August 2011

I certify that I have read this thesis and that in my opinion it is fully adequate, in scope and in quality, as a thesis for the degree of Master of Science.

Prof. Dr. Yusuf Ziya İder(Supervisor)

I certify that I have read this thesis and that in my opinion it is fully adequate, in scope and in quality, as a thesis for the degree of Master of Science.

Prof. Dr. Ergin Atalar

I certify that I have read this thesis and that in my opinion it is fully adequate, in scope and in quality, as a thesis for the degree of Master of Science.

Prof. Dr. Nevzat Güneri Gençer

Approved for the Graduate School of Engineering and Sciences:

Prof. Dr. Levent Onural
Director of Graduate School of Engineering and Sciences

ABSTRACT

MAGNETIC RESONANCE ELECTRICAL IMPEDANCE TOMOGRAPHY BASED ON THE SOLUTION OF THE CONVECTION EQUATION AND 3D FOURIER TRANSFORM-MAGNETIC RESONANCE CURRENT DENSITY IMAGING

Ömer Faruk Oran
M.S. in Electrical and Electronics Engineering
Supervisor: Prof. Dr. Yusuf Ziya İder
August 2011

In Magnetic Resonance Electrical Impedance Tomography (MREIT) and Magnetic Resonance Current Density Imaging (MRCDI), current is injected into a conductive object such as the human-body via surface electrodes. The resulting internal current generates a magnetic flux density distribution which is measured using a Magnetic Resonance Imaging (MRI) system. Utilizing this measured data, MREIT is the inverse problem of reconstructing the internal electrical conductivity distribution and MRCDI is the inverse problem of reconstructing a current density distribution. There are hardware and reconstruction algorithm development aspects of MREIT and MRCDI. On the hardware side, an MRI compatible constant current source is designed and manufactured. On the other side, two reconstruction algorithms are developed one for MREIT and one for MRCDI. Most algorithms for MREIT concentrate on utilizing the Laplacian of only one component of the magnetic flux density ($\nabla^2 B_z$). In this thesis, a new

algorithm is proposed to solve this $\nabla^2 B_z$-based MREIT problem which is mathematically formulated as a steady state scalar pure convection equation. Numerical methods developed for the solution of the more general convection-diffusion equation are utilized. It is known that the solution of the pure convection equation is numerically unstable if sharp variations of the field variable (in this case conductivity) exist or if there are inconsistent boundary conditions. Various stabilization techniques, based on introducing artificial diffusion, are developed to handle such cases and in the proposed algorithm the streamline upwind Petrov Galerkin (SUPG) stabilization method is incorporated into Galerkin weighted residual Finite Element Method (FEM) to numerically solve the MREIT problem. The proposed algorithm is tested with simulated and also experimental data from phantoms. It is found that for the case of two orthogonal current injections the SUPG method is beneficial when there is noise in the magnetic flux density data or when there are sharp variations in conductivity. It is also found that the algorithm can be used to reconstruct conductivity using data from only one current injection if SUPG is used. For MRCDI, a novel iterative Fourier transform based MRCDI algorithm, which utilizes one component of magnetic flux density, is developed for 3D problems. The projected current is reconstructed on any slice using $\nabla^2 B_z$ data for that slice only. The algorithm is applied to simulated as well as actual data from phantoms. Effect of noise in measurement data on the performance of the algorithm is also investigated.

Keywords: Magnetic Resonance Electrical Impedance Tomography, Magnetic Resonance Current Density Imaging, Impedance Imaging, Current Density Imaging, Current Source, Finite Element Method, Partial Differential Equations, Spatial Frequency Domain Techniques, Fourier Transform

ÖZET

TAŞINIM DENKLEMİNİN ÇÖZÜMÜNE DAYALI MANYETİK REZONANS ELEKTRİKSEL EMPEDANS TOMOGRAFİ VE 3B FOURIER DÖNÜŞÜMÜ-MANYETİK REZONANS AKIM YOĞUNLUĞU GÖRÜNTÜLEME

Ömer Faruk Oran
Elektrik ve Elektronik Mühendisliği Yüksek Lisans
Tez Yöneticisi: Prof. Dr. Yusuf Ziya İder
Ağustos 2011

Manyetik Rezonans Elektriksel Empedans Tomografisi'nde (MREET) ve Manyetik Rezonans Akım Yoğunluğu Görüntülenmesi'nde (MRAYG), iletken bir cisme (insan vücudu gibi) yüzey elektrotları vasıtasıyla akım uygulanır. İçerideki akım, Manyetik Rezonans Görüntüleme (MRG) sistemiyle ölçülen bir manyetik akı yoğunluğu oluşturur. MREET, ölçülen bu verinin kullanılarak cisim içerisindeki iletkenlik dağılımının geriçatılması ters problemidir. MRAYG ise yine ölçülen bu verinin kullanılarak cisim içerisindeki akım yoğunluğu dağılımının geriçatılması ters problemidir. MREET ve MRAYG yöntemlerinin donanım ve geriçatım algoritmaları geliştirilmesi tarafları vardır. Donanım geliştirilmesi tarafında MRG uyumlu bir sabit akım kaynağı tasarlanmış ve üretilmiştir. Diğer tarafta ise, MREET ve MRAYG yöntemleri için ayrı ayrı olmak üzere iki geriçatım algoritması geliştirilmiştir. MREET algoritmalarının birçoğu manyetik akı yoğunluğunun sadece bir bileşenine Laplas işleci uygulanması sonucu elde edilen verinin ($\nabla^2 B_z$) kullanılmasına yoğunlaşmışlardır. Bu tezde, matematiksel olarak yatışkın-durumdaki skalar ve saf taşınım denklemi şeklinde formüle edilen

$\nabla^2 B_z$-bazlı MREET probleminin çözümü için yeni bir algoritma önerilmiştir. Daha genel yayınım-taşınım denkleminin çözümü için geliştirilen nümerik yöntemler kullanılmıştır. Alan değişkeninde (bu durumda iletkenlik) keskin değişimler ya da tutarsız sınır şartları varsa saf taşınım denkleminin nümerik çözümünün kararsız olduğu bilinmektedir. Bu gibi durumlara karşı, denkleme suni yayınım katılmasına dayanan birçok kararlılaştırıcı teknik önerilmiştir ve önerilen algoritmada MREET probleminin nümerik olarak çözülmesi için Taşınım Yönünde Petrov Galerkin (TYPG) kararlılaştırıcı tekniği, Galerkin Ağırlıklı Artıklar Sonlu Elemanlar Yöntemi'ne dahil edilmiştir. Önerilen algoritma, benzetimle elde edilen verilerle ve fantomlardan alınan deney verileri ile sınanmıştır. Birbirine dik iki yönde akım uygulanması durumu incelendiğinde, manyetik akı yoğunluğu verisinde gürültü ya da iletkenlikte keskin değişikler olduğunda TYPG tekniğinin faydalı olduğu görülmüştür. Ayrıca TYPG tekniği kullanıldığında, algoritmanın tek yönde akım uygulandığında da kullanılabileceği görülmüştür. Üç boyutlu MRAYG problemleri için, manyetik akı yoğunluğunun tek bileşenini kullanan ve Fourier dönüşümüne dayalı özgün bir tekrarlamalı algoritma geliştirilmiştir. Herhangi bir kesitteki izdüşümsel akım yoğunluğu, o kesitteki $\nabla^2 B_z$ verisi kullanılarak geriçatılmıştır. Algoritma benzetimle elde edilen verilere uygulandığı gibi deney fantomlarından elde edilen gerçek verilere de uygulanmıştır. Ölçüm verilerindeki gürültünün algoritmanın performansı üzerindeki etkileri de araştırılmıştır.

Anahtar Kelimeler: Manyetik Rezonans Elektriksel Empedans Tomografi, Manyetik Rezonans Akım Yoğunluğu Görüntüleme, Empedans Görüntüleme, Akım Yoğunluğu Görüntüleme, Akım Kaynağı, Sonlu Elemanlar Yöntemi, Kısmi Türevsel Denklemler, Uzaysal Frekans Bölgesi Yöntemleri, Fourier Dönüşümü

ACKNOWLEDGMENTS

I am greatly indebted to my supervisor Prof. Dr. Yusuf Ziya İder for his invaluable guidance and encouragement throughout my M.Sc. study. We have been working together for four years now and I hope it will continue. He has been always available for a discusssion and always cared about any idea which he criticized by scientific reasoning. I especially appreciate his patience in the times when the pace of the ongoing research was slow. Undoubtedly, I am fortunate to work with an advisor like him.

I would also like to thank Prof. Dr. Ergin Atalar and to Prof. Dr. Nevzat Güneri Gençer for kindly accepting to be a member of my jury. I am grateful to Prof. Dr. Ergin Atalar also for his invaluable ideas especially about the issues regarding the magnetic resonance imaging aspect of my research. I was lucky to take a course from him about magnetic resonance imaging during my M.Sc study which helped me gain a great insight about the subject.

I want to also acknowledge Prof. Dr. Murat Eyüboğlu from Middle East Technical University. We have conducted some experiments at the METU MRI lab at the early stage of my M.Sc. study. I also want to thank Evren Değirmenci and Rasim Boyacıoğlu for their help in these experiments.

Very special thanks goes to my colleague and friend Mustafa Rıdvan Cantaş. Besides being a great friend to me, we have conducted all the experiments together and he provided me great ideas about the experimental procedures. I would also like to extend my thanks to my other office mates Necip Gürler and Fatih Süleyman Hafalır.

Last not least, I wish to express my deep gratitude to my parents for their unconditional support and patience. Also I would like to thank my sister, Elif, not only for being an excellent friend but also for being a perfect mother to my two cutest nephews.

Contents

1 INTRODUCTION **1**

1.1 Motivation 1

1.2 MRCDI and MREIT Problem Definitions 3

1.2.1 Forward Problem 3

1.2.2 Inverse Problem 4

1.3 Review of Previous Studies in MRCDI and MREIT 5

1.4 Objective and Scope of the Thesis 10

1.5 Organization of the Thesis 11

2 DATA COLLECTION SYSTEM FOR MREIT AND MRCDI 12

2.1 Measurement of B_z via an MRI Scanner 13

2.2 MR Compatible Current Source for MRCDI and MREIT 14

3 MREIT BASED ON THE SOLUTION OF THE CONVECTION EQUATION 19

3.1 Methods 19

3.1.1 The Algorithm 19

3.1.2 Simulation methods 21

3.1.3 Experimental methods 23

3.2 Results 25

3.2.1 Simulation Results 25

3.2.2 Experimental Results 30

3.3 Discussion 34

4 THREE-DIMENSIONAL FOURIER TRANSFORM MAGNETIC RESONANCE CURRENT DENSITY IMAGING (FT-MRCDI) 43

4.1 Methods 44

4.1.1 The Algorithm 44

4.1.2 Simulation and Experimental Methods 47

4.2 Simulation Results 48

4.3 Experimental Results 55

4.4 Discussion 57

5 CONCLUSIONS 61

APPENDIX 64

A Stabilization Techniques for the Solution of Convection-Diffusion Equation 64

B Triangular Mesh Based MRCDI and MREIT 68

B.1 Methods 68

B.1.1 Background Information 68

B.1.2 The Triangular Mesh Based MRCDI 69

B.1.3 The Triangular Mesh Based MREIT 71

B.1.4 Simulation and Experimental Methods 72

B.2 Results 72

B.2.1 Simulation Results 72

B.2.2 Experimental Results 74

List of Figures

2.1 The conventional MREIT pulse sequence used in the study. 14

2.2 Hardware Setup: On the left, microcontroller and power supply units which are located near MRI console are shown. The fiber-optic links which carry A and B signals from the microcontroller unit to the voltage-to-current (V/C) converter are also shown. On the right, the V/C converter which are located in the scanner room is shown with the MRI scanner. 15

2.3 Curcuit diagram for microcontroller part. G_z stands for z-gradient signal. HFBR1414 is a optical transmitter which converts electrical signals to optical signals 16

2.4 A and B signals 17

2.5 Circuit diagram for voltage-to-current converter part. R_L denotes the load resistor which is the experimental phantom in our case. HFBR2412 is a optical receiver which converts optical signals to electrical signals 18

3.1 (a) Phantom model drawn using Comsol Multiphysics. Two cylindrical regions which have different conductivity than the background are also seen. The height of the first cylindrical region is 10 cm while the height of the other cylindrical region is 8 cm. z-direction is the direction of the main magnetic field of the MRI system. (b) Picture of the experiment phantom for the first experimental setup explained in section 3.1.3. The balloon inside the phantom acts as an insulator and it isolates its inside solution from the background solution. (c) Illustration of the center transverse slice of the phantom where $z = 0$. The directions of two orthogonal current injection profiles are also shown. 22

3.2 Figures at the central slice of the simulation phantom: (a) simulated $\nabla^2 B_z$, (b) actual conductivity distribution, (c) quiver plot of the actual difference current density distribution ($x-$ and $y-$ components), (d) quiver plot of the reconstructed $\mathbf{J}^*$ 26

3.3 Reconstructed conductivity in the simulations: (a) the reconstructed conductivity distribution at the center slice, (b) the reconstructed conductivity profile on the $x = y$ line at the center slice. (a) and (b) are obtained when a single current injection is used without stabilization. (c) and (d) are same as (a) and (b) but with the SUPG stabilization applied in the solution. (e) and (f) are same as (a) and (b) but when two current injections are utilized without stabilization. 28

3.4 Reconstructed conductivity in the simulations when conductivity change is sharp: (a) reconstructed conductivity distribution at the center slice, (b) the reconstructed (solid line) and actual (broken line) conductivity profiles on the $x = y$ line at the center slice. . . 29

3.5 Simulation results for the evaluation of the performance of the algorithm against noise: (a) Noisy $\nabla^2 B_z$ for $SNR = 180$ and $T_C = 50ms$, (b) Quiver plot of calculated $\mathbf{J}^*$ using noisy $\nabla^2 B_z$, (c) reconstructed conductivity distribution at the center slice, (d) reconstructed conductivity profile on the $x = y$ line at the center slice. (c) and (d) are obtained when no stabilization is applied. (e) and (f) are same with (c) and (d) but with SUPG stabilization applied. 31

3.6 Input data and the reconstructed current densities for the first experimental setup explained in Section 3.1.3. (a) and (b) are $\nabla^2 B_z$ calculated from the measured B_z for two current injections respectively, (c) and (d) are filtered versions of $\nabla^2 B_z$ given in (a) and (b), (e) and (f) are the quiver plots of calculated $\mathbf{J}^*$ for the two current injections respectively 33

3.7 Reconstructed conductivity distributions for the first experimental setup explained in Section 3.1.3. (a) reconstructed conductivity distribution at the center slice of the phantom, (b) reconstructed conductivity profile on the $x = y$ line at the center slice. (a) and (b) is obtained when the original $\nabla^2 B_z$ (no filter) is used without stabilization. (c) and (d) are same with (a) and (b) but the filtered $\nabla^2 B_z$ is used without stabilization. (e) and (f) are same with (a) and (b) but the original $\nabla^2 B_z$ (no filter) is used with the SUPG stabilization. (g) and (h) are same with (a) and (b) but the filtered $\nabla^2 B_z$ is used with the SUPG stabilization 35

3.8 Results for the second experimental setup explained in Section 3.1.3). (a) and (b) are $\nabla^2 B_z$ calculated from the measured B_z for two current injections respectively. $\nabla^2 B_z$ is multiplied with a cosine window in the frequency domain ($k_{max} = 300m^{-1}$). (c) the reconstructed conductivity distribution at the center slice when no stabilization is used (d) the reconstructed conductivity distribution at the center slice when SUPG stabilization is used 36

4.1 Magnitudes of inverse filters: (a) $-\frac{1}{2\pi} j k_y \frac{1}{k_x^2+k_y^2}$ (b) $-\frac{1}{2\pi} j k_x \frac{1}{k_x^2+k_y^2}$. 46

4.2 Simulation results for the 3D FT-MRCDI: (a) initial $\nabla^2 B_z$ (input to the algorithm), (b) $\nabla^2 B_z$ reconstructed at the tenth iteration, (c, d) quiver plot of the reconstructed $\mathbf{J}^*$ at the first and tenth iterations respectively, (e, f) magnitude of the reconstructed $\mathbf{J}^*$ at the first and tenth iterations respectively (The region inside the object is nulled to emphasize the decrease of the magnitude outside the object throughout the iterations). 50

4.3 The L^2-error made in the reconstruction of $\mathbf{J}^*$ and the ϕ ratio as iterations proceed for two different simulation cases. (a) and (b) are drawn for the first simulation case explained in Section 3.1.2. (c) and (d) are drawn for the simulation case in which the non-zero regions of $\nabla^2 B_z$ is closer to the boundary. 51

4.4 Conductivity distribution((a)) and the quiver plot of actual difference current density((b)) for the simulation case in which the non-zero regions of $\nabla^2 B_z$ is closer to the boundary. 52

4.5 Simulation results for the 3D FT-MRCDI when the non-zero regions of $\nabla^2 B_z$ is closer to the boundary : (a) initial $\nabla^2 B_z$ (input to the algorithm), (b) $\nabla^2 B_z$ reconstructed at the tenth iteration, (c, d) quiver plot of the reconstructed $\mathbf{J}^*$ at the first and tenth iterations respectively, (e, f) magnitude of the reconstructed $\mathbf{J}^*$ at the first and tenth iterations respectively (The region inside the object is nulled to emphasize the decrease of the magnitude outside the object throughout the iterations). 53

4.6 Simulation results for the 3D FT-MRCDI when noise is added to $\nabla^2 B_z$: (a) initial $\nabla^2 B_z$ (input to the algorithm), (b) $\nabla^2 B_z$ reconstructed at the tenth iteration, (c, d) quiver plot of the reconstructed $\mathbf{J}^*$ at the first and tenth iterations respectively, (e, f) magnitude of the reconstructed $\mathbf{J}^*$ at the first and tenth iterations respectively (The region inside the object is nulled to emphasize the decrease of the magnitude outside the object throughout the iterations). 54

4.7 Experimental results for the first experimental setup: (a) initial $\nabla^2 B_z$ (input to the algorithm), (b) $\nabla^2 B_z$ at the eighth iteration, (c, d) quiver plot of the reconstructed $\mathbf{J}^*$ at the first and eighth iterations respectively, (e, f) magnitude of the reconstructed $\mathbf{J}^*$ at the first and eighth iterations respectively (The region inside the object is nulled to emphasize the decrease of the magnitude outside the object throughout the iterations). 56

4.8 The iteration number versus the ϕ ratio: (a) the first experimental setup, (b) the second experimental setup. 57

4.9 Experimental results for the second experimental setup: (a) initial $\nabla^2 B_z$ (input to the algorithm), (b) $\nabla^2 B_z$ at the seventh iteration, (c, d) quiver plot of the reconstructed $\mathbf{J}^*$ at the first and seventh iterations respectively, (e, f) magnitude of the reconstructed $\mathbf{J}^*$ at the first and seventh iterations respectively (The region inside the object is nulled to emphasize the decrease of the magnitude outside the object throughout the iterations). 58

A.1 The solution of equation (A.2): (a) $\beta = 1$, $k = 0$ and $u(0) = 0$, $u(1) = 1$ (b) $\beta = 1$, $k = 0$ and $u(0) = 0$, $u(1) = 0$ (c) $\beta = 1$, $k = 1/194$ and $u(0) = 0$, $u(1) = 0$ (d) $\beta = 1$, $k = 10/194$ and $u(0) = 0$, $u(1) = 0$ 67

B.1 Simulation results for the triangular mesh based MRCDI: (a) simulated $\nabla^2 B_z$, (b) quiver plot of the actual difference current density distribution ($x-$ and $y-$ components), (c) quiver plot of the $\mathbf{J}^*$ reconstructed using the method proposed by Park *et al.* , (d) quiver plot of the $\mathbf{J}^*$ reconstructed using the triangular mesh based MRCDI method. 73

B.2 Reconstructed conductivities using triangular mesh based MREIT in the simulations: (a) the reconstructed conductivity distribution at the center slice, (b) the reconstructed conductivity profile on the $x = y$ line at the center slice. (c) and (d) are same as (a) and (b) but reconstructions are made with noisy $\nabla^2 B_z$ ($SNR = 180$ and $T_C = 50ms$). 75

B.3 Simulation results for the evaluation of the performance of the triangular mesh based MRCDI against noise: (a) Noisy $\nabla^2 B_z$ for $SNR = 180$ and $T_C = 50ms$, (b) quiver plot of $\mathbf{J}^*$ reconstructed using the method proposed by Park *et al.* from noisy $\nabla^2 B_z$, (c) quiver plot of the $\mathbf{J}^*$ reconstructed using the triangular mesh based MRCDI method from noisy $\nabla^2 B_z$. 76

B.4 Experimental results for the first experiment setup explained in Section 3.1.3: (a) and (b) are quiver plots of $\mathbf{J}^*$ at the center slice reconstructed using the triangular mesh based MRCDI method from noisy $\nabla^2 B_z$ for two current injection directions respectively, (c) is the conductivity distribution at the center slice reconstructed using the triangular mesh based MREIT. 78

B.5 Experimental results for the second experiment setup explained in Section 3.1.3: (a) and (b) are quiver plots of $\mathbf{J}^*$ at the center slice reconstructed using the triangular mesh based MRCDI method from noisy $\nabla^2 B_z$ for two current injection directions respectively, (c) is the conductivity distribution at the center slice reconstructed using the triangular mesh based MREIT. 79

List of Tables

1.1 Typical electrical conductivities of some biological tissues at low frequencies (reproduced from [4]) 2

Chapter 1

INTRODUCTION

1.1 Motivation

In Magnetic Resonance Electrical Impedance Tomography (MREIT), electrical current is injected into a conductive object such as the human-body via surface electrodes. The resulting internal current generates a magnetic flux density distribution both inside and outside the object. The magnetic flux density inside the object is measured using a Magnetic Resonance Imaging (MRI) system, and from this measured magnetic flux density distribution, the internal electrical conductivity distribution of the object is reconstructed.

Imaging electrical conductivity distribution of biological tissues has been an active research area in the field of medical imaging for decades. Electrical conductivity greatly varies in different tissues of human body since each tissue has different cell concentration, cellular structure, membrane capacitance, and so on [1]-[3]. Electrical conductivity of human tissues is also a function of the frequency of the applied current. In MREIT and MRCDI, very low frequencies are considered (less than 1 kHz) and therefore effects of permittivity is ignored and only

conductivity is considered. Typical electrical conductivities of different biological tissues at low frequencies are given Table 1.1 [4].

The conductivity distribution provides both an anatomical image and a different contrast mechanism. More importantly, the electrical conductivity also depends on the pathological state of the tissues which means the electrical conductivity imaging can be used for detection and characterization of, for instance, tumors [5]-[7].

Similar to MREIT, in Magnetic Resonance Current Density Imaging (MRCDI), the magnetic flux density due to injected currents is measured via an MRI system. The internal current density distribution is then reconstructed using this data. MRCDI is strictly related to MREIT in the sense that some MREIT algorithms require the current density distribution to be known and in other algorithms the current density may be calculated once the conductivity is obtained. Besides being a companion problem to MREIT, MRCDI itself has also potential medical applications [8]-[15]. There are many therapeutic techniques in which currents are injected to the body (e.g. cardiac defibrillation and pacing, electrocautery, and some treatment methods in physiotherapy). Knowledge of current density distribution would be useful in planning and designing such therapeutic techniques.

Table 1.1: Typical electrical conductivities of some biological tissues at low frequencies (reproduced from [4])

Tissue	Frequency (kHz)	Conductivity (S/m)
Cerebrospinal fluid (human)	1	1.56
Blood (human)	DC	0.67
Plasma (human)	DC	1.42
Skeletal muscle (longitudinal fibers) (human)	DC	0.41
Skeletal muscle (transverse fibers) (human)	0.1	0.15
Fat (dog)	0.01	0.04
Bone (human)	0.1	0.00625

1.2 MRCDI and MREIT Problem Definitions

1.2.1 Forward Problem

Let Ω be a connected and bounded domain in $\mathbb{R}^3$ representing the internal region of a three-dimensional electrically conducting object in which the electrical current density and the conductivity distribution is to be imaged. DC current of magnitude I is applied between two electrodes attached on the boundary of the domain which is denoted by $\partial\Omega$. The electric potential, $\phi(x, y, z)$, dictated by the current injection satisfies the boundary-value problem with Neumann boundary condition which is given as

$$\begin{aligned} \nabla \cdot \sigma \nabla \phi(x, y, z) &= 0 \text{ in } \Omega \\ \sigma \frac{\partial \phi}{\partial \mathbf{n}} &= g \text{ on } \partial\Omega \end{aligned} \tag{1.1}$$

where σ is the electrical conductivity, $\mathbf{n}$ is the unit outward normal along the boundary $\partial\Omega$, $\int_{\mathcal{E}_\pm} g \, \mathrm{d}s = \pm \mathrm{I}$ on electrodes ($\mathcal{E}_\pm$ denotes one of the electrodes on $\partial\Omega$ and sign depends on whether current is injected through or sunk from the electrode considered), and $g = 0$ on $\partial\Omega$ other than electrodes. The current density, $\mathbf{J}$, is given by $\mathbf{J} = \sigma\mathbf{E}$ where $\mathbf{E} = -\nabla\phi$ is the electric field. Once the problem given by Equation 1.1 is solved for electric potential, it easy to calculate the current density distribution.

In MREIT and MRCDI, currents of very low frequency are injected into the imaging object and therefore static version of Maxwell's equations are used. In the static assumption, the displacement current, $\frac{\partial \mathbf{D}}{\partial t}$, and the magnetic induction, $\frac{\partial \mathbf{B}}{\partial t}$, are negligible. Therefore $\mathbf{J} = \nabla \times \mathbf{B}/\mu_0$ and $\nabla \times \mathbf{E} = \mathbf{0}$.

The magnetic flux density generated by the current density distribution in Ω is given by *Biot-Savart* law as

$$\mathbf{B}(\mathbf{r}) = \frac{\mu}{4\pi} \int_\Omega \mathbf{J}(\mathbf{r}) \times \frac{\mathbf{r} - \mathbf{r}'}{|\mathbf{r} - \mathbf{r}'|^3} \, \mathrm{d}\mathbf{r}' \tag{1.2}$$

where $\mathbf{B}(\mathbf{r})$ is the generated magnetic flux density, $\mathbf{r}$ is the position vector in $\mathbb{R}^3$, and μ is the magnetic permeability which can be assumed to be space-invariant and has the free space value of $\mu_0 = 4\pi \times 10^{-7}$ H/m for body tissues.

Given the conductivity distribution in Ω, the object and boundary geometry, and the electrode configuration, the forward problem of MRCDI and MREIT is the calculation of the magnetic flux density which is generated by the internal current density. The internal current density distribution is calculated from the electric potential which is the solution of Equation 1.1. The solution of forward problem is necessary for the generation simulated data which are used to test the developed algorithms. Furthermore, as will be discussed in Section 1.3, some MRCDI and MREIT algorithms, including the MREIT algorithm proposed in this thesis, requires the solution of the current density distribution when homogeneous conductivity is assumed in Ω.

1.2.2 Inverse Problem

The inverse problem of MRCDI is the reconstruction of the current density from the measured magnetic flux density. Some early MRCDI algorithms assume that all components of the magnetic flux density are measured. However, as will be discussed in Section 1.3, measurement of all components of the magnetic flux density is impractical, and therefore currently most MRCDI algorithms utilize only one component of the magnetic flux density, namely B_z, if main magnetic field of the MRI scanner is assumed to be the z- direction. B_z is generated only by transverse (x- and y- components) current density and the relation given in Equation 1.2 is written only for B_z as

$$B_z(x,y,z) = \frac{\mu_0}{4\pi} \int_{\Omega} \frac{(y-y')J_x(x',y',z') - (x-x')J_y(x',y',z')}{[(x-x')^2 + (y-y')^2 + (z-z')^2]^{(3/2)}} \mathrm{d}x'\mathrm{d}y'\mathrm{d}z'. \quad (1.3)$$

On the other hand, the inverse problem of MREIT is the reconstruction of the conductivity distribution from the measured magnetic flux density. Some early MREIT algorithms assume that that all components of the magnetic flux density are measured and all components of the current density are calculated from Ampere's Law ($\mathbf{J} = \nabla \times \mathbf{B}/\mu_0$) so that the inverse problem of MREIT reduces to reconstruction of the conductivity from the current density. These algorithms often called **J**-based MREIT algorithms. Recently most algorithms utilize only B_z, which are often called B_z-based MREIT algorithms.

Although some B_z-based MREIT problems directly utilize B_z data, other algorithms use the Laplacian of B_z ($\nabla^2 B_z$). Taking the curl of both sides of Ampere's Law ($\mathbf{J} = \nabla \times \mathbf{B}/\mu_0$), and using the vector identity $\nabla \times \nabla \times \mathbf{B} = \nabla(\nabla \cdot \mathbf{B}) - \nabla^2 \mathbf{B}$ together with the fact that $\nabla \cdot \mathbf{B} = 0$, the following expression, which relates the x- and y- components of the current density distribution to $\nabla^2 B_z$, is obtained [8]:

$$\frac{\partial J_x}{\partial y} - \frac{\partial J_y}{\partial x} = \frac{\nabla^2 B_z}{\mu_0} \tag{1.4}$$

Since current density is given by $\mathbf{J} = \sigma \mathbf{E}$ and $\nabla \times \mathbf{E} = 0$, we also have

$$\frac{1}{\sigma}(J_x \frac{\partial \sigma}{\partial y} - J_y \frac{\partial \sigma}{\partial x}) = \frac{\nabla^2 B_z}{\mu_0} \tag{1.5}$$

For the $\nabla^2 B_z$-based MREIT algorithms, the inverse problem is the reconstruction of the conductivity using the relation given in Equation 1.5.

1.3 Review of Previous Studies in MRCDI and MREIT

MRCDI was introduced in 1989 by Joy *et al.* [16]. In their study, by physically rotating the experiment phantom inside the MRI scanner, they measured all components of the magnetic flux density generated by the injected current. Since only the component of the magnetic flux density parallel to the direction of the

main magnetic field of the MRI scanner can be measured at one time, object rotations are necessary for measuring all components of the magnetic flux density. The current density distribution was calculated from Ampere's Law ($\mathbf{J} = \nabla \times \mathbf{B}/\mu_0$). As an experiment phantom, they prepared two isolated cylindrical tubes one within the other and both tubes were filled with electrolyte. The current was applied between two ends of the inner tube and a uniform current flowing only in one direction was obtained. Later in 1991, Scott *et al.* used a similar procedure to reconstruct nonuniform current density flowing in all directions [8]. One year later, Scott *et al.* published their study in which they investigated the sensitivity of MRCDI to both random noise and systematic errors [17]. There are some other investigators who have also measured all components of the magnetic flux density and utilized Ampere's Law to reconstruct the current density. In 1998, Eyüboğlu *et al.* [18] reported that they have reconstructed current density magnitude of which is lower than the current density reconstructed by Scott *et al.* . Also they reconstructed the current density in a slice more close to the electrodes. They used a similar experimental phantom that was used by Scott *et al.* in 1991. Other studies may be listed as applications of the MRCDI procedure proposed by Joy *et al.* [8]-[15].

In practice, rotating the object inside an MRI scanner is not desirable because of possible misalignments after the rotation. Furthermore, for long objects, subject rotations are in fact impossible in a conventional closed bore MRI system. Last not least, since the experiment must be repeated three-times in order to measure all three components of the magnetic flux density, total scan time becomes three times higher. Therefore most MRCDI and MREIT algorithms use only one component of the measured magnetic flux density, namely B_z, where z- direction is the direction of the main magnetic field of the MRI scanner. It was shown by Park *et al.* that the transverse current density distribution cannot be fully recovered using only B_z information unless the difference between the z-components of the actual current density and the current density calculated for

homogeneous conductivity is negligible [19] . Nevertheless, in their study, Park *et al.* have also developed an algorithm by which J_x and J_y distributions can be estimated for a certain slice given the $\nabla^2 B_z$ data for that slice. They have called this estimated transverse current density the "projected current density" which is the recoverable portion of the actual current density.

Besides spatial domain MRCDI algorithms, some frequency domain techniques for MRCDI is also suggested [20]-[22]. İder *et al.* have developed Fourier Transform (FT)-based MRCDI algorithms utilizing only B_z for two- and three-dimensional problems [22]. For two-dimensional problems where the current density has no z- component, the proposed algorithm iteratively reconstructs both the current density on an xy- plane inside the object and also the magnetic flux density on the same xy- plane outside the object. For three-dimensional problems, another algorithm has been developed in the same study by which the "projected current density" at any desired slice is iteratively reconstructed from the $\nabla^2 B_z$ data for that slice. The algorithm for three-dimensional case is named "3D Fourier Transform-Magnetic Resonance Current Density Imaging (FT-MRCDI)" and the work done for this thesis also includes the algorithm developed for 3D FT-MRCDI which is discussed in Chapter 4.

As indicated in Section 1.1, MRCDI and MREIT are companion problems such that in many MREIT algorithms current density is also reconstructed. In the following, some MREIT algorithms will be discussed in which the current density is reconstructed as a part of the algorithm or may be reconstructed as an additional information once the conductivity is reconstructed. The MREIT algorithms fall into two categories which are **J**-based and B_z-based algorithms respectively. While early MREIT algorithms are members of the first group, recently most MREIT algorithms are members of the latter group.

In **J**-based MREIT algorithms, all components of the magnetic flux density is measured from which **J** is calculated using Ampere's Law. These algorithms concentrate on reconstructing the conductivity distribution from the reconstructed current density. In 1992, Zhang proposed the first **J**-based MREIT algorithm in his MSc thesis and so the MREIT concept was first introduced [23]. Apart from this study, the MREIT concept is also introduced by Woo *et al.* [24] in 1994, and by Birgul and İder [25] in 1995 independently. These two studies also involve **J**-based algorithms. Other **J**-based algorithms are given in [26]-[31].

On the other hand, B_z-based MREIT algorithms provide us with the ability to reconstruct the conductivity distribution using only B_z which is advantageous over **J**-based algorithms since impractical object rotations are not needed. Therefore, today, most MREIT algorithms fall into category of B_z-based MREIT algorithms.

In 1995, Birgul and İder proposed the first B_z-based algorithm [25]. They formed a sensitivity matrix in order to linearize the relation between the conductivity and B_z which is given by Equations 1.1 and 1.3 considering the fact that $\mathbf{J} = -\sigma\nabla\phi$. The obtained sensitivity matrix is inverted using truncated singular value decomposition. They have published simulation results [32] and the experimental results are given in [33] for the proposed sensitivity matrix based MREIT algorithm.

As mentioned in Section 1.2.2, some B_z-based MREIT algorithms utilize the Laplacian of B_z ($\nabla^2 B_z$) in which $\nabla^2 B_z$ is calculated from the measured B_z before the reconstruction algorithm starts. The relation between the conductivity (σ), current density (**J**) and the Laplacian of B_z ($\nabla^2 B_z$) was given in Equation 1.5. If J_x and J_y are known for a certain slice (intersection of the object with a certain $z = constant$ plane) then the transverse gradient of the conductivity, $(\frac{\partial\sigma}{\partial x},\ \frac{\partial\sigma}{\partial y})$, can be calculated from the $\nabla^2 B_z$ data obtained for that slice only. This is the major advantage of $\nabla^2 B_z$-based algorithms because reconstruction

of conductivity at a certain slice is possible so that measuring B_z in the whole domain is not necessary. If the electric potential (ϕ) is used, Equation 1.5 may be written as

$$\frac{\partial \sigma}{\partial x}\frac{\partial \phi}{\partial y} - \frac{\partial \sigma}{\partial y}\frac{\partial \phi}{\partial x} = \frac{\nabla^2 B_z}{\mu_0}. \tag{1.6}$$

In 2003, Seo *et al.* proposed a $\nabla^2 B_z$-based iterative algorithm which depends on the solution of the above equation [34]. For the first iteration, they assumed a homogeneous conductivity and solved the forward problem to find electric potential and they used this electric potential to solve Equation 1.6 for the gradient of the conductivity in each MR pixel. They used two orthogonal current injections to obtain a unique solution. For the calculation of the conductivity from its gradient, they utilized a line integral method. The newly calculated conductivity is used for the next iteration and the iterations stop if the change in the conductivity for the consecutive iterations is sufficiently small. Oh *et al.* used the same algorithm with the difference that they utilized a layer potential technique to calculate the conductivity distribution from its gradient [35]. They called this algorithm as "Harmonic B_z algorithm".

In 2004, İder and Onart modified Equation 1.5 to obtain

$$\nabla^2 B_z = \mu_0 (J_x \frac{\partial R}{\partial y} - J_y \frac{\partial R}{\partial x}) \tag{1.7}$$

where $R = \ln \sigma$ [36]. They proposed an iterative algorithm based on the above equation. For the first iteration, they assumed a homogeneous conductivity and solved for the current density. Next, they used the finite difference approximation to obtain a matrix system for the solution of R. Upon the solution of the matrix system, R is obtained directly in each pixel. They used this R in the next iteration and the iterations stop if the change in R for the consecutive iterations are sufficiently small.

In 2008, Nam *et al.* used the "projected current density" [19] in Equation 1.7 to find the transverse gradient of R in each pixel at the slice of interest [37]. Starting from the gradient distribution, they utilized a layer potential technique,

suggested by Oh *et al.* [35], to reconstruct the conductivity distribution on that slice.

1.4 Objective and Scope of the Thesis

This thesis covers the research regarding both the hardware and the algorithm development aspects of MREIT and MRCDI. As mentioned previously, for MREIT and MRCDI, currents are injected through surface electrodes into the imaging object which requires an MRI compatible constant current source. Therefore, on the hardware side, a current source which is used for injecting currents in the experiments is designed and developed.

On the other hand, we have developed two new reconstruction algorithms one for MREIT and one for MRCDI. For MREIT, the devoloped algorithm is named *MREIT based on the solution of the convection equation*. In this algorithm, the relation which is given in Equation 1.7 is put into the form of the steady-state scalar convection equation. Convection equation is a special case of the more general convection-diffusion equation and describes the distribution of a physical quantity (e.g. concentration, temperature) under the effect of two basic mechanisms, convection and diffusion. The convection-diffusion equation arises in many physical phenomena such as distribution of heat, fluid dynamics etc. Although physically no convection mechanism exists in the MREIT problem, it can nevertheless be handled as a convection problem solely from a mathematical point of view. Furthermore, because the convection equation by itself does not always yield stable numerical solutions, introduction of a diffusion term as a stabilization technique is customary. Therefore, in *MREIT based on the solution of the convection equation*, the MREIT problem is handled as a convection-diffusion problem and the advanced numerical methods developed for the solution of the convection-diffusion equation by using finite element method (FEM) are

adapted and used for solving the MREIT problem. The methods are then tested both with simulated and experimental data.

For MRCDI, a spatial frequency domain based MRCDI algorithm which is named *Three-dimensional Fourier transform MRCDI*, is developed. In this algorithm, in a imaging slice, Equation 1.4 and divergence-free condition of the current density is utilized together in the frequency domain. To our knowledge, the proposed algorithm is the only frequency domain MRCDI algorithm for 3D problems. The results obtained from both the simulated data and the experimental data are presented.

Noise is inherent in the actual B_z measurements. Therefore it is important to evaluate the performance of any reconstruction algorithm for MREIT or MRCDI. In this thesis, we also provide simulation results for both developed MREIT and MRCDI algorithms when random noise is added to the simulated $\nabla^2 B_z$.

1.5 Organization of the Thesis

This thesis consists of five chapters. Chapter 2 discusses the designed data collection system for MREIT and MRCDI. In this chapter, the MRI pulse sequence, which is used for measuring magnetic flux density due to the injected currents is discussed. Also the designed current source is described. Chapter 3 and 4 discusses the developed *MREIT based on the solution of the convection equation* algorithm and *Three-dimensional Fourier transform MRCDI* algorithms respectively. The simulation and experimental methods and the results obtained using these methods are given in each chapter in order to evaluate the performance of the proposed algorithms. Finally, Chapter 5 provides conclusions to the thesis.

Chapter 2

DATA COLLECTION SYSTEM FOR MREIT AND MRCDI

In MRCDI and MREIT, an MRI scanner is used to measure the magnetic flux density distribution due to the injected currents. It is known that an MRI system is only sensitive to the transverse magnetization and only z- component of the generated magnetic flux density can effect transverse magnetization by providing additional phase to the spins (z- direction is the direction of the main magnetic field of the MRI scanner). Therefore only z- component of the generated magnetic flux density, namely B_z, can be measured at one time, and we will discuss measurement of only B_z in this chapter. It is important to remind that, in order to measure other components of the generated magnetic flux density, the imaging object could be rotated inside the MRI scanner. However, in practice, object rotations are impractical as discussed in Chapter 1.

2.1 Measurement of B_z via an MRI Scanner

In order to measure B_z via an MRI scanner, several MRI pulse sequences is proposed [16], [38]-[43]. In this study, the conventional spin-echo MREIT pulse sequence proposed by Joy *et al.* [16] is used. The timing diagram of the sequence is given in Figure 2.1. As evident from Figure 2.1, the imaging slice is transversal and so B_z is measured in a transversal slice, although sagittal and coronal slices are possible. Two acquisitions are required in which positive and negative current injections are used separately. The complex k-space data obtained using this pulse sequence can be written for positive and negative current injections as

$$\begin{aligned}\mathcal{S}^{\pm}(m,n) = \int\limits_{R^2} M(x,y)\exp\left(j\delta(x,y)\right)\exp\left(\pm j\gamma B_z(x,y)T_c\right) \\ \exp\left(-j2\pi(m\Delta k_x x + n\Delta k_y y)\right)\mathrm{d}x\mathrm{d}y\end{aligned} \tag{2.1}$$

where $M(x,y)$ is the transverse magnetization which is a function of spin density and T_1, T_2 decay constants, $\delta(x,y)$ is the systematic phase artifact in radians, γ is the gyromagnetic ratio (26.7519×10^7 rad/T s), B_z is the z- component of the magnetic flux density due to the injected current, T_c is the total current injection time and k_x, k_y are the spatial frequency components in x- and y- directions. Two complex images for positive and negative current injections, which can be obtained from $\mathcal{S}^{\pm}(m,n)$ using two-dimensional discrete inverse Fourier transform (DFT), are given as

$$\mathcal{M}^{\pm}(x,y) = M(x,y)\exp\left(j\delta(x,y)\right)\exp\left(\pm j\gamma B_z(x,y)T_c\right). \tag{2.2}$$

The phases of two images in radians are

$$\Phi_1 = \delta(x,y) + \gamma B_z(x,y)T_c \text{ and } \Phi_2 = \delta(x,y) - \gamma B_z(x,y)T_c. \tag{2.3}$$

from which B_z can be calculated by subtracting phases to eliminate $\delta(x,y)$ and dividing by two ($B_z(x,y) = (\Phi_1 - \Phi_2)/(2\gamma T_c)$). Note that the obtained phase images are most likely wrapped and in order to unwrap the phase images, Goldstein's phase unwrapping algorithm is used in this study [44].

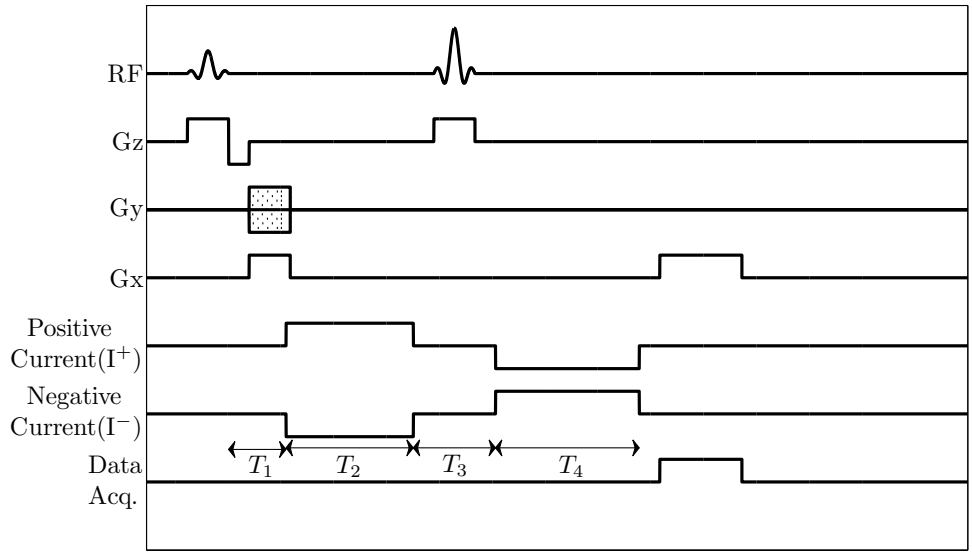

Figure 2.1: The conventional MREIT pulse sequence used in the study.

2.2 MR Compatible Current Source for MR-CDI and MREIT

In MRCDI and MREIT modalities, an MRI compatible constant current source is required to inject currents into the subject through surface electrodes. The required current waveform is given in Figure 2.1. The current injection cycle starts T_1 milliseconds after the 90° RF excitation pulse. Therefore the current source must be triggered by the MRI system to indicate the location of the excitation RF pulse in time. Once triggered by the MRI system, the current source must apply currents with respect to T_1, T_2, T_3 and T_4 as shown in Figure 2.1. Since T_E can be differently selected for each experiment, T_1-T_4 is not constant and the current source must be designed such that these values is entered for each experiment.

In this study, a current source system which has above specifications is designed and implemented for the MRCDI and MREIT experiments. The designed

system has three parts (each part placed in a different box), namely power supply, microcontroller, and voltage-to-current converter (Figure 2.2).

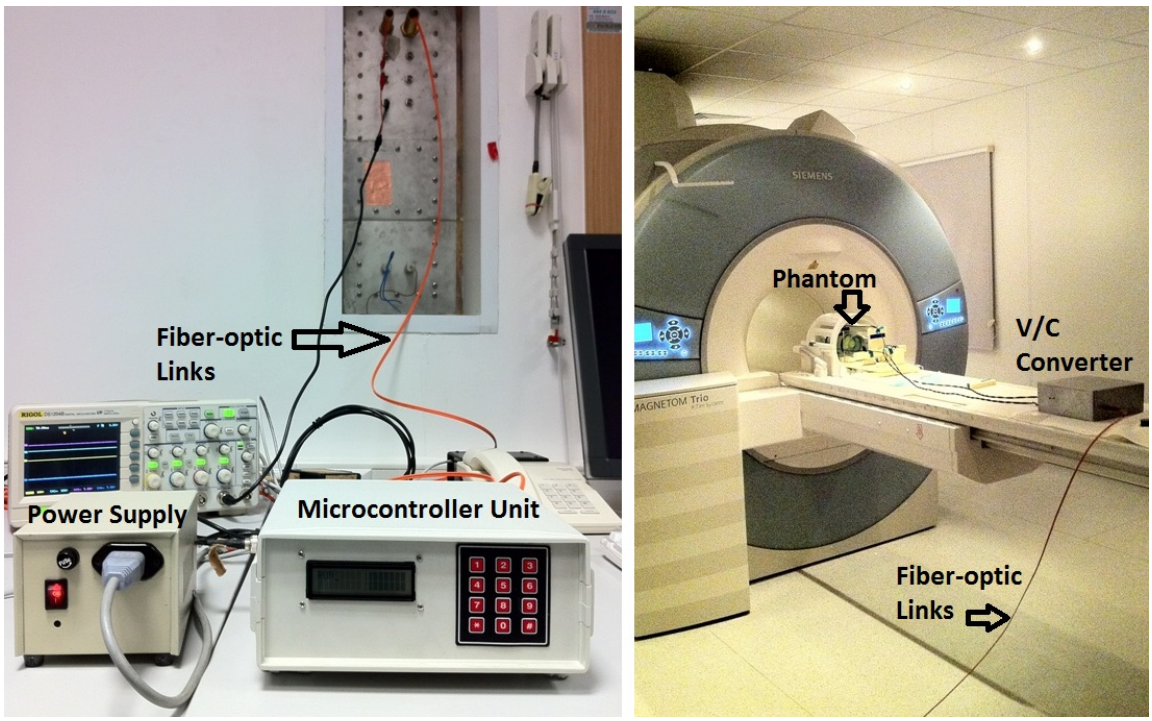

Figure 2.2: Hardware Setup: On the left, microcontroller and power supply units which are located near MRI console are shown. The fiber-optic links which carry A and B signals from the microcontroller unit to the voltage-to-current (V/C) converter are also shown. On the right, the V/C converter which are located in the scanner room is shown with the MRI scanner.

The circuit diagram for the microcontroller part is given in Figure 2.3. The microcontroller part mainly produces A and B signals (Figure 2.4) which are then sent to the current source box via fiber-optic links. The required trigger is taken from the negative edge at the onset of the refocusing pulse of the z-gradient, which is the only negative part in the z-gradient signal as shown in Figure 2.1. The z-gradient signal is isolated from the microcontroller box circuit by using a linear optocoupler such that the gradient signal on the isolated side is transferred to the non-isolated side with a DC offset. The isolated side of the circuit operates at ± 12 V obtained from lead-acid batteries whereas the non-isolated part operates at ± 15 V and 8 V obtained from the power supply part. Once the signal is transferred to the non-isolated part, the signal is entered to a

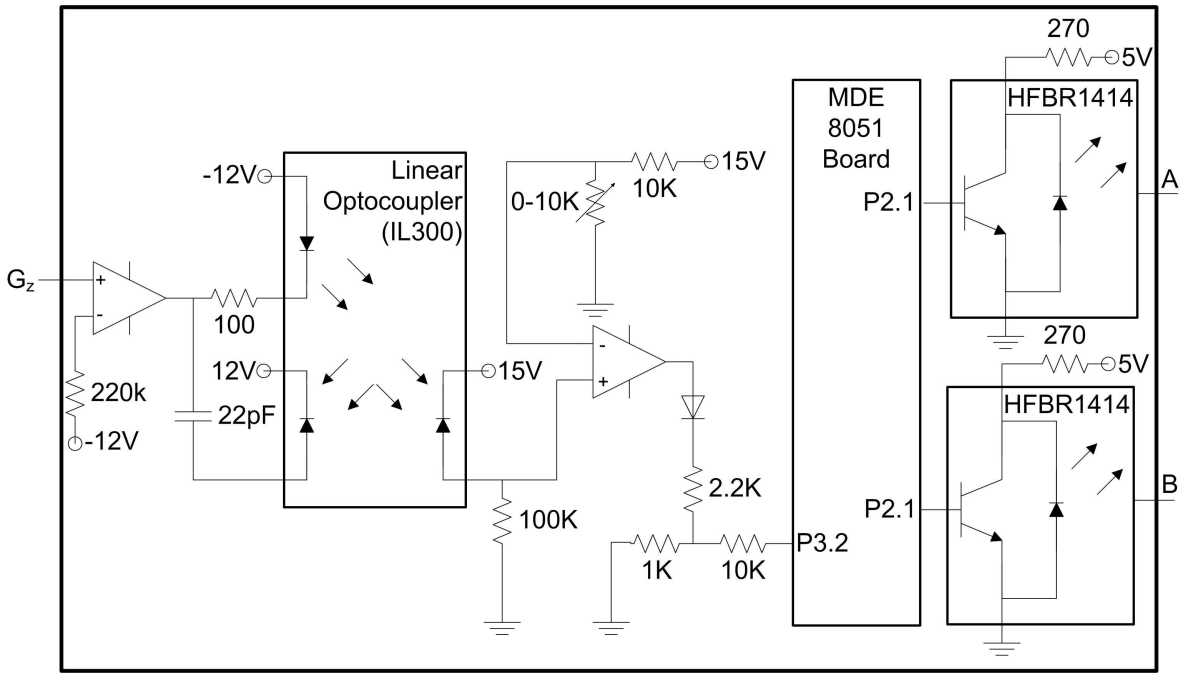

Figure 2.3: Curcuit diagram for microcontroller part. G_z stands for z-gradient signal. HFBR1414 is a optical transmitter which converts electrical signals to optical signals

comparator such that another signal, which becomes 15 V during the refocusing part of the gradient signal and stays at -15 V otherwise, is produced. This signal is input to the interrupt port of the microcontroller board after eliminating the negative part with a diode and the signal level is decreased by a voltage-divider circuit. The microcontroller board consists of a 8051 microcontroller and driving circuitry. The board is programmed to produce A and B signals with respect to the T_1-T_4 which are entered with the help of a numpad and an LCD. A and B signals are sent to the voltage-to-current converter part by using digital optical transmitters (Avago Technologies, HFBR 1414). The circuit diagram for the voltage-to-current converter part is given in Figure 2.5 where R_L represents the phantom. The voltage-to-current converter part converts optical A and B signals into the electrical signals and then subtracts B from A to obtain the desired current injection waveform as a voltage as shown in Figure 2.4. This voltage waveform is then converted to the current waveform via a simple opamp circuit. The magnitude of the current may be adjusted with the resistor at the negative

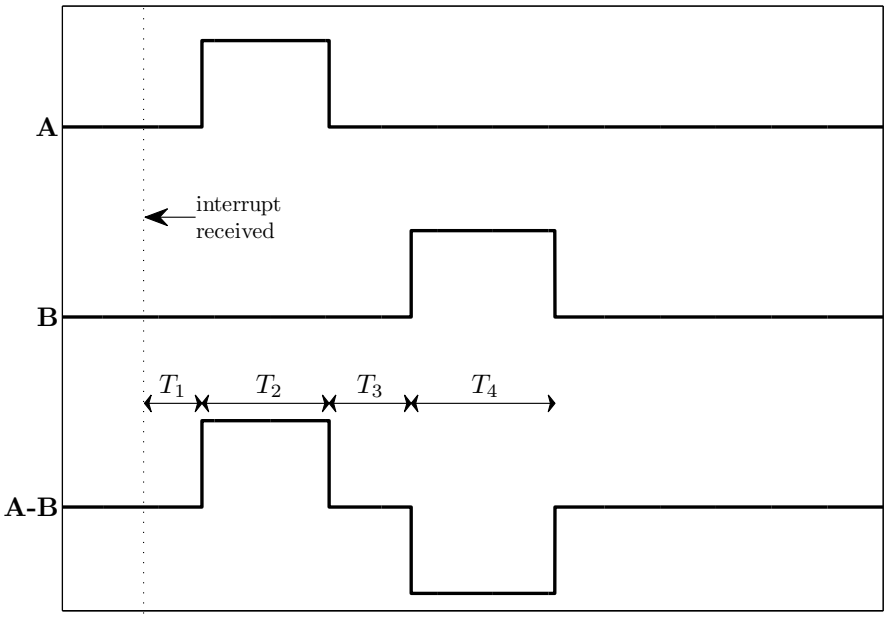

Figure 2.4: A and B signals

input of the opamp. The voltage-to-current converter part operates at ±12 V obtained from the lead-acid batteries. The voltage-to-current converter part is the only part of the current source system which is placed inside the scanner room in the experiments (Figure 2.2). Therefore the circuit and the batteries are placed in an aluminum case. For the output cables which transfer current from voltage-to-current converter part to the phantom (the imaging object), feed-through filters are used. Furthermore, fiber-optic links are used between microcontroller part and the voltage-to-current converter part in order to preclude any possible noise from microcontroller box inside the scanner room.

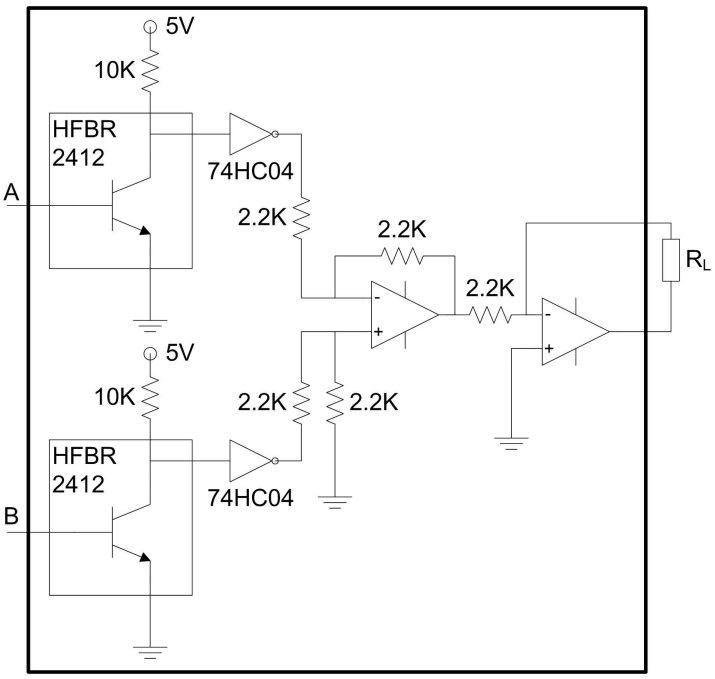

Figure 2.5: Circuit diagram for voltage-to-current converter part. R_L denotes the load resistor which is the experimental phantom in our case. HFBR2412 is a optical receiver which converts optical signals to electrical signals

Chapter 3

MREIT BASED ON THE SOLUTION OF THE CONVECTION EQUATION

3.1 Methods

3.1.1 The Algorithm

The relation between electrical conductivity (σ), current density ($\mathbf{J}$), and Laplacian of the B_z ($\nabla^2 B_z$) was derived in Section 1.2.2 as

$$\frac{1}{\sigma}(J_x \frac{\partial \sigma}{\partial y} - J_y \frac{\partial \sigma}{\partial x}) = \frac{\nabla^2 B_z}{\mu_0}. \tag{3.1}$$

Defining $R = \ln \sigma$, Equation 3.1 can be expressed as [36]

$$\nabla^2 B_z = \mu_0 (J_x \frac{\partial R}{\partial y} - J_y \frac{\partial R}{\partial x}). \tag{3.2}$$

Furthermore defining $\widetilde{\mathbf{J}} = (-J_y, J_x)$, and $\nabla R = (\frac{\partial R}{\partial x}, \frac{\partial R}{\partial y})$, Equation 3.2 can be put into the form of the scalar pure convection equation, which is introduced and

discussed in the Appendix A, as

$$\widetilde{\mathbf{J}} \cdot \nabla R = \frac{\nabla^2 B_z}{\mu_0}. \tag{3.3}$$

In this equation, $\widetilde{\mathbf{J}}$ may be recognized as the convective field defined in Equation A.1, R is the scalar field to be solved and $\frac{\nabla^2 B_z}{\mu_0}$ is the source term.

Apart from R, the $\widetilde{\mathbf{J}}$ vector is also unknown in Equation (3.3) since the current density is not known. The actual current density consists of two components, namely $\mathbf{J}^0$ and $\mathbf{J}^d$, where $\mathbf{J}^0$ is the current density distribution obtained by solving the forward problem for the homogenous conductivity distribution and $\mathbf{J}^d$ is defined as the difference current density such that $\mathbf{J}^d = \mathbf{J} - \mathbf{J}^0$. Since only B_z is utilized, only an estimate for the actual difference current density, namely $\mathbf{J}^*$, can be calculated [19]. $\mathbf{J}^*$ is calculated from the relation $\mathbf{J}^* = (\frac{\partial \beta}{\partial y}, -\frac{\partial \beta}{\partial x})$ where β is the solution of the two-dimensional (2-D) Laplace equation given as

$$\nabla^2 \beta = \frac{\nabla^2 B_z}{\mu_0} \text{ in } \Omega' \text{ and } \beta = 0 \text{ on } \partial\Omega' \tag{3.4}$$

where Ω' is the intersection of Ω with a $z = constant$ plane (the slice of interest) and $\partial\Omega'$ is the boundary of the intersection. Once $\mathbf{J}^*$ is obtained, the projected current density which is defined as $\mathbf{J}^P = \mathbf{J}^* + \mathbf{J}^0$ is calculated. $\widetilde{\mathbf{J}} = (-J_y^P, J_x^P)$ is then substituted into Equation (3.3) so that it can be solved for R.

For the numerical solution of Equation (3.3) on the slice of interest, finite element method (FEM) is used. In the FEM formulation, either standard Galerkin weighted residual method [45], or Galerkin weighted residual method with streamline upwind Petrov-Galerkin (SUPG) stabilization [46], which is discussed in detail in Appendix A, is used.

In general more than one current injections may be used for MREIT. If two orthogonal current injections are used, the final matrix system for Equation (3.3) is written as

$$\left[\begin{array}{c} \mathbf{K}_1 \\ \mathbf{K}_2 \end{array} \right]_{2\mathrm{N}\times\mathrm{N}} \mathbf{R}_{\mathrm{N}\times 1} = \left[\begin{array}{c} \mathbf{b}_1 \\ \mathbf{b}_2 \end{array} \right]_{2\mathrm{N}\times 1} \tag{3.5}$$

where N is the number of nodes in the triangular mesh at the slice of interest, and $\mathbf{K}_1$, $\mathbf{K}_2$ and $\mathbf{b}_1$, $\mathbf{b}_2$ are obtained for two orthogonal current injections by using Galerkin weighted residual FEM with or without SUPG stabilization. In solving Equation (3.3) boundary conditions must also be considered. When Dirichlet boundary conditions are used, some nodes on the boundary are assigned conductivity values and the matrix system given in (3.5) is reduced. The reduced system is solved using singular value decomposition (SVD) without truncation. If only one current injection is used, the matrix system involving only $\mathbf{K}_1$ and $\mathbf{b}_1$ is solved.

3.1.2 Simulation methods

For simulations, a cylindrical phantom of height 20 cm and diameter 9.4 cm is modeled (Figure 3.1(a)) using Comsol Multiphysics software package in order to solve for electric potential in the three-dimensional forward problem explained in Section 1.2.1. The regions that the current is injected and sunk are 3 cm recessed from the body of the phantom to model the phantom used in experiments. Current is injected through circular electrodes of diameter 1 cm located at the ends of recessed parts. Cross-section of the recessed parts is square with edges of 2.5 cm long. Current is applied between opposite electrodes and two orthogonal current injection directions are possible as shown in Figure 3.1(c). The amount of injected current is 10 mA and total current injection time is 50 ms.

Background conductivity of the simulation phantom is taken to be 1 S/m and two cylindrical regions of conductivity anomaly are modeled inside the phantom. Figure 3.2(b) shows the conductivity distribution of the simulation phantom for the $z = 0$ slice. The conductivities of the low and high conductivity anomalies are 0.2 S/m and 5 S/m respectively. However the change of conductivity from the background value to the low and high values in the anomalous regions is not sharp but it is tapered as shown Figure 3.3(b), (d) and (f). Tetrahedral

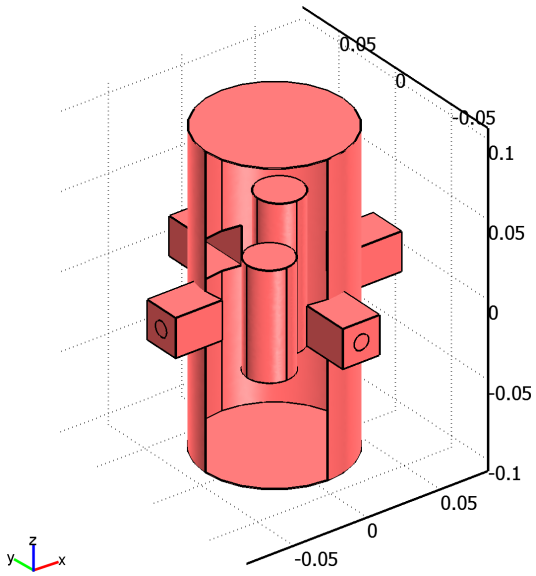

(a)

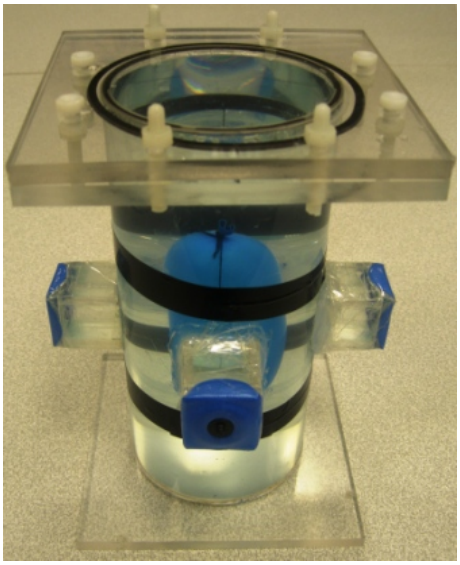

(b)

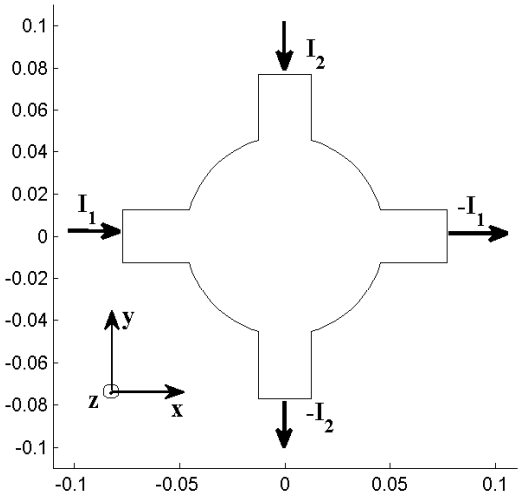

(c)

Figure 3.1: (a) Phantom model drawn using Comsol Multiphysics. Two cylindrical regions which have different conductivity than the background are also seen. The height of the first cylindrical region is 10 cm while the height of the other cylindrical region is 8 cm. z-direction is the direction of the main magnetic field of the MRI system. (b) Picture of the experiment phantom for the first experimental setup explained in section 3.1.3. The balloon inside the phantom acts as an insulator and it isolates its inside solution from the background solution. (c) Illustration of the center transverse slice of the phantom where $z = 0$. The directions of two orthogonal current injection profiles are also shown.

elements with quadratic shape functions are used for the FEM formulation of the three-dimensional problem. There are 1,159,225 tetrahedral elements and 212,007 nodes (1,608,578 degrees of freedom since quadratic shape functions are used) in total. Once the forward problem is solved, the current density distribution is obtained on the nodes of a 2-D triangular mesh representing the plane at $z = 0$. The relation given in (1.4) is then used to calculate the simulated $\nabla^2 B_z$. There are 5088 triangles and 2657 nodes in the 2-D triangular mesh.

The simulated $\nabla^2 B_z$ at the slice of interest is the input data for reconstructing the projected transverse current density on that slice. Conductivity distribution is then reconstructed by solving Equation (3.3) using the proposed method. Errors made in the reconstructed projected current density and the reconstructed conductivity in the slice of interest are calculated using the relative L^2-error formula:

$$\mathrm{E}_{L^2}(\mathbf{J}^P) = 100\left[\frac{\sum_{i=1}^{M}((J_{x_i}^a - J_{x_i}^P)^2 + (J_{y_i}^a - J_{y_i}^P)^2)}{\sum_{i=1}^{M}({J_{x_i}^a}^2 + {J_{y_i}^a}^2)}\right]^{1/2}$$
$$\mathrm{E}_{L^2}(\sigma) = 100\left[\frac{\sum_{j=1}^{N}(\sigma_j^a - \sigma_j)^2}{\sum_{j=1}^{N}{\sigma_j^a}^2}\right]^{1/2} \tag{3.6}$$

where $J_{x_i}^a$ and $J_{y_i}^a$ are the x- and y- components of the actual current density at the center of the i'th triangle, $J_{x_i}^P$ and $J_{y_i}^P$ are the x- and y- components of the reconstructed projected current density, σ_j^a and σ_j are the actual and reconstructed conductivity distributions at the j'th node respectively, N is the number of nodes in the 2-D mesh and M is the number of the triangles in the 2-D mesh.

3.1.3 Experimental methods

Two different experimental setups are prepared for the experiments. For the first experimental setup, an experimental phantom, dimensions of which are the same as the simulation phantom explained in section 3.1.2, is manufactured. The

phantom is first filled with the background solution (12 gr/l NaCl and 1.5 gr/l $CuSO_4.5H_2O$). An insulator object is then obtained by filling a cylindrically shaped balloon with the background solution so that the solutions inside and outside the balloon have no contact (Figure 3.1(b)). Current is injected through electrodes facing each other and data is obtained for two orthogonal current injection profiles. B_z is measured at three consecutive (no gap) transverse slices of thickness 5 mm. $\nabla^2 B_z$ is calculated at the middle slice which is centered to $z = 0$ plane of the phantom. For the Laplacian operator the finite difference approximation is utilized:

$$\nabla^2 B_{zc}(m,n) = \frac{B_{zc}(m+1,n)-2B_{zc}(m,n)+B_{zc}(m-1,n)}{(\Delta x)^2} + \frac{B_{zc}(m,n+1)-2B_{zc}(m,n)+B_{zc}(m,n-1)}{(\Delta y)^2} + \frac{B_{zu}(m,n+1)-2B_{zc}(m,n)+B_{zl}(m,n-1)}{(\Delta z)^2} \tag{3.7}$$

where $m = 1, ..., N$, $n = 1, ..., N$, B_{zu}, B_{zc}, B_{zl} are B_z matrices obtained at the upper, center and lower slices respectively, Δx and Δy are the sizes of an MR image pixel in x- and y-directions respectively, Δz is the slice thickness and N is the size of the MR image matrix in both directions. The standard spin-echo MREIT pulse sequence, which is discussed in Section 2.1, is used. The magnitude of the applied current is 10 mA and total duration of current injection is 42 ms. The number of averages is 5, echo time (T_E) is 60 ms, repetition time (T_R) is 900 ms, image matrix is 128×128 and the field of view is 180×180 mm. The experiments are conducted using a 3T MRI scanner (Siemens Magnetom Trio).

For the second experimental setup, the same experimental phantom is used. The phantom is filled with background solution (3 gr/l NaCl, 1 gr/l $CuSO_4.5H_2O$) and two conductive cylindrical agar (15 gr/l agar) objects of height 7 cm and diameter 3.4 cm is placed inside the phantom. While the first object has lower conductivity (0.8 gr/l NaCl 1 gr/l $CuSO_4.5H_2O$) than the background solution the other object has higher conductivity (12 gr/l NaCl, 1 gr/l $CuSO_4.5H_2O$).

All other experiment parameters including MR imaging parameters and current injection time is the same with the first experimental setup.

3.2 Results

3.2.1 Simulation Results

Simulated $\nabla^2 B_z$ data, actual conductivity distribution, actual difference current density distribution ($x-$ and $y-$ components), and $\mathbf{J}^*$ reconstructed using the method explained in Section 3.1.1 are shown in Figure 3.2 for the simulation phantom. All images are drawn for the central transverse slice of the simulation phantom where $z = 0$ (named as imaging slice hereafter) and when current is injected in $\mathbf{I}_1$ direction shown in Figure 3.1(c). The relative L^2-error made in the reconstructed $\mathbf{J}^*$ is 23.59%.

Figure 3.3(a) shows the reconstructed conductivity distribution at the imaging slice for the case of single current injection ($\mathbf{I}_1$ direction in Figure 3.1(c)) when no stabilization is used in the FEM with Galerkin weighted residual method. Conductivity values on the boundary are assumed to be 1 S/m ($R = 0$ since $R = \ln \sigma$). Reconstructed conductivity of the upper and lower recessed regions is not shown in the figure because in these regions excessively noisy distributions of conductivity with very large variance are obtained. This is most likely due to the fact that in the upper and lower recessed regions current density is very low and therefore the convection equation is ill-defined in these regions. Next, SUPG stabilization is utilized in the numerical solution of equation (3.3) for the case of single current injection and the reconstructed conductivity distribution at the imaging slice is given in Figure 3.3(c). A more stable solution is obtained and the relative L^2-error made in the reconstructed conductivity is 6.26% (L^2-error in the previous case without using stabilization was 56% even excluding upper

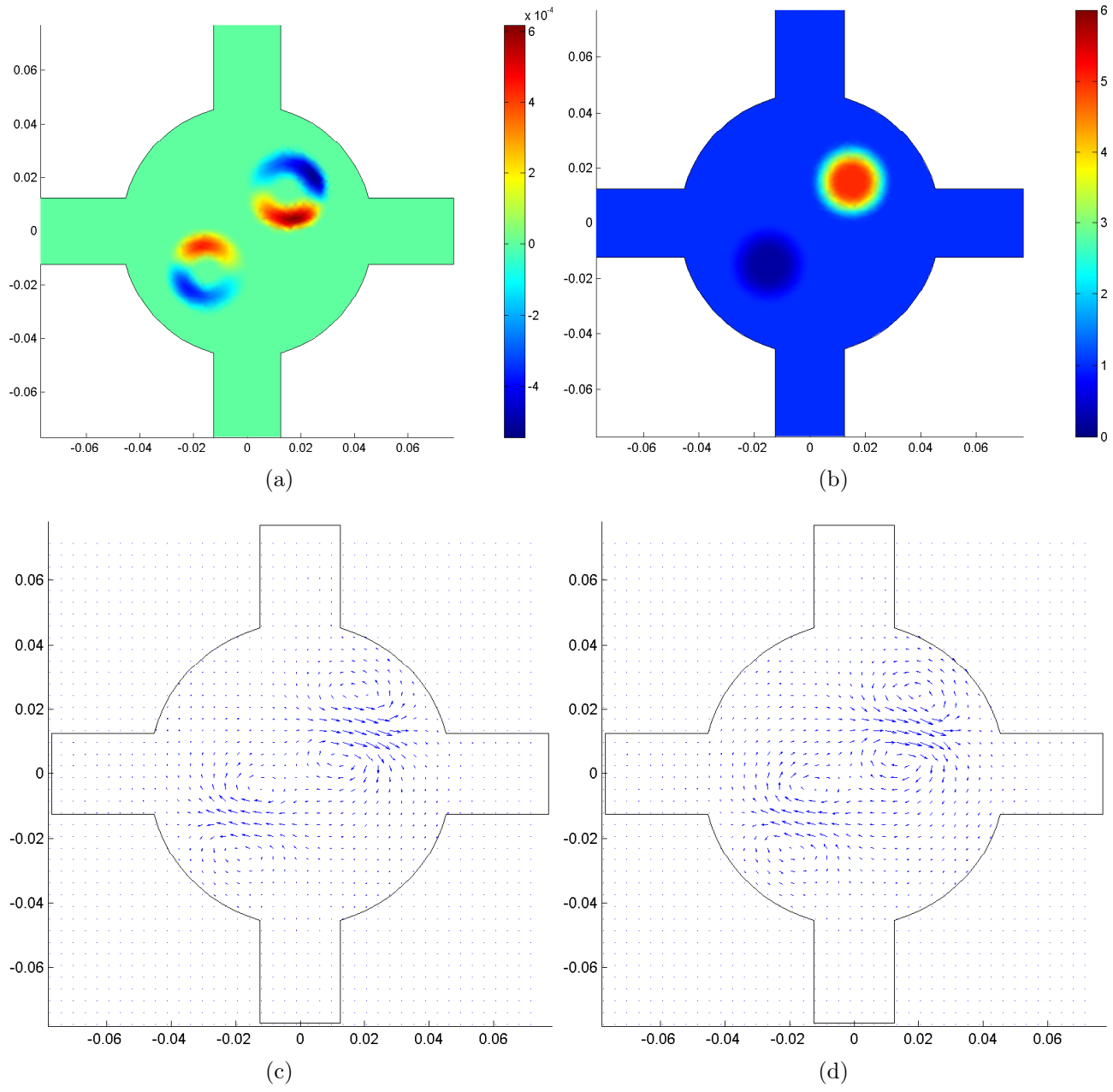

Figure 3.2: Figures at the central slice of the simulation phantom: (a) simulated $\nabla^2 B_z$, (b) actual conductivity distribution, (c) quiver plot of the actual difference current density distribution ($x-$ and $y-$ components), (d) quiver plot of the reconstructed $\mathbf{J}^*$

and lower recessed regions). Figure 3.3(b) and (d) show the reconstructed conductivity profiles on the $x = y$ line of the imaging slice for the cases of without and with stabilization respectively. It is observed that oscillations seen in the profile when no stabilization is used disappear with the use of stabilization and yet transition regions of conductivity change are still well represented.

Figure 3.3(e) and (f) show the reconstructed conductivity at the imaging slice for the case of two current injections when no stabilization is used. The solution is stable even though no stabilization is utilized and the L^2-error made in the reconstructed conductivity is 3.68%. With two current injections, we know that the current distribution in the recessed regions has large values at least for one of the current injection cases. Therefore, when two current injections are used, the ill-defined convection equation situation is not observed. Furthermore, when SUPG stabilization is used, no significant improvement is obtained in the reconstructed conductivity distribution. It is also important to note that, in the example investigated, the conductivity distribution does not have sharp variations nor the given boundary conditions are inconsistent, and therefore stabilization is not necessary.

The algorithm is also tested when the conductivity distribution at the imaging slice has sharp variations. For this purpose, the phantom geometry same with the previous case is used with a narrower conductivity transition region. The actual conductivity profile on the $x = y$ line at the imaging slice is given in Figure 3.4(b) and (d). Reconstruction results for the case of two current injections are also shown in Figure 3.4. Figure 3.4(a) and (b) show the conductivity reconstructions when no stabilization is utilized. L^2-error made in the reconstructed conductivity is 15.88% and considerable oscillations are observed. However, when SUPG stabilization is used L^2-error decrease to 7.11% and oscillations disappear as shown in Figure 3.4(c) and (d). Therefore, although stabilization is not found to be necessary when conductivity variations are not sharp, it is found that

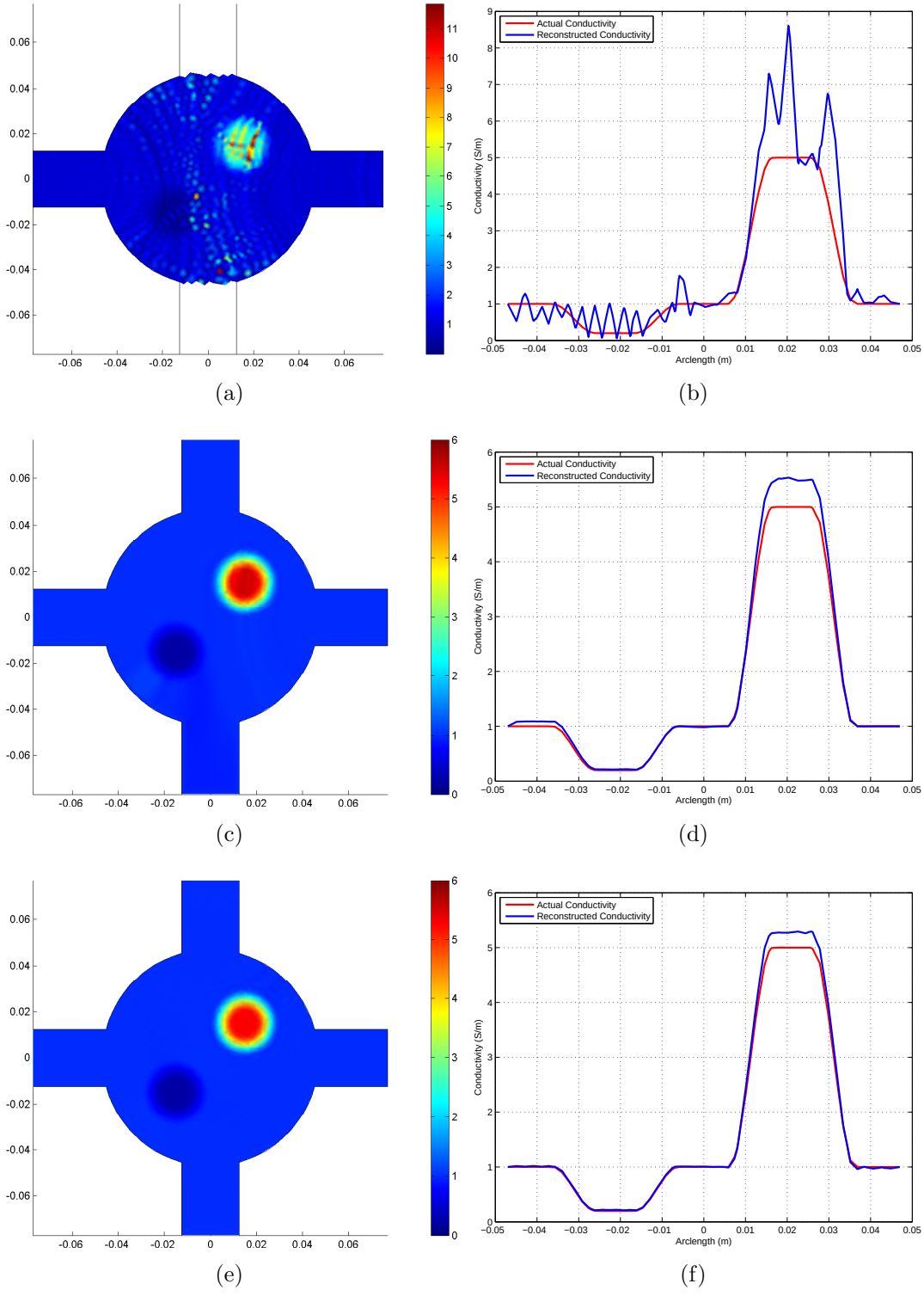

Figure 3.3: Reconstructed conductivity in the simulations: (a) the reconstructed conductivity distribution at the center slice, (b) the reconstructed conductivity profile on the $x = y$ line at the center slice. (a) and (b) are obtained when a single current injection is used without stabilization. (c) and (d) are same as (a) and (b) but with the SUPG stabilization applied in the solution. (e) and (f) are same as (a) and (b) but when two current injections are utilized without stabilization.

for subjects in which conductivity variations are sharp and abrupt, stabilization becomes necessary.

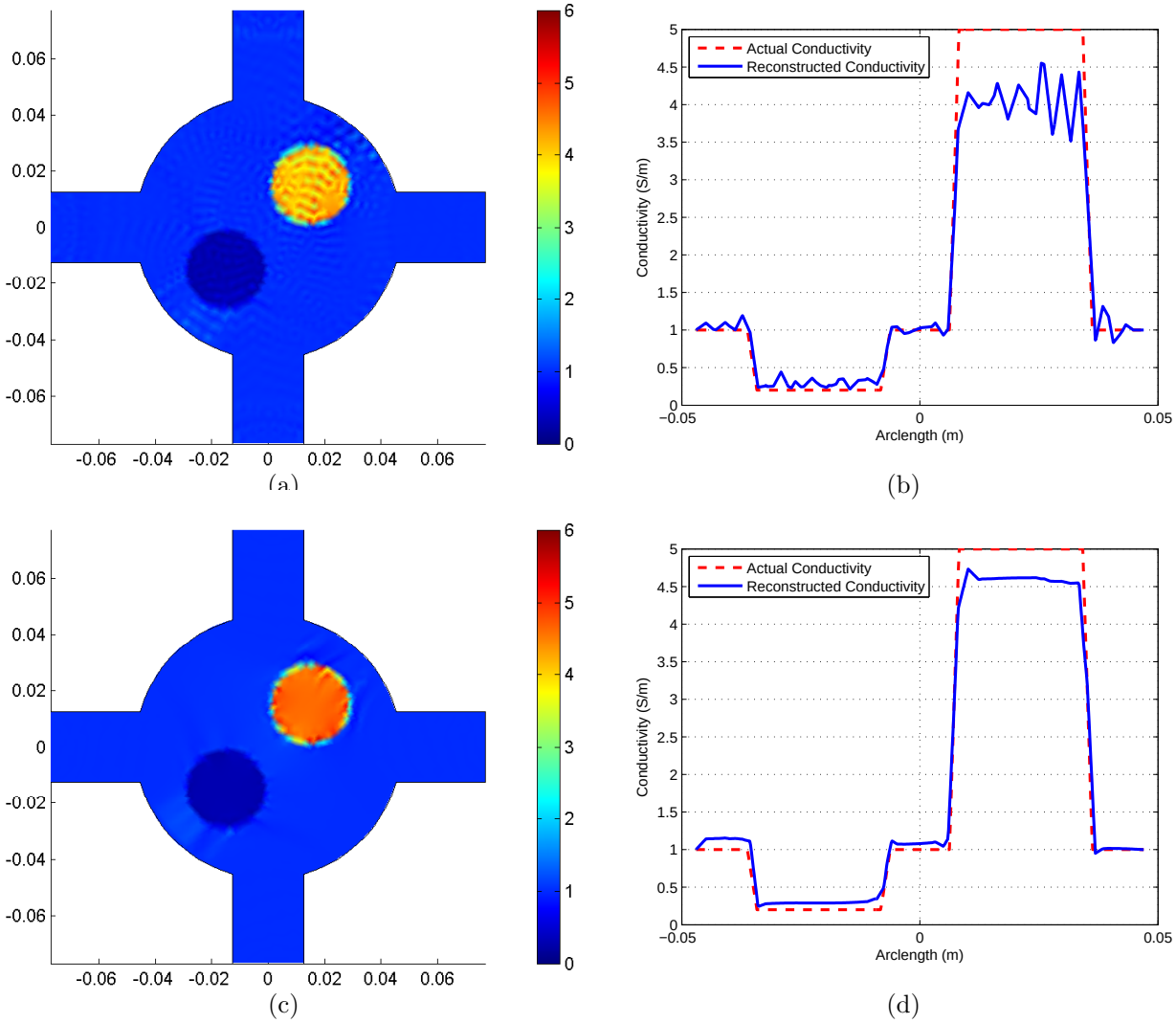

Figure 3.4: Reconstructed conductivity in the simulations when conductivity change is sharp: (a) reconstructed conductivity distribution at the center slice, (b) the reconstructed (solid line) and actual (broken line) conductivity profiles on the $x = y$ line at the center slice.

Performance of the algorithm against noise in measurement data is also investigated. The noise in B_z is assumed to have Gaussian distribution with the standard deviation $\sigma_{B_z} = 1/(2\gamma T_C SNR)$ where γ is the gyromagnetic ratio ($26.7519 \times 10^7 rad/Ts$), T_C is the duration of current injection in seconds and SNR is the signal-to-noise ratio of the MR system [17]. Although in practice one needs to know B_z in three consecutive slices in z direction in order to calculate

$\nabla^2 B_z$ using finite difference approximation as given in Equation (3.7), we use the relation given in (1.4) to calculate $\nabla^2 B_z$. Therefore in order to calculate the noise image which will be added to $\nabla^2 B_z$, the following steps are followed: Let G_u, G_c, and G_l be the noise images representing the noise in B_z at upper, center and lower slices respectively each of which calculated independently for specific SNR and T_C. $\nabla^2 G$ is then calculated using Equation (3.7) when B_z is replaced with G and it is added to $\nabla^2 B_z$ which is calculated using (1.4). Noisy $\nabla^2 B_z$ and $\mathbf{J}^*$ obtained using the noisy $\nabla^2 B_z$ are given in Figure 3.5(a) and (b) when $SNR = 180$ and $T_C = 50ms$. The reconstructed conductivity distribution and conductivity profile on the $x = y$ line are given at the imaging slice in Figure 3.5(c) and (d) when no stabilization is applied and in Figure 3.5(e) and (f) when SUPG stabilization is applied. Two current injection profiles are utilized in all reconstructions. The relative L^2-error made in the reconstruction of the conductivity is 17.33% when no stabilization is utilized and 13.41% when SUPG stabilization is utilized. The last two given relative L^2-errors are 29.94% and 20.71% when SNR is 120 (T_C is the same), 54.76% and 31.65% when SNR is 90. The benefit of using SUPG stabilization technique in decreasing the oscillations and the L^2-errors is clearly seen and is more pronounced for low SNR values.

3.2.2 Experimental Results

Experimental results for the first experimental setup explained in Section 3.1.3 are given in Figure 3.6. Figure 3.6(a) and (b) show the "masked" $\nabla^2 B_z$ which are calculated from the data obtained from the experimental phantom for two current injections respectively at the center slice of the phantom (called as imaging slice hereafter). All conductivity reconstructions for experiments is made using two current injections. It is observed that the numerical error in the calculated $\nabla^2 B_z$ is most pronounced in recessed parts of the phantom since B_z changes rapidly

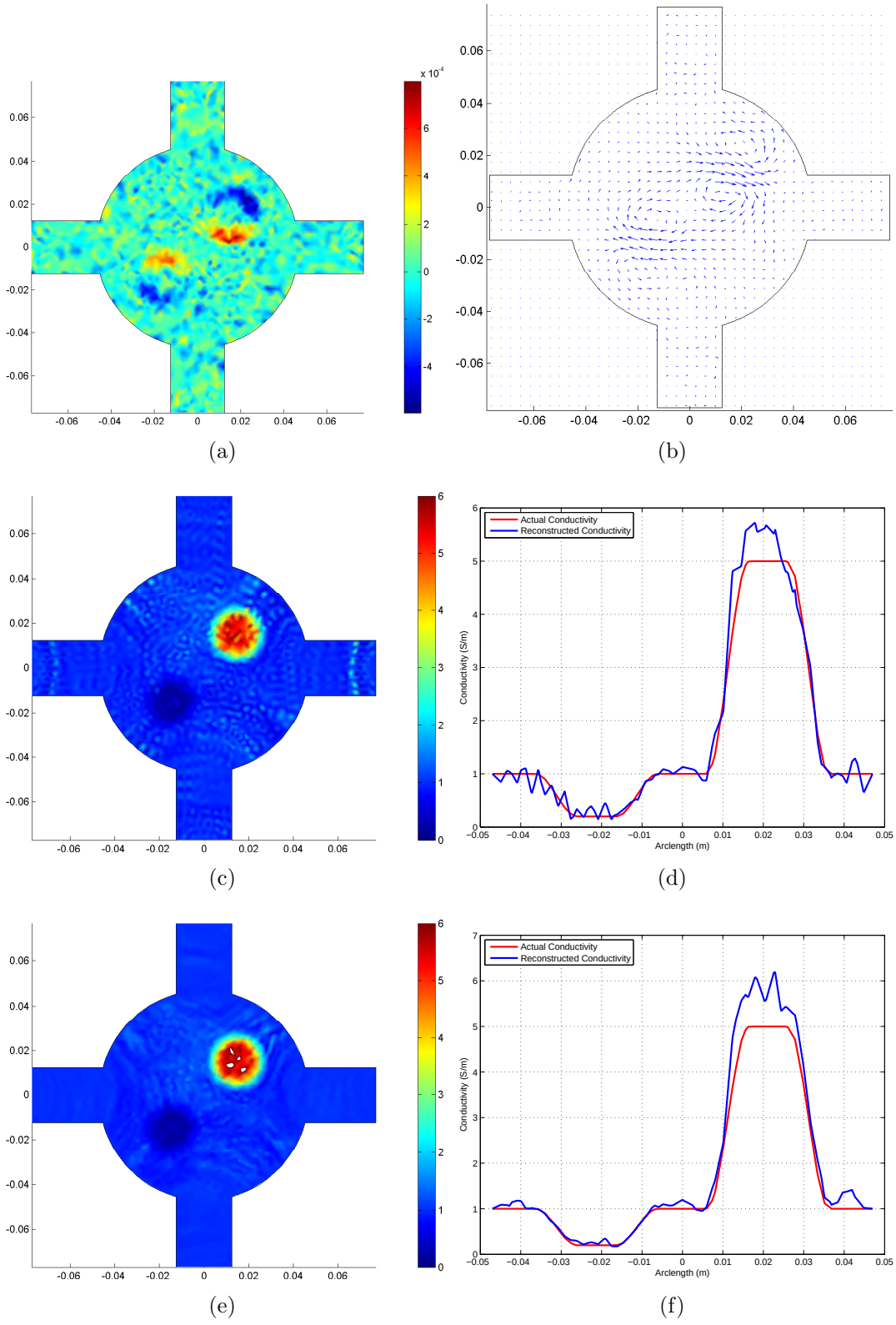

Figure 3.5: Simulation results for the evaluation of the performance of the algorithm against noise: (a) Noisy $\nabla^2 B_z$ for $SNR = 180$ and $T_C = 50ms$, (b) Quiver plot of calculated $\mathbf{J}^*$ using noisy $\nabla^2 B_z$, (c) reconstructed conductivity distribution at the center slice, (d) reconstructed conductivity profile on the $x = y$ line at the center slice. (c) and (d) are obtained when no stabilization is applied. (e) and (f) are same with (c) and (d) but with SUPG stabilization applied.

and also has high magnitude in these regions. Also B_z measurements near the boundary of the phantom have relatively high noise probably due to the partial volume effect in MR voxels here. Therefore $\nabla^2 B_z$ data is masked such that only $\nabla^2 B_z$ calculated on the circular region of radius 0.045 m is used and outside of this region, including recessed parts, $\nabla^2 B_z$ is taken as zero in the calculations (it is known that $\nabla^2 B_z = 0$ in these regions since the conductivity is constant).

The differentiation process during the calculation of $\nabla^2 B_z$ amplifies high spatial frequency components of B_z which leads to the amplification of the noise inherent in B_z measurements. Therefore, a Hanning window low pass filter is applied to the $\nabla^2 B_z$ data in the frequency domain. Figure 3.6(c) and (d) show the low pass filtered versions of the $\nabla^2 B_z$ data for two current injection profiles. The Hanning window is $w(k_x, k_y) = 0.5(1 - \cos \frac{\pi k}{k_{max}})$ where k_x and k_y are spatial frequencies in x and y directions respectively [47]. k_{max} should be chosen separately for each experimental setup depending on the SNR of the MR system and to the magnitude of the $\nabla^2 B_z$ data which depends on the spatial contrast of the conductivity. For the experimental data given in Figure 3.6, k_{max} is chosen as $400m^{-1}$. It should be noted that the choice of k_{max} sets a lower bound for the spatial resolution of the reconstructed conductivity [22]. Figure 3.6(e) and (f) show the calculated $\mathbf{J}^*$ for two current injections using filtered $\nabla^2 B_z$ data.

In Figure 3.7(a) and (b) the reconstructed conductivity distribution and conductivity profile on the $x = y$ line are given at the imaging slice when the $\nabla^2 B_z$ data shown in Figure 3.6(a) and (b) is used without any stabilization. The reconstructed conductivity suffered from spurious oscillations. Since the differentiation process amplifies the noise, $\nabla^2 B_z$ data contain sharp variations due to the noise and the conductivity reconstructed from such an input would have sharp variations too. However, as indicated in Section 3.2.1, when no stabilization is used in the FEM formulation, sharp variations in the solution cause oscillations as seen in Figure 3.7(a) and (b). When the low-pass filtered versions of $\nabla^2 B_z$ data

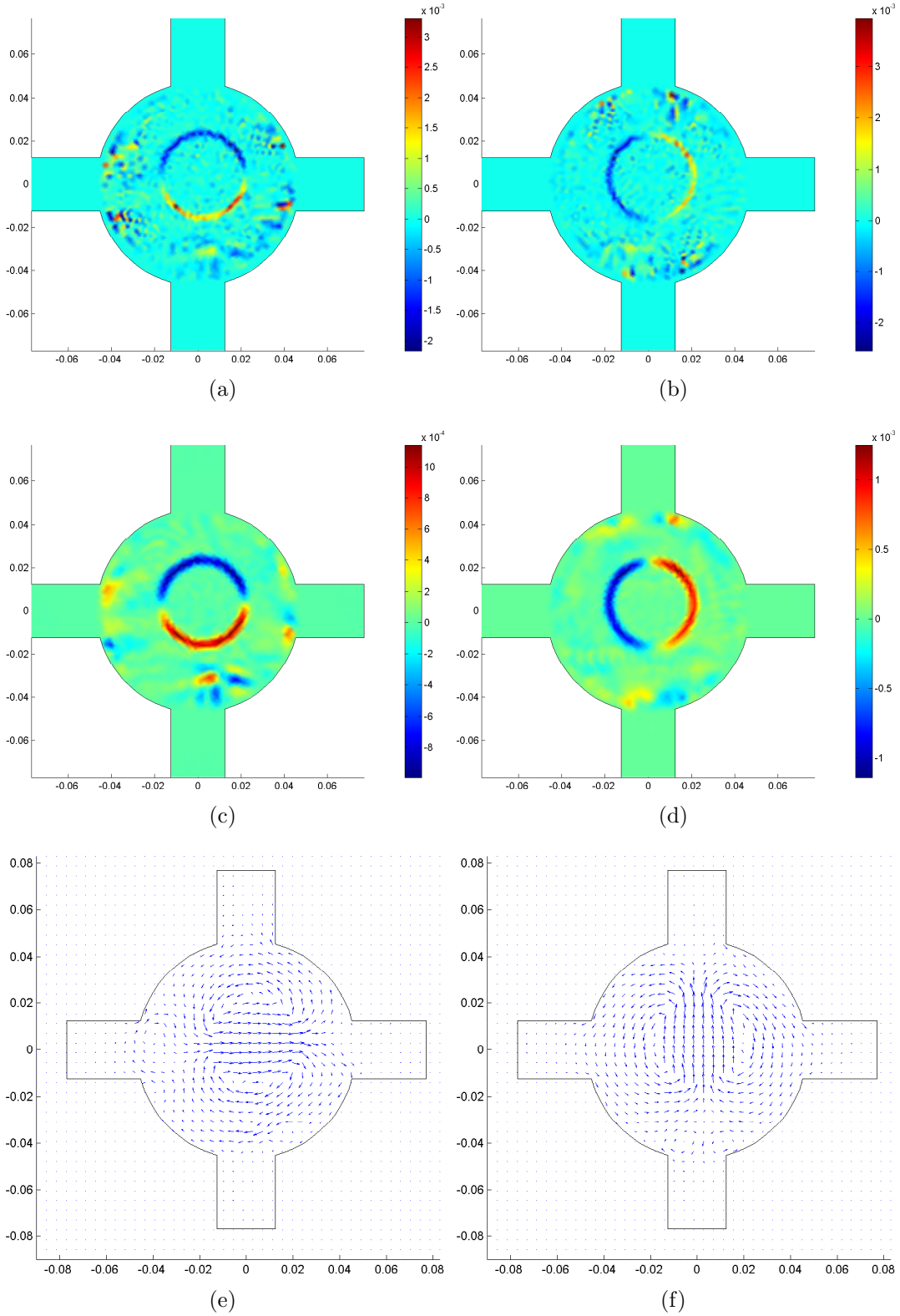

Figure 3.6: Input data and the reconstructed current densities for the first experimental setup explained in Section 3.1.3. (a) and (b) are $\nabla^2 B_z$ calculated from the measured B_z for two current injections respectively, (c) and (d) are filtered versions of $\nabla^2 B_z$ given in (a) and (b), (e) and (f) are the quiver plots of calculated $\mathbf{J}^*$ for the two current injections respectively

(Figure 3.6(c) and (d)) are used, since the sharp variations in $\nabla^2 B_z$ due to the amplified noise are smoothed by the filter, the oscillations in the reconstructed conductivity decrease as shown in Figure 3.7(c) and (d). Figure 3.7(e) and (f) show the reconstructed conductivity when the original $\nabla^2 B_z$ data (no filter) is used with SUPG stabilization. This time, the artificial diffusion term which is introduced to the convection equation by SUPG stabilization smears out the sharp variations in the solution so that the oscillations decrease. Figure 3.7(g) and (h) show the reconstructed conductivity when both the filtered versions of $\nabla^2 B_z$ (Figure 3.6(c) and (d)) and also SUPG stabilization are used.

Experimental results for the second experimental setup explained in Section 3.1.3 are given in Figure 3.8. Since MR signals coming from the agar objects are relatively low, the measured B_z data in these regions is greatly corrupted with noise. Therefore all reconstructions are done with low-pass filtered versions of $\nabla^2 B_z$ data. The cosine window explained above is used with $k_{max} = 300m^{-1}$. Figure 3.8(a) and (b) show the low-pass filtered $\nabla^2 B_z$ data for two current injections respectively. Figure 3.8(c) shows the reconstructed conductivity distribution at the center slice of the phantom when no stabilization is used. The reconstructed conductivity distribution suffers from oscillations when no stabilization is used. Figure 3.8(d) shows the reconstructed conductivity distribution when SUPG stabilization is used. The oscillations in the solution decreases and the conductivity is well reconstructed.

3.3 Discussion

In this chapter, a new MREIT algorithm is proposed to reconstruct conductivity distribution on a slice of interest given the $\nabla^2 B_z$ data for that slice. The relation between conductivity and $\nabla^2 B_z$ data is formulated as a steady-state scalar convection equation (Equation 3.3) and reconstruction of conductivity is achieved by

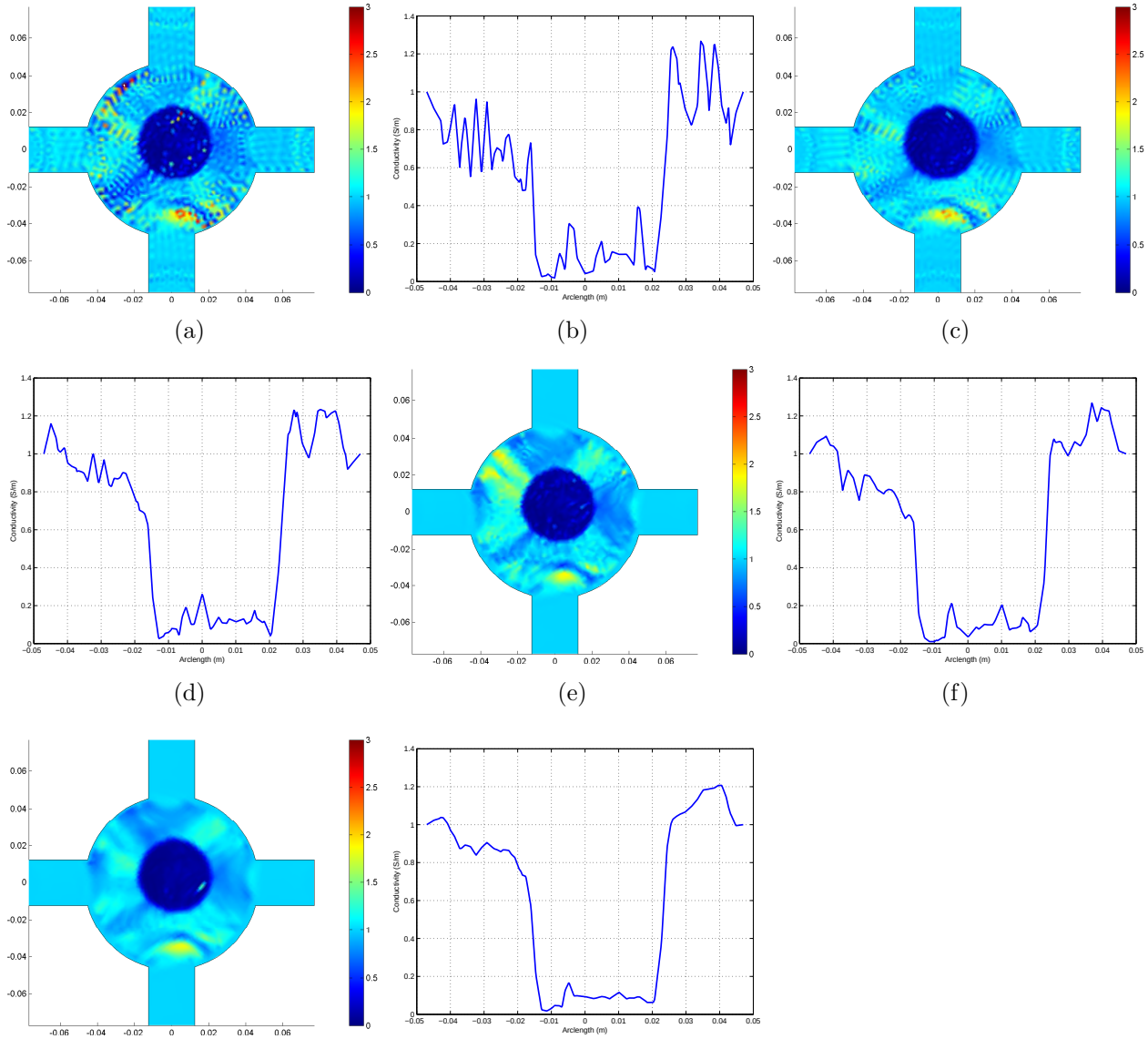

Figure 3.7: Reconstructed conductivity distributions for the first experimental setup explained in Section 3.1.3. (a) reconstructed conductivity distribution at the center slice of the phantom, (b) reconstructed conductivity profile on the $x = y$ line at the center slice. (a) and (b) is obtained when the original $\nabla^2 B_z$ (no filter) is used without stabilization. (c) and (d) are same with (a) and (b) but the filtered $\nabla^2 B_z$ is used without stabilization. (e) and (f) are same with (a) and (b) but the original $\nabla^2 B_z$ (no filter) is used with the SUPG stabilization. (g) and (h) are same with (a) and (b) but the filtered $\nabla^2 B_z$ is used with the SUPG stabilization

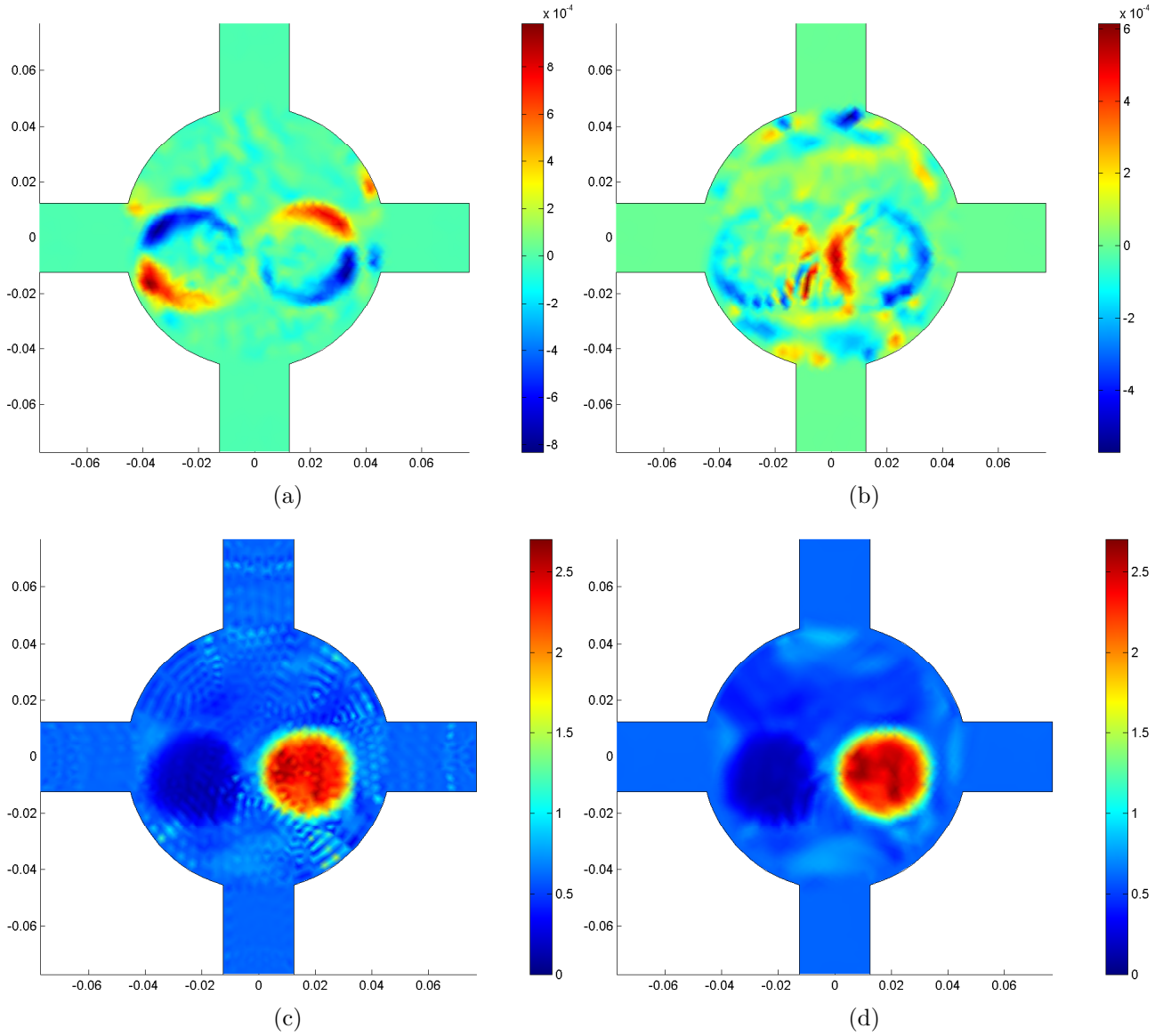

Figure 3.8: Results for the second experimental setup explained in Section 3.1.3). (a) and (b) are $\nabla^2 B_z$ calculated from the measured B_z for two current injections respectively. $\nabla^2 B_z$ is multiplied with a cosine window in the frequency domain ($k_{max} = 300m^{-1}$). (c) the reconstructed conductivity distribution at the center slice when no stabilization is used (d) the reconstructed conductivity distribution at the center slice when SUPG stabilization is used

the numerical solution of the convection equation using FEM. Effects of including stabilization in the FEM formulation are also investigated. Reconstructed conductivity distributions using both simulated and experimental data show that the proposed algorithm is successful. To our knowledge, it is the first time that the MREIT problem is handled as the solution of a scalar convection equation.

It is well known that the numerical solution of the pure convection equation with Galerkin weighted residual FEM is unstable and gives inaccurate results if the actual solution includes sharp variations [48, 49]. Sharp variations in the solution may be due to internal regions where the solution has steep gradient or due to inconsistent Dirichlet boundary conditions. In a general sense, the solution of Equation 3.3 may be thought of as taking the line integral of ∇R along the direction of the convective field $\widetilde{\mathbf{J}}$. If the given R on the inlet boundary on which $\widetilde{\mathbf{J}}.\mathbf{n} < 0$ ($\mathbf{n}$ being the outward normal to the boundary) and the outlet boundary on which $\widetilde{\mathbf{J}}.\mathbf{n} > 0$ are inconsistent, the solution will have a sharp variation near the outlet boundary (Please see Appendix A for a one-dimensional example). The instability of the numerical solution, which is caused by any sharp variation in the solution, may be overcome by choosing a stabilization technique which in effect adds a diffusion term to the partial differential equation. In this study the streamline-upwind Petrov Galerkin (SUPG) stabilization technique is used.

It is found that when two current injections are used the Galerkin weighted residual FEM formulation without stabilization gives accurate results as shown in Figure 3.3(e) and (f) if the actual conductivity distribution does not have sharp variations and the given Dirichlet boundary conditions are consistent. However, for the case when the conductivity distribution has sharp variations, spurious oscillations occur in the solution and an accurate solution is not obtained as shown in Figure 3.4(a) and (b). The oscillations disappear with the use of SUPG stabilization as shown in Figure 3.4(c) and (d). L^2-errors in the reconstructed conductivities with and without stabilization also support that the stabilization

improves the accuracy of the solution. The case for which the conductivity variations are not sharp but the given Dirichlet boundary conditions are inconsistent is also investigated. Although the reconstructed conductivity suffered from spurious oscillations when FEM without stabilization is used, the solution is stable when SUPG stabilization is used.

In general for MREIT at least two orthogonal current injection profiles are used in order to guarantee unique conductivity reconstruction apart from a constant factor [29]. However it is also of interest to investigate what can be done for the case of a single current injection [50]. As evident from Equation (1.5), the conductivity reconstruction problem is ill-defined in the regions where the current density is low. This problem can be overcome by using more than one current injection profiles such that the current density is high enough in the problematic regions for at least one current injection. However if one current injection is used this is not possible and the inaccurate solution in the problematic regions may harm the accuracy of the solution in the whole domain. For the simulation phantom considered in this study, if the current is injected in $\mathbf{I}_1$ direction, the current density in upper and lower recessed regions is very low which makes the convection equation ill-defined here. When the FEM without stabilization is used, the reconstructed unstable conductivity is shown in Figure 3.3(a) and (b). On the other hand, SUPG stabilization introduces an artificial diffusion term to the convection equation such that the amount of diffusion is higher in the regions where the magnitude of the convective field $\widetilde{\mathbf{J}}$ is low. Although we may not guarantee the accuracy of the solution in the problematic regions, the accuracy of the solution in other regions is higher (L^2-error is decreased) and the solution is stabilized as shown in Figure 3.3(c) and (d). Therefore, if there are regions in the solution domain where the convection equation is ill-defined, which especially occur when single current injection is used, the SUPG stabilization is beneficial. Note that we may use more than one current injection and still have problematic

regions where the current density is low for all of the current injection profiles. Therefore SUPG stabilization is also beneficial for such cases.

In practice, noise is inherent in the measurement of B_z and robustness of the proposed algorithm against noise must also be investigated. Noise in B_z simulations is modeled by using the noise model given by Scott *et al.* (1992). Two current injection profiles are used for all reconstructions using noisy data. It is observed that when no stabilization technique is utilized in the solution using noisy data, the reconstructed conductivity contained unacceptable oscillations (Figure 3.5(c) and (d)). On the contrary, when SUPG stabilization technique is utilized, the oscillations in the solution are diminished and L^2-error made in the reconstructions of the conductivity is lower. The reconstructed conductivity for this case is given in Figure 3.5(e) and (f).

The role that stabilization techniques play in the solution of the MREIT convection equation is better understood when experimental results are investigated. For the first experimental setup with an insulated region in the phantom, when neither a low-pass filter is applied to measured data nor any stabilization technique is utilized, the reconstructed conductivity suffers from oscillations and is relatively unstable as shown in Figure 3.7(a) and (b). However when either a low-pass filter is applied to measurement data or SUPG stabilization technique is utilized, a smoother conductivity is obtained. The best result is obtained when both the low-pass filter and SUPG stabilization technique are used. Similar observations are made regarding the results obtained for the second experimental setup for which two anomalous regions with higher and lower conductivity with respect to the background exist in the phantom. Therefore, we think, by way of introducing artificial diffusion, SUPG acts to avoid oscillations in regions where the solution has sharp variations.

In all reconstructions made using both simulated and experimental data the conductivity values at the boundary are assumed to be known. In experiments

conducted by phantoms this information is available since the conductivity of background solution is known. Furthermore in experiments that would be conducted using human or animal subjects, the information is available when large carbon hydro-gel electrodes are used or the subject is covered with conductive gel pads with appropriate conductivity [51].

Seo *et al.* (2003) have also proposed an $\nabla^2 B_z$-based algorithm for the reconstruction of conductivity and later it was modified and named as Harmonic B_z algorithm as discussed in Section 1.3 [34, 35]. This is an iterative algorithm and at each iteration the equation $\widetilde{\mathbf{E}} \cdot \nabla\sigma = \frac{\nabla^2 B_z}{\mu_0}$, where $\widetilde{\mathbf{E}} = [-E_y \; E_x]^{\mathrm{T}}$ and E_x, E_y are the x- and y- components of the electric field, is used. At the first iteration $\widetilde{\mathbf{E}}$ is calculated for a uniform conductivity distribution and for other iterations it is calculated using the conductivity from the previous iteration. This equation is in the same convection equation form as the equation $\widetilde{\mathbf{J}} \cdot \nabla R = \frac{\nabla^2 B_z}{\mu_0}$ that we used in this study. Therefore the solution methods that we have suggested can also be applied to reconstruct the conductivity at each iteration of Harmonic B_z algorithm.

As discussed in Section 1.3 [34, 35], some previously proposed algorithms for MREIT utilize either $\widetilde{\mathbf{E}} \cdot \nabla\sigma = \frac{\nabla^2 B_z}{\mu_0}$ [34, 35] or $\widetilde{\mathbf{J}} \cdot \nabla R = \frac{\nabla^2 B_z}{\mu_0}$ [37] to first calculate $\nabla\sigma$ or ∇R and then from the gradient information they use an line integral method [34] or layer potential technique [34, 37] to reconstruct σ or R. In these algorithms, in order to calculate the distribution of $\nabla\sigma$ or ∇R, one needs to apply at least two orthogonal current injections. However using our method, reconstructions for single current injection are also possible. On the other hand, calculation of distribution of $\nabla\sigma$ or ∇R give other information as well. Namely, if electric field or current density for two current injections are collinear at a spatial location then the 2×2 matrix obtained to solve for $\nabla\sigma$ or ∇R becomes ill-conditioned. In such a situation, regularization techniques are used to estimate the gradient. In our method, stabilization techniques are used

in the FEM formulation for the whole domain and we think these techniques act as a sort of regularization for ill-conditioned cases.

İder and Onart previously proposed an algorithm based on the finite difference discretization of $\widetilde{\mathbf{J}} \cdot \nabla R = \frac{\nabla^2 B_z}{\mu_0}$ [36]. However, the method proposed in this study uses FEM and the triangular mesh of the solution domain provides a more handy method for real objects with irregular boundary.

There are many FEM software packages which use advanced numerical techniques for the solution of partial differential equations. Comsol Multiphysics is one of these packages and it has a module for solving the convection-diffusion equation which also employs stabilization techniques. Although Comsol Multiphysics cannot solve the MREIT convection equation using two current injections, the $\mathbf{K}_1$, $\mathbf{K}_2$ matrices and the $\mathbf{b}_1$, $\mathbf{b}_2$ vectors in Equation 3.5 can be imported from the Comsol environment for two current injections separately as done in this study. The final matrix system is solved by Matlab using SVD. We think the possibility of using FEM software packages in the implementation of the algorithm is one of its advantages.

Before developing the *MREIT based on the solution of the convection equation* algorithm, we had proposed another MREIT algorithm, namely *triangular mesh based MREIT* [52], whereby the conductivity distribution is reconstructed at nodes of a triangular mesh by solving Equation 3.2. In this algorithm, the projected current density [19] is utilized in Equation 3.2 and the projected current density is reconstructed by the proposed *triangular mesh based MRCDI* algorithm. Although R values are defined on the nodes of the triangular mesh and ∇R is approximated using linear shape functions inside a triangle, the algorithm is not based on FEM. This algorithm is described and some simulation and experimental results are given in Appendix B. Although we have obtained satisfactory results for both the simulation and experiment cases considered, the theoretical foundation of the algorithm is yet to be investigated and we have not

developed a solid mathematical ground for the algorithm. Therefore we have decided to discuss the algorithm in the appendix rather than the mainstream of the manuscript.

Chapter 4

THREE-DIMENSIONAL FOURIER TRANSFORM MAGNETIC RESONANCE CURRENT DENSITY IMAGING (FT-MRCDI)

Some Fourier transform based MRCDI (FT-MRCDI) methods has been proposed before for two-dimensional (2D) problems where the current density has no z-component inside the object [20]-[22]. In this thesis, we have developed a novel MRCDI algorithm for three-dimensional problems. This chapter is devoted to the developed algorithm which we named "3D FT-MRCDI".

4.1 Methods

4.1.1 The Algorithm

The 3D FT-MRCDI method developed and presented in this thesis aims at estimating the difference current density using a Fourier transform formulation. It is a slice based method such that the 2D Fourier transforms are utilized rather than 3D Fourier transforms. Utilizing 3D Fourier transforms would require measurement of B_z in the whole 3D domain which is impractical and time-consuming. The starting point for the derivations is the two relations which are derived in Appendix B.1.2 for the estimate of the difference current density which is denoted by $\mathbf{J}^*$ (this terminology is also used by Park *et al.* [19]). The relations are given as:

$$\begin{aligned} &\frac{\partial J_x^*}{\partial y} - \frac{\partial J_y^*}{\partial x} = \frac{\nabla^2 B_z}{\mu_0} \quad \text{and} \\ &\frac{\partial J_x^*}{\partial x} + \frac{\partial J_y^*}{\partial y} = 0. \end{aligned} \tag{4.1}$$

The above relations may be written in spatial frequency domain using 2D Fourier transforms of J_x^*, J_y^* and $\nabla^2 B_z$ as

$$\begin{aligned} &j2\pi k_y \mathcal{F}_2\{J_x^*(x,y,t)\} - j2\pi k_x \mathcal{F}_2\{J_y^*(x,y,t)\} = \frac{\mathcal{F}_2\{[\nabla^2 B_z](x,y,t)\}}{\mu_0} \quad \text{and} \\ &j2\pi k_x \mathcal{F}_2\{J_x^*(x,y,t)\} + j2\pi k_y \mathcal{F}_2\{J_y^*(x,y,t)\} = 0. \end{aligned} \tag{4.2}$$

where $z = t$ at the imaging slice and 2D Fourier transform of J_x^* is defined as $\mathcal{F}_2\{J_x\}(k_x,k_y) = \int\limits_{\mathbb{R}^2} J_x(x,y,t)\mathrm{e}^{-j2\pi(k_x x + k_y y)}\mathrm{d}x\mathrm{d}y$ and the definitions for other Fourier transforms are similar. Combining these two equations, the relations for the $J_x{}^*$ and $J_y{}^*$ in the spatial frequency domain are obtained as

$$\begin{aligned} &\mathcal{F}_2\{J_x^*(x,y,t)\} = -\tfrac{1}{2\pi} j k_y \tfrac{1}{k_x^2+k_y^2} \tfrac{\mathcal{F}_2\{[\nabla^2 B_z](x,y,t)\}}{\mu_0} \quad \text{and} \\ &\mathcal{F}_2\{J_y^*(x,y,t)\} = \tfrac{1}{2\pi} j k_x \tfrac{1}{k_x^2+k_y^2} \tfrac{\mathcal{F}_2\{[\nabla^2 B_z](x,y,t)\}}{\mu_0} \end{aligned} \tag{4.3}$$

The expressions $-\frac{1}{2\pi}jk_y\frac{1}{k_x^2+k_y^2}$ and $-\frac{1}{2\pi}jk_y\frac{1}{k_x^2+k_y^2}$, which are multiplier to the Fourier transform of $\nabla^2 B_z$ in Equation 4.3, may be named as "inverse filters" and magnitude of the filters are shown in Figure 4.1. Thus, starting from the measurement of $\nabla^2 B_z$ at $z = t$ one can find estimates for $J_x^d(x, y, t)$ and $J_y^d(x, y, t)$ currents at that slice. These are estimates because we have made the assumption that $\frac{\partial J_z^d}{\partial z}(x, y, t)$ is negligible, as discussed in Section B.1.2. Of course, as evident from Equation 3.7, calculation of $\nabla^2 B_z$ at $z = t$ requires at least the measurement of B_z at $z = t$, $z = t + \delta$, and $z = t - \delta$ with δ chosen to be sufficiently small so that $\frac{\partial^2 B_z}{\partial^2 z}$ can be calculated at $z = t$.

Let Ω denote the interior of the imaging slice (the region of the $z = t$ plane which is inside the imaging object), Γ denote its boundary, and Ω_L denote a sufficiently large region such that $\Omega \subset \Omega_L$. Fourier transforms are evaluated in Ω_L. $\nabla^2 B_z = 0$ outside Ω but it may not be zero on Γ, as evident from the relation $\frac{\nabla^2 B_z}{\mu_0} = \frac{\partial J_x}{\partial y} - \frac{\partial J_y}{\partial x}$ (this is actually Equation 1.4). Since J_x and J_y are zero just outside Ω, their derivatives will have jumps on Γ when evaluated by a discrete approximation. However it is not possible to calculate $\nabla^2 B_z$ on Γ because this requires the measurement of B_z slightly outside of Ω. 3D FT-MRCDI algorithm is as follows:

1. $\nabla^2 B_z$ is calculated in Ω from the measured B_z. On Γ, $\nabla^2 B_z$ is taken equal to its immediate value in Ω. $\nabla^2 B_z$ in $(\Omega_L \setminus (\Omega \cup \Gamma))$ is taken as zero since no conductivity change occurs in this region. As a result, $\nabla^2 B_z$ in whole Ω_L is obtained and this data is the input of the first iteration.

2. $\mathcal{F}_2\{[\nabla^2 B_z](x, y, t)\}$ is calculated and inverse filters are used to calculate Fourier transform of currents in Ω_L. Inverse Fourier transform is then used to calculate currents in the spatial domain.

3. The outside-to-inside ratio (ϕ) of currents, which is defined as the ratio of sum of magnitudes of the reconstructed current in $(\Omega_L \setminus \Omega)$ to the sum of

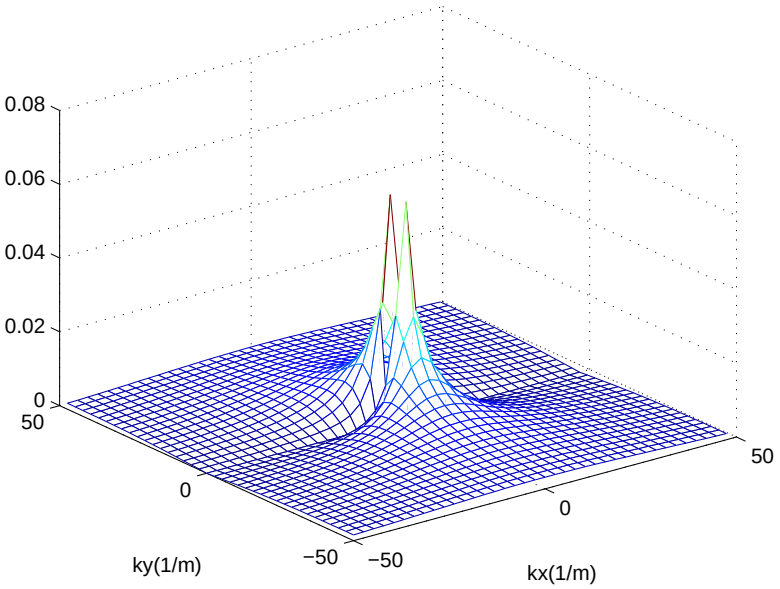

(a)

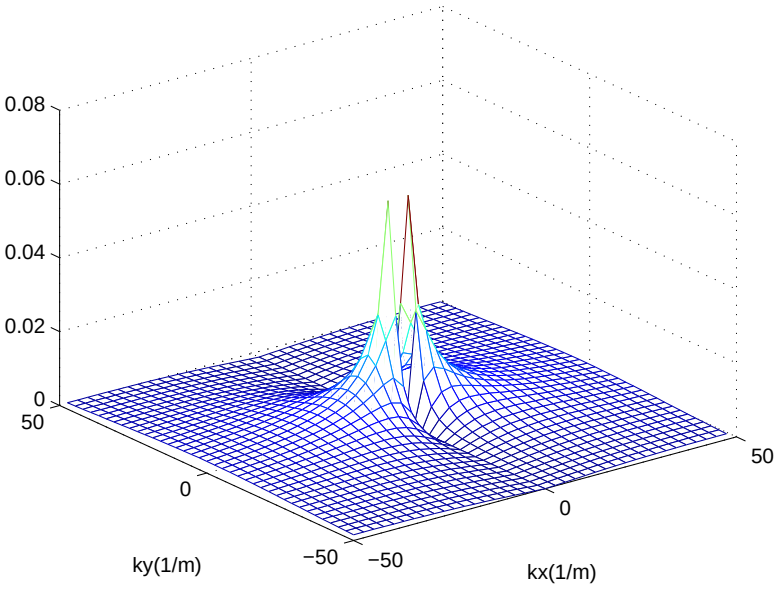

(b)

Figure 4.1: Magnitudes of inverse filters: (a) $-\frac{1}{2\pi}jk_y\frac{1}{k_x^2+k_y^2}$ (b) $-\frac{1}{2\pi}jk_x\frac{1}{k_x^2+k_y^2}$

magnitudes of the reconstructed current in Ω, is calculated. ϕ defines a stopping criteria for the algorithm.

4. If the difference of the two ϕ ratios in consecutive iterations are close enough, the algorithm stops. Otherwise, the currents are nulled for $(\Omega_L \backslash \Omega)$ and $\nabla^2 B_z$ is calculated from $\frac{\nabla^2 B_z}{\mu_0} = \frac{\partial J_x}{\partial y} - \frac{\partial J_y}{\partial x}$ in Ω and on Γ. Values of $\nabla^2 B_z$ calculated on Γ are retained but the measured values are assigned to $\nabla^2 B_z$ in Ω (obviously with this procedure $\nabla^2 B_z$ becomes 0 outside of Ω) and steps 2 to 4 are repeated with the newly obtained $\nabla^2 B_z$.

It is important to note that once the $\mathbf{J}^*$ is reconstructed via the proposed algorithm, one may calculate the "projected current density" from the relation $\mathbf{J}^P = \mathbf{J}^* + \mathbf{J}^0$ where $\mathbf{J}^0$ is the current density when homogeneous conductivity is assumed inside the object and may be calculated by solving the forward problem discussed in Section 1.2.1. The name "projected current density" is given by Park *et al.* [19] and since $\mathbf{J}^*$ is an estimate for the actual difference current density $\mathbf{J}^P$ is an estimate for the actual current density.

4.1.2 Simulation and Experimental Methods

The simulation phantom is modeled using Comsol Multiphysics software package in order to solve for electric potential in the 3D forward problem explained in Section 1.2.1 and the same simulation phantom described in Section 3.1.2 is used for the simulations. Furthermore the same methods discussed in Section 3.1.2 are used for calculating $\nabla^2 B_z$ and for calculating the L^2-errors made in the reconstructions.

For the experiments done for 3D-FTMRCDI, two experimental setups which are discussed in Section 3.1.3 are used. Therefore, in the first experimental setup, a balloon, which is filled with the background solution and which have electrically no connection to background solution, is used inside the phantom as

an insulator. On the other hand, in the second experimental setup, two agar objects which have lower and higher conductivity than the background solution is used inside the experimental phantom. Other experimental methods, including the calculation of $\nabla^2 B_z$ from measured B_z and the MRI parameters, are also the same with the methods discussed in Section 3.1.3.

4.2 Simulation Results

In the following, simulation results are given for the simulation phantom discussed in Section 3.1.2. For this phantom, simulated $\nabla^2 B_z$ data, actual conductivity distribution and actual difference current density distribution ($x-$ and $y-$ components) were shown before in Figure 3.2.

Figure 4.2 shows the simulation results which are obtained using the 3D-FTMRCDI algorithm. In Figure 4.2(a) and (b), the initial $\nabla^2 B_z$ which is input to the algorithm and the $\nabla^2 B_z$ which is reconstructed after the tenth iteration are shown respectively. On the boundary (Γ), $\nabla^2 B_z$ has built up at the end of the tenth iteration. The magnitude of reconstructed $\mathbf{J}^*$ at the recessed regions are low compared to the $\mathbf{J}^*$ reconstructed inside the object as seen in Figure 4.2(c) and (d). Therefore, as evident from the relation $\frac{\partial J_x}{\partial y} - \frac{\partial J_y}{\partial x} = \frac{\nabla^2 B_z}{\mu_0}$, we observe that, the $\nabla^2 B_z$, which is built on the recessed sections of the boundary by the algorithm, is low compared to the other sections of the boundary.

It is also of interest to observe the behavior of reconstructed $\mathbf{J}^*$ as iterations proceed. Figure 4.2(e) and (f) show the magnitude of the reconstructed $\mathbf{J}^*$ at the first and tenth iterations respectively (the figures are drawn at the same color scale). Although, at the first iteration, significant amount of reconstructed $\mathbf{J}^*$ is located outside of the object ($\phi = 2.44\%$), after the tenth iteration, reconstructed $\mathbf{J}^*$ is more confined to the inside of the object ($\phi = 0.59\%$). Actually, the build up of the $\nabla^2 B_z$ on Γ, is what forces the reconstructed $\mathbf{J}^*$ to be inside the object.

Therefore, as iterations proceed, the reconstructed $\mathbf{J}^*$ becomes more confined to the inside of the object, in other words, becomes more close to the actual difference current density and thus both the L^2-error made in the reconstruction of the $\mathbf{J}^*$ and the ϕ ratio decreases simultaneously. In Figure 4.3(a) and (b) iteration number vs. the L^2-error made in the reconstruction of the $\mathbf{J}^*$ and iteration number vs. the ϕ ratio are shown respectively. While the L^2-error is 22.79% at the first iteration it is 21.00% after the tenth iteration. The L^2 error is 23.59% when Park's method is used. The L^2-error and the ϕ ratio follows each other as iterations proceed which proves that observing the ϕ ratio is a good stopping criteria for the algorithm. Although no significant improvement is achieved after the fifth iteration (ϕ ratio stays almost constant), we continued until the tenth iteration to guarantee that no further improvements in the L^2-error is possible. It is important to remember that we do not expect the L^2-error to be close to zero since $\mathbf{J}^*$ is only an estimate in a 3D problem and this error is strictly related to $\frac{\partial J_z^d}{\partial z}(x, y, t)$.

The algorithm is also tested when the $\nabla^2 B_z$ given to the algorithm at the first iteration has non-zero regions closer to the boundary. Inside the simulation phantom, the same two objects are used but the centers of the objects are located at $(-0.021, -0.021)$ and $(0.021, 0.021)$ respectively. In Figure 4.4(a) and (b) the conductivity distribution and the quiver plot of the actual difference current density are shown at the imaging slice for this case and Figure 4.5 shows the reconstruction results. If the non-zero part of $\nabla^2 B_z$ is closer to the boundary, then the reconstructed $\mathbf{J}^*$ at the outside of the object is much higher at the first iteration ($\phi = 5.99\%$) as can be observed in Figure 4.5(c) and (d). The L^2-error made in the reconstruction of $\mathbf{J}^*$ and the ϕ ratio are shown in Figure 4.3(c) and (d) respectively as iterations proceed. While the L^2-error is 29.06% at the first iteration it is 25.57% after the tenth iteration. The decrease in the L^2-error and the ϕ ratio as iterations proceed is observed better for this case. However the final L^2-error is higher than the previous simulation case.

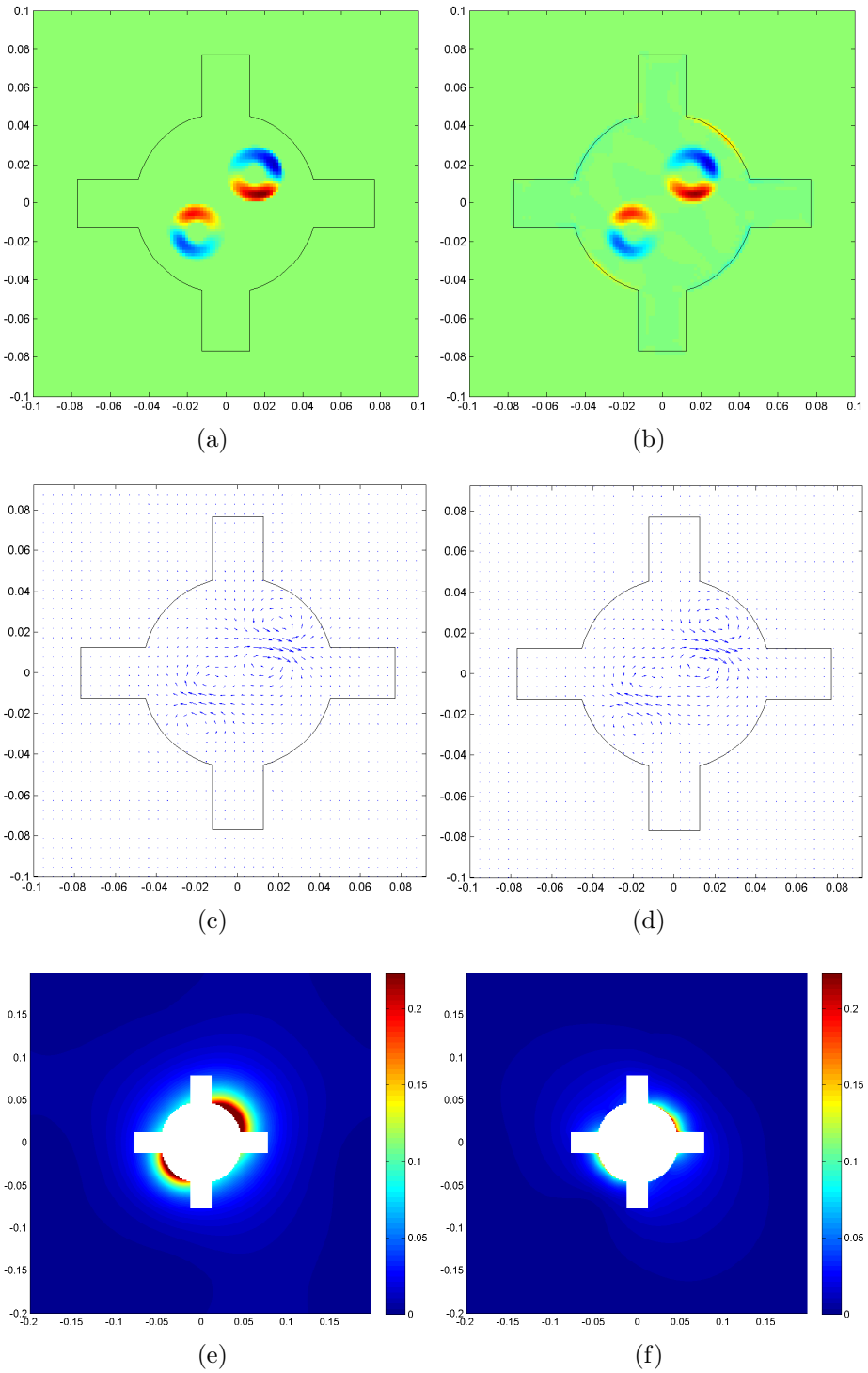

Figure 4.2: Simulation results for the 3D FT-MRCDI: (a) initial $\nabla^2 B_z$ (input to the algorithm), (b) $\nabla^2 B_z$ reconstructed at the tenth iteration, (c, d) quiver plot of the reconstructed $\mathbf{J}^*$ at the first and tenth iterations respectively, (e, f) magnitude of the reconstructed $\mathbf{J}^*$ at the first and tenth iterations respectively (The region inside the object is nulled to emphasize the decrease of the magnitude outside the object throughout the iterations).

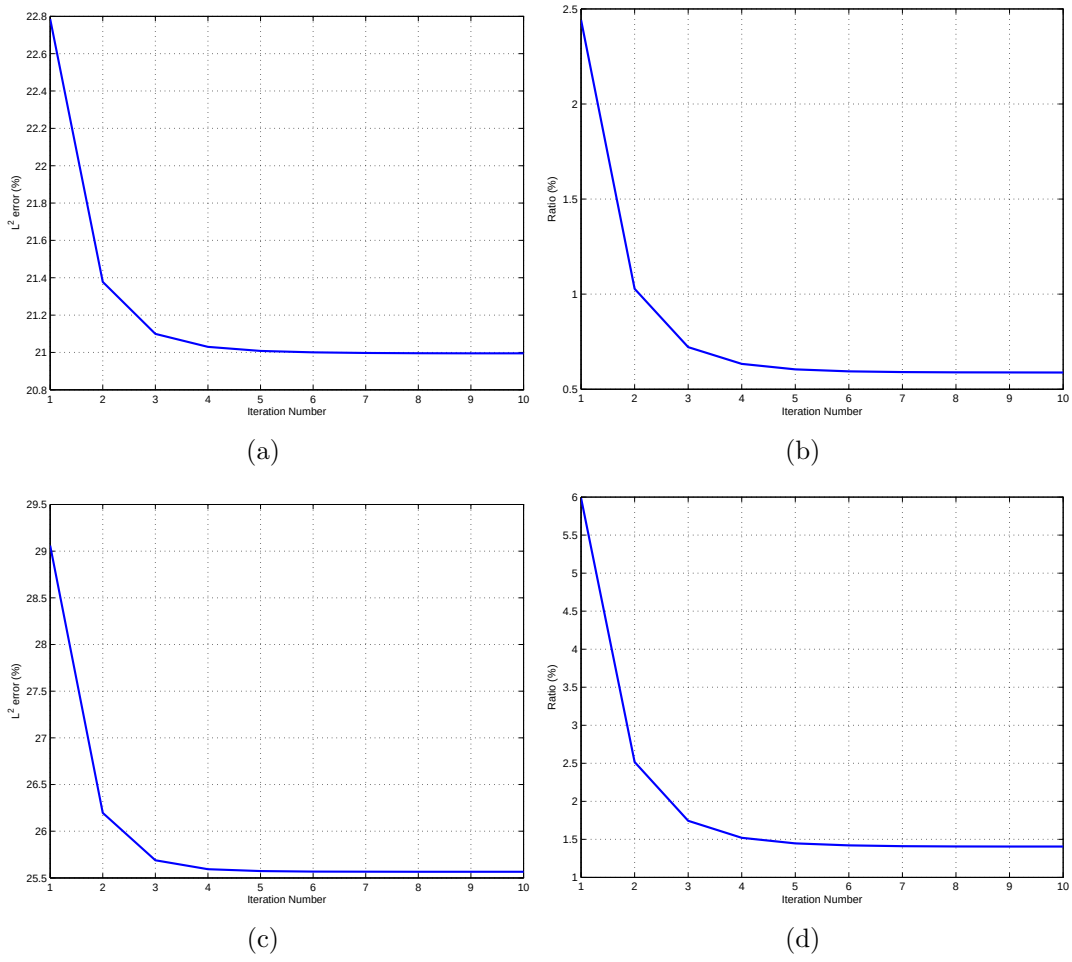

Figure 4.3: The L^2-error made in the reconstruction of $\mathbf{J}^*$ and the ϕ ratio as iterations proceed for two different simulation cases. (a) and (b) are drawn for the first simulation case explained in Section 3.1.2. (c) and (d) are drawn for the simulation case in which the non-zero regions of $\nabla^2 B_z$ is closer to the boundary.

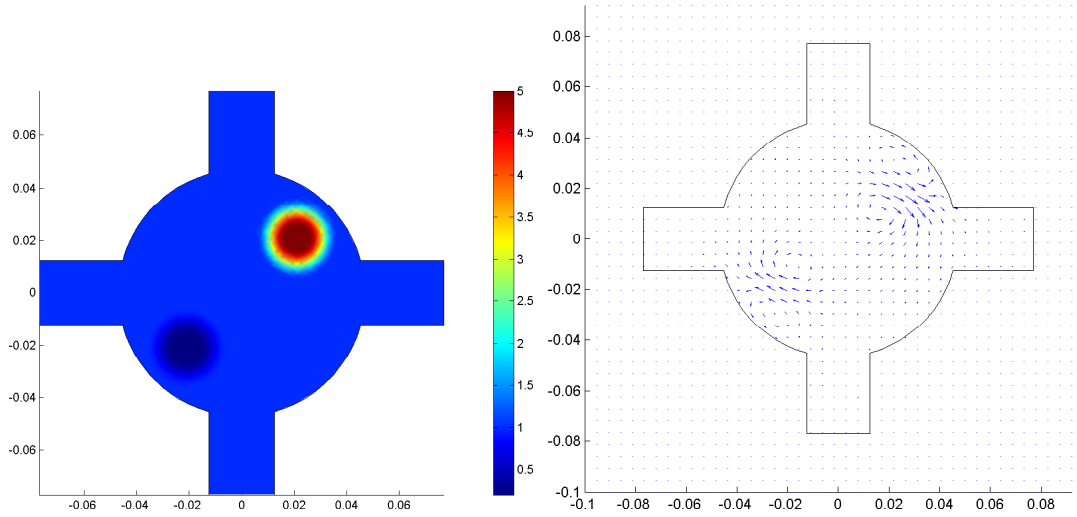

(a) (b)

Figure 4.4: Conductivity distribution((a)) and the quiver plot of actual difference current density((b)) for the simulation case in which the non-zero regions of $\nabla^2 B_z$ is closer to the boundary.

The success of the proposed algorithm is also investigated when noise is added to the simulated $\nabla^2 B_z$. In order to simulate the noise in $\nabla^2 B_z$ data, a similar procedure explained in Section 3.2.1, is followed. The simulation results are given in Figure 4.6 when $SNR = 180$. It is evident from Figure 4.1 that the inverse filters have a low-pass character. Therefore, $\nabla^2 B_z$ which is reconstructed in Ω in the fourth step of the last iteration is the low-pass filtered version of the initial $\nabla^2 B_z$. This situation can only be observed when the input data is noisy or have high frequency components. Otherwise the effect of the low-pass inverse filters are not seen. Figure 4.6(a) show the initial $\nabla^2 B_z$ which is noisy and Figure 4.6(b) show the $\nabla^2 B_z$ obtained in the fourth step of the last iteration. $\nabla^2 B_z$ has built up on Γ and when $\nabla^2 B_z$ in Ω is observed, the low-pass filter effect which is mentioned above is seen. After seven iterations the algorithm stops since the stopping criteria is met and the L^2-error made in the reconstruction of $\mathbf{J}^*$ is 28.80%. The L^2-error is 37.29% when $SNR = 120$, and 46.24% when $SNR = 90$.

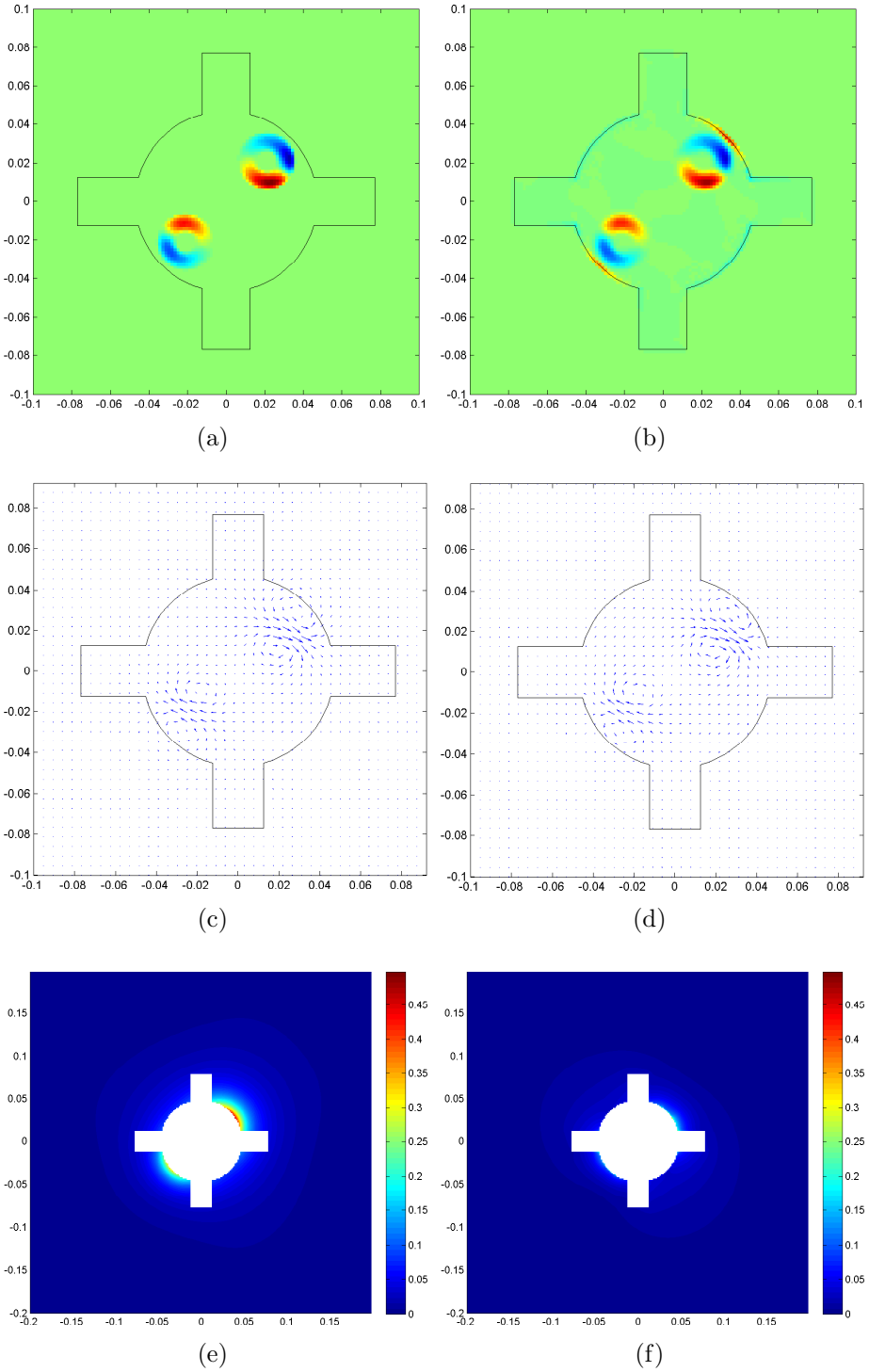

Figure 4.5: Simulation results for the 3D FT-MRCDI when the non-zero regions of $\nabla^2 B_z$ is closer to the boundary : (a) initial $\nabla^2 B_z$ (input to the algorithm), (b) $\nabla^2 B_z$ reconstructed at the tenth iteration, (c, d) quiver plot of the reconstructed $\mathbf{J}^*$ at the first and tenth iterations respectively, (e, f) magnitude of the reconstructed $\mathbf{J}^*$ at the first and tenth iterations respectively (The region inside the object is nulled to emphasize the decrease of the magnitude outside the object throughout the iterations).

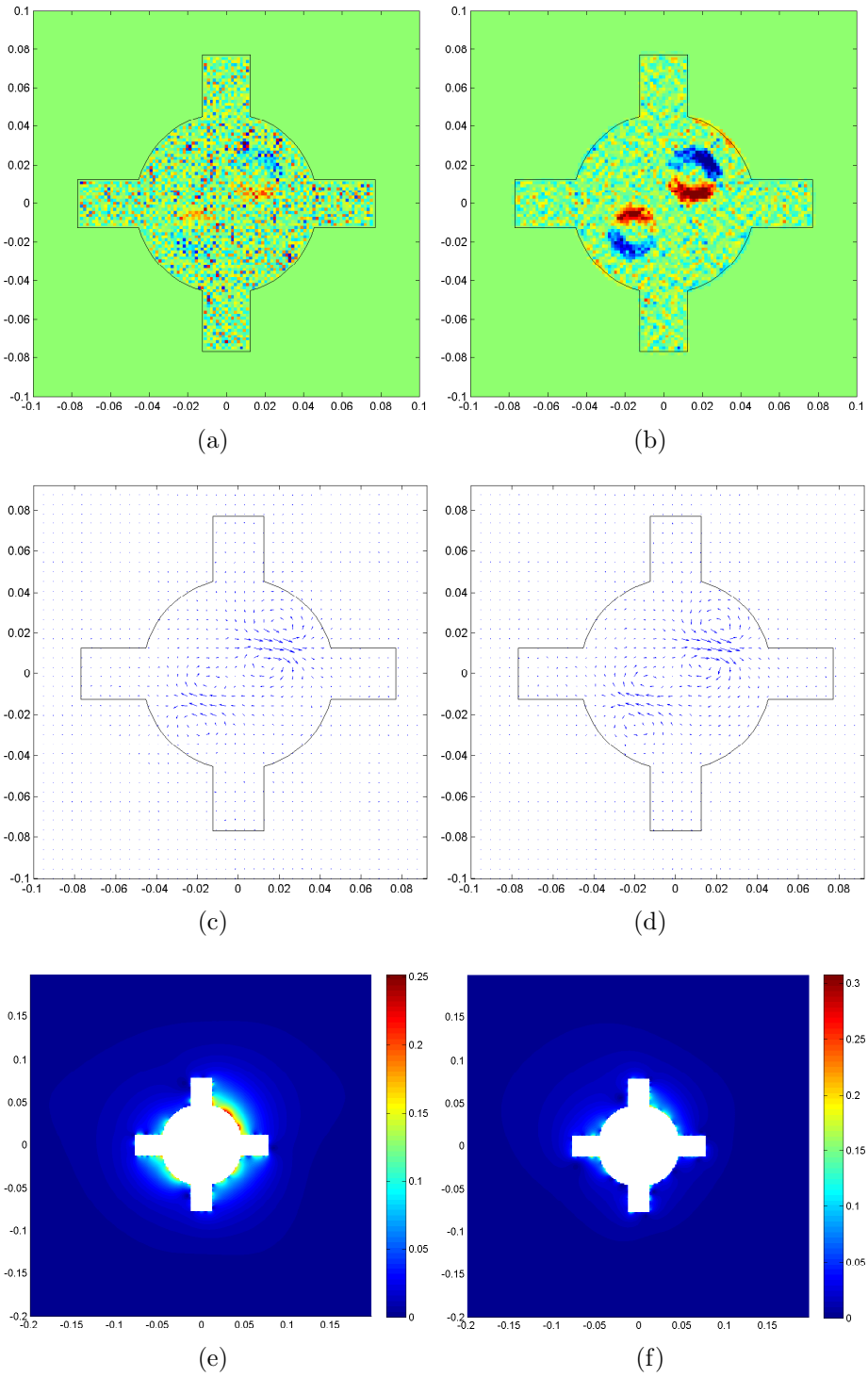

Figure 4.6: Simulation results for the 3D FT-MRCDI when noise is added to $\nabla^2 B_z$: (a) initial $\nabla^2 B_z$ (input to the algorithm), (b) $\nabla^2 B_z$ reconstructed at the tenth iteration, (c, d) quiver plot of the reconstructed $\mathbf{J}^*$ at the first and tenth iterations respectively, (e, f) magnitude of the reconstructed $\mathbf{J}^*$ at the first and tenth iterations respectively (The region inside the object is nulled to emphasize the decrease of the magnitude outside the object throughout the iterations).

4.3 Experimental Results

For the first experimental setup, Figure 4.7 shows the initial and final (after the eight iteration) $\nabla^2 B_z$, quiver plot of the reconstructed $\mathbf{J}^*$ after the first and the eighth iterations, and the magnitude of the reconstructed $\mathbf{J}^*$ at the outside region of the object. In order to emphasize the decrease of the reconstructed current density at the outside the object, the reconstructed current density inside the object is nulled in Figure 4.7(e) and (f). For the second experimental setup, the same results are given in Figure 4.9.

The algorithm stops after eight iterations for the first experimental setup and after seven iterations for the second experimental setup. Iteration number vs. the ϕ ratio is given in Figure 4.8 (a) and (b) respectively for two experimental setups. The algorithm stops since the difference between the ϕ ratios in two consecutive algorithms are close enough.

The differentiation process during the calculation of $\nabla^2 B_z$ amplifies high spatial frequency components of B_z which leads to the amplification of the noise inherent in B_z measurements. Therefore, as done in the experiments for the convection equation based MREIT, a Hanning window low pass filter is applied to the $\nabla^2 B_z$ data in the frequency domain. The $\nabla^2 B_z$ data given in Figures 4.7 and 4.9 are low-pass filtered versions of the original data. The Hanning window is $w(k_x, k_y) = 0.5(1 - \cos \frac{\pi k}{k_{max}})$ where k_x and k_y are spatial frequencies in x and y directions respectively [47]. Since in the first experimental setup an insulator is used the contrast of the $\nabla^2 B_z$ is higher than the second experimental setup. Therefore, although for the first experimental setup k_{max} is chosen to be 400 m$^-$1, for the second experimental setup k_{max} is chosen to be 300 m$^-$1.

For both experimental setups, it is observed that the numerical error in the calculated $\nabla^2 B_z$ is most pronounced in recessed parts of the phantom since B_z

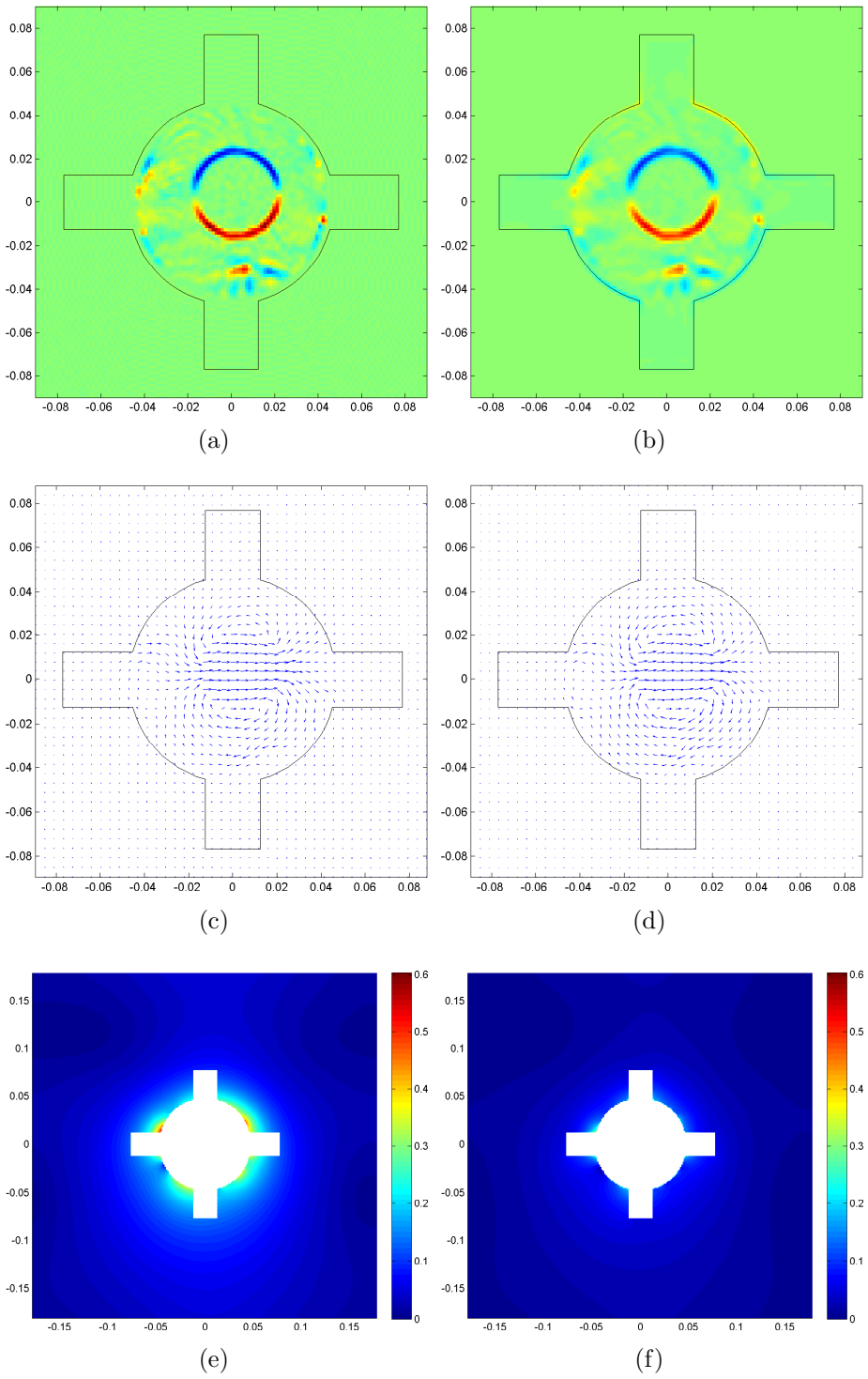

Figure 4.7: Experimental results for the first experimental setup: (a) initial $\nabla^2 B_z$ (input to the algorithm), (b) $\nabla^2 B_z$ at the eighth iteration, (c, d) quiver plot of the reconstructed $\mathbf{J}^*$ at the first and eighth iterations respectively, (e, f) magnitude of the reconstructed $\mathbf{J}^*$ at the first and eighth iterations respectively (The region inside the object is nulled to emphasize the decrease of the magnitude outside the object throughout the iterations).

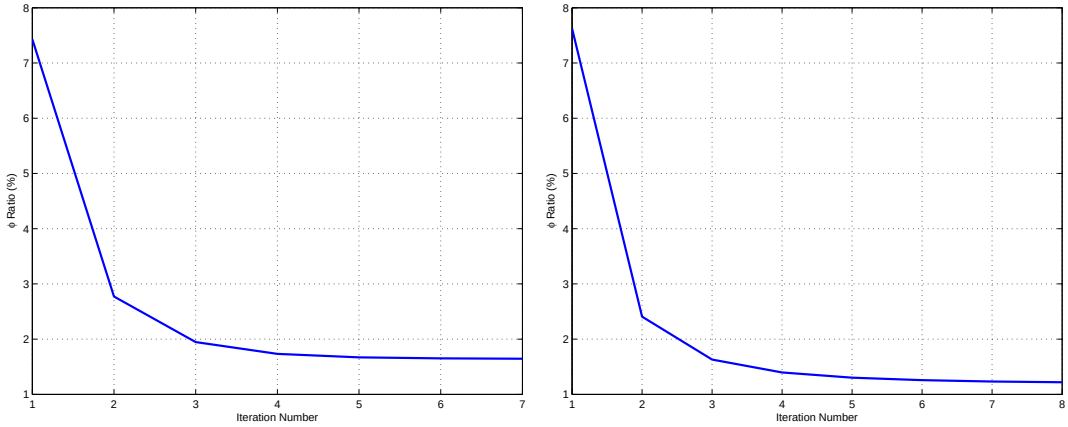

(a) (b)

Figure 4.8: The iteration number versus the ϕ ratio: (a) the first experimental setup, (b) the second experimental setup.

changes rapidly and also has high magnitude in these regions. Also B_z measurements near the boundary of the phantom have relatively high noise probably due to the partial volume effect in MR voxels here. Therefore, as done in the experiments for the convection equation based MREIT, $\nabla^2 B_z$ data is masked such that only $\nabla^2 B_z$ calculated on the circular region of radius 0.045 m is used and outside of this region, including recessed parts, $\nabla^2 B_z$ is taken as zero in the calculations (it is known that $\nabla^2 B_z = 0$ in these regions since the conductivity is constant).

4.4 Discussion

In this chapter, an iterative Fourier transform based MRCDI algorithm for 3D problems is proposed. The algorithm is capable of reconstructing the current density at a desired slice from the $\nabla^2 B_z$ data obtained for that slice only. To reconstruct an estimate for the difference current density ($\mathbf{J}^*$), the relation between the difference current density and $\nabla^2 B_z$ is utilized in spatial frequency domain. Furthermore the divergence-free condition of the difference current density is also considered for obtaining inverse filters. Successful reconstructions

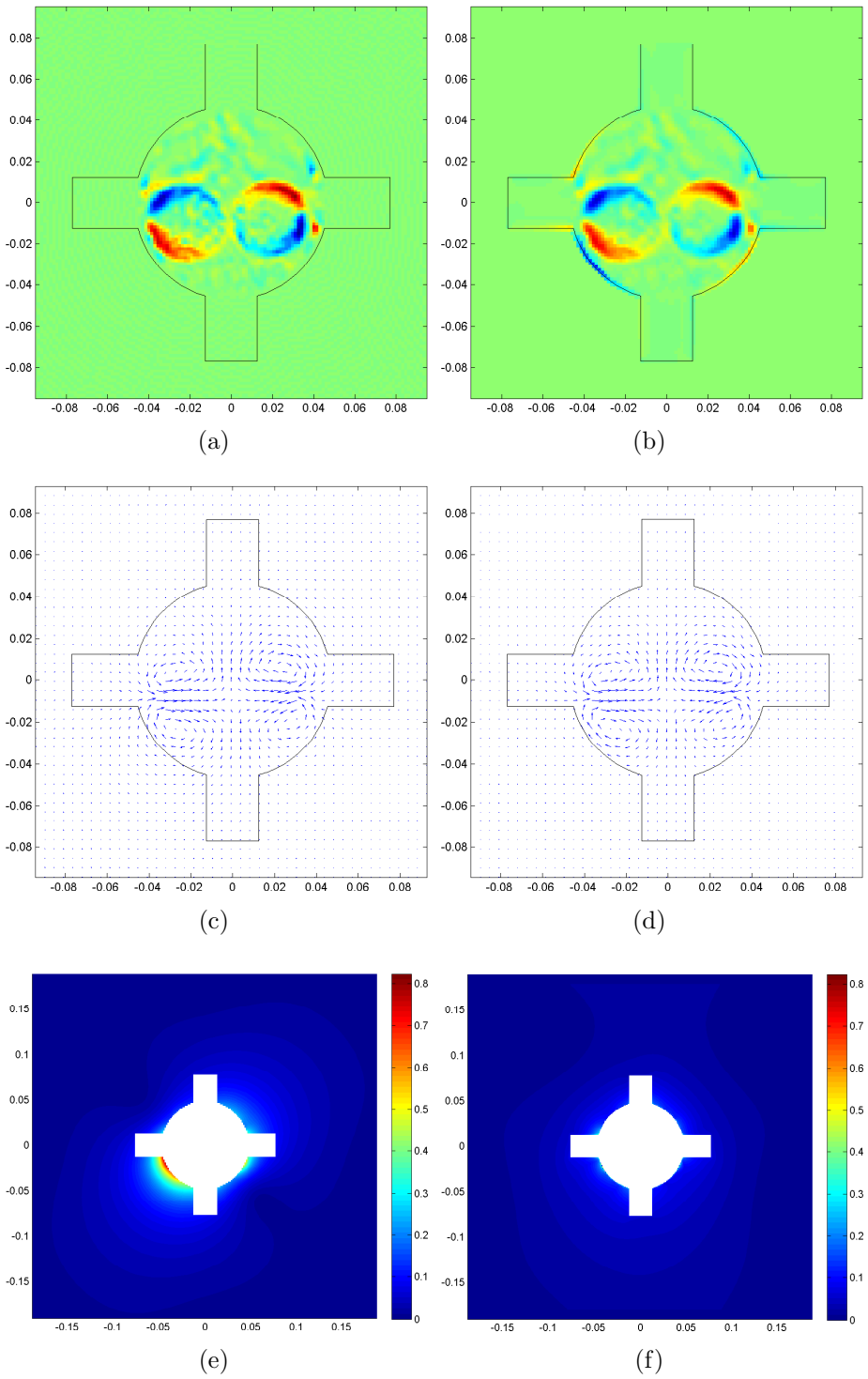

Figure 4.9: Experimental results for the second experimental setup: (a) initial $\nabla^2 B_z$ (input to the algorithm), (b) $\nabla^2 B_z$ at the seventh iteration, (c, d) quiver plot of the reconstructed $\mathbf{J}^*$ at the first and seventh iterations respectively, (e, f) magnitude of the reconstructed $\mathbf{J}^*$ at the first and seventh iterations respectively (The region inside the object is nulled to emphasize the decrease of the magnitude outside the object throughout the iterations).

which are obtained from both simulated and experimental data are presented. The performance of the algorithm against measurement noise of B_z is also investigated and successful reconstructions are obtained when different amount of noise is added to the input data. To our knowledge, the algorithm is the only Fourier transform based MRCDI algorithm for 3D problems.

Fourier transform methods for 2D MRCDI have also been proposed. Lee *et al.* and Oh *et al.* considered a special geometry in which one component of the magnetic flux density is related to one component of current only [20, 21]. While in the study of Lee *et al.* current has z-component only, in the study of Oh *et al.* , current is predominantly in the z direction. It is known that $\mathcal{F}_3\{J_z\} = 2\pi j k_x \mathcal{F}_3\{H_y\} - 2\pi j k_y \mathcal{F}_3\{H_x\}$. Assuming that H_z is negligible, and since magnetic flux density is divergence free, and assuming that μ is uniform, one obtains $2\pi j k_x \mathcal{F}_3\{H_x\} + 2\pi j k_y \mathcal{F}_3\{H_y\} = 0$. Therefore one can relate $\mathcal{F}_3\{J_z\}$ to $\mathcal{F}_3\{H_x\}$ only. Thus the methods developed in by Lee *et al.* and Oh *et al.* are not applicable to the 3D problems considered in this study. Other investigators have used Fourier transform methods for the CDI problem in which the magnetic field is measured outside the object using non-MRI methods [47, 53, 54]. Pesikan *et al.* have also used Fourier domain methods for the CDI problem and they have used MRI to measure the magnetic field but their measurements are confined to a region away from the current sources [55].

Park *et al.* have analyzed the recovery of current density in a 3D object [19]. They have developed a theory whereby the "projected current" density is calculated from $\nabla^2 B_z$ data. Their algorithm for finding the "projected current density" was discussed in Section 3.1.1. The theory of Park *et al.* and the 3D FT-MRCDI technique presented in this chapter are closely related. Park *et al.* have developed their theory for reconstructions from $\nabla^2 B_z$ data directly. Let $f(x, y)$ denote the $\nabla^2 B_z/\mu_0$ which is measured at $z = 0$. Then from Park *et al.* theory $(\frac{\partial^2}{\partial x^2} + \frac{\partial^2}{\partial y^2})\beta(x, y, 0) = f(x, y)$ and in the Fourier domain

$-4\pi^2(k_x^2+k_y^2)\mathcal{F}_2\{\beta(x,y,0)\} = \mathcal{F}_2\{f\}$. Therefore $\mathcal{F}_2\{J_x^*\} = j2\pi k_y \frac{\mathcal{F}_2\{f\}}{-4\pi^2(k_x^2+k_y^2)} = -\frac{jk_y}{2\pi(k_x^2+k_y^2)}\mathcal{F}_2\{f\}$ and $\tilde{J}_y^* = \frac{jk_x}{2\pi(k_x^2+k_y^2)}\mathcal{F}_2\{f\}$. These expressions are identical to what we have stated in Equation 4.3.

The method developed in this study is more suitable for the problem of induced current MRCDI [56]. In induced current MRCDI current is not injected but is induced by an applied magnetic field. Thus the current density in the object is divergence free both inside and also on the boundary. In such a scenario, the current density itself is reconstructed rather than the difference current density.

Chapter 5

CONCLUSIONS

In this thesis, two new reconstruction algorithms one for MREIT and one for MRCDI are proposed. Handling MREIT reconstruction problem, based on the solution of the convection equation is a new approach. The convection-diffusion type of problems arises in many areas, especially in fluid dynamics, and solving the convection-diffusion equation is, therefore, of broad interest. In MREIT, physically no convection nor diffusion mechanisms exist. However, from a mathematical point of view, the main equation for $\nabla^2 B_z$-based MREIT is a convection equation. When the convection is dominant in the problem or the problem is of pure convection type as in our case, the numerical solution of the convection-diffusion equation is not trivial due to instability of the numerical solution in certain cases. The numerical solution of the convection equation has been an active research area for decades and numerous stabilization techniques has been proposed. In this study, these techniques are also investigated and utilized for the numerical solution of the MREIT convection equation. We believe that handling the MREIT problem as a convection problem provides a useful insight about the problem.

Considering the simulation and experimental results for *MREIT based on the solution of the convection equation* algorithm we conclude that for the case of two orthogonal current injections, the SUPG stabilization technique is beneficial when there is noise in the measured magnetic flux density data or when there are sharp variations in conductivity of the object at the imaging slice. The SUPG stabilization technique is beneficial in the sense that it substantially decreases the L^2-error made in the reconstruction and provides more stable solutions (no spurious oscillations are seen in the solution).

We have also shown that SUPG stabilization technique can be used to reconstruct conductivity from only one current injection. When one current injection is used the magnitude of the current in some region may be low which causes these regions to be ill defined. However SUPG stabilization technique introduces much more artificial diffusions for these regions and a stable solution of the problem is possible.

In the proposed algorithm for MREIT, we have used SUPG stabilization technique for MREIT convection equation. However there are some other stabilization techniques as well. In the future, we would also investigate other stabilization techniques for MREIT convection equation. Every stabilization technique has its own advantages in different cases and we would like to compare the results from different stabilization techniques quantitatively. Furthermore, more than one stabilization technique might be applied at the same time.

For MRCDI, the proposed algorithm is a Fourier transform based algorithm and the reconstruction is made in the spatial frequency domain. The proposed algorithm is developed for 3D problems. Reconstruction of the current density at a desired slice is possible using the $\nabla^2 B_z$ data only at the desired slice. Once the discrete Fourier transforms in the algorithm are calculated using "Fast Fourier Transform" the reconstruction process is simply element-wise multiplication of

inverse filter matrix and the Fourier transform of currents (x- and y- components). Therefore the algorithm is fast and very easy to implement. We think this is the most important advantage of the algorithm.

The study involving MREIT based on the solution of the convection equation is submitted for publication [57]. Furthermore, 3D FT-MRCDI algorithm presented in this thesis is published in [22] (in this paper we have presented only simulation results for 3D problems). *Triangular mesh based MRCDI and MREIT* algorithm and experimental results for 3D FT-MRCDI algorithm were presented in *Workshop on MR-based Impedance Imaging*, Seoul, Korea [52, 58].

APPENDIX A

Stabilization Techniques for the Solution of Convection-Diffusion Equation

The general form of the scalar stationary convection-diffusion equation may be written as

$$\beta \cdot \nabla u + \nabla \cdot (k \nabla u) = F \tag{A.1}$$

where β is the divergence-free convective field, k is the diffusion coefficient, u is the scalar quantity which is distributed under the effect of diffusion and convection, and F is the source term. A measure of how relatively the convective term is dominant is given by element Péclet number which is defined as $Pe = \|\beta\| \, h/(2c)$ where h is the finite element size. A larger Péclet number means the convection is more dominant in the equation than the diffusion. It is known that if the solution contains sharp variations then there will be local disturbances in the regions where $Pe > 1$ which leads to spurious oscillations in the solution. Furthermore the solution may be purely oscillatory in the case of pure convection equation ($Pe = \infty$). To illustrate the concept of stability of the convection-diffusion

equation, consider a simple one-dimensional problem which is given as

$$\beta \frac{\mathrm{d}u(x)}{\mathrm{d}x} + k \frac{\mathrm{d}^2 u(x)}{\mathrm{d}x^2} = 1 \tag{A.2}$$

The problem is to be solved with FEM in the range $0 \leq x \leq 1$ with 97 elements and Dirichlet boundary conditions are used at both ends, and with β taken as 1. If $k = 0$ the problem is purely convective and in this case, if consistent boundary conditions are chosen (e.g. $u(0) = 0$, $u(1) = 1$), the problem may be solved with the standard FEM with Galerkin weighted residual formulation as seen in Figure A.1(a). On the other hand, if the boundary conditions are inconsistent (e.g. $u(0) = 0$, $u(1) = 0$) then the boundary condition on the right ($u(1) = 0$) will cause a sharp variation on the solution near the right boundary. In this case, solving the equation with Galerkin formulation will gives a pure oscillatory unstable solution as seen in Figure A.1(b). To stabilize the solution a diffusion term may be added to the equation. Such a diffusion is often called artificial diffusion. Let the artificial diffusion term be $\tilde{k} \frac{\mathrm{d}^2 u(x)}{\mathrm{d}x^2}$. Choosing $\tilde{k} = 0.5 \left\| \beta \right\| h$ is natural for a pure convective equation since this guarantees that $Pe = 1$ in the whole domain. For this example this choice gives $\tilde{k} = 1/194$ since β is constant and Figure A.1(c) shows the solution for this choice. Adding too much artificial diffusion however (e.g. $\tilde{k} = 10/194$) introduces too much smoothing effect as shown Figure A.1(d).

For two-dimensional problems, it would be enough to introduce artificial diffusion in only one particular direction to stabilize the solution and therefore $\tilde{k}$ may be anisotropic. A number of stabilization techniques that introduce artificial diffusion in the direction of convective field (upwind) or in the direction perpendicular to the convective field (crosswind) has been suggested in the literature. One popular stabilization technique is streamline upwind Petrov-Galerkin (SUPG) [46]. SUPG uses the special Petrov-Galerkin shape functions in the Galerkin weighted residual FEM formulation. It is explained below that the

SUPG procedure is equivalent to adding a diffusion term to the pure convection equation.

In order to introduce artificial diffusion only in the upwind direction, the pure convection equation can be modified by adding a diffusion term with $\tilde{k}_{i,j} = 0.5h\beta_i\beta_j / \|\beta\|$ as a tensor. In this case, let $\mathbf{A}_1$ denote the N $\times$ N matrix (N is the number of nodes in the triangular mesh) which is obtained from the FEM with Galerkin weighted residual formulation of the modified equation such that $\mathbf{A}_1\mathbf{u} = \mathbf{b}_1$, where $\mathbf{u}$ is the vector denoting u values on the nodes and $\mathbf{b}_1$ vector is obtained from the source term. The SUPG technique, which uses the Petrov-Galerkin shape functions, gives a different system equation $\mathbf{A}_2\mathbf{u} = \mathbf{b}_2$. It is known that $\mathbf{A}_1$ matrix is the same with $\mathbf{A}_2$ matrix [48] but $\mathbf{b}_1$ and $\mathbf{b}_2$ are not the same. Therefore SUPG method has the properties of introducing artificial upwind diffusion and it is also consistent in the sense that Petrov-Galerkin shape functions are applied to both sides of the convection equation.

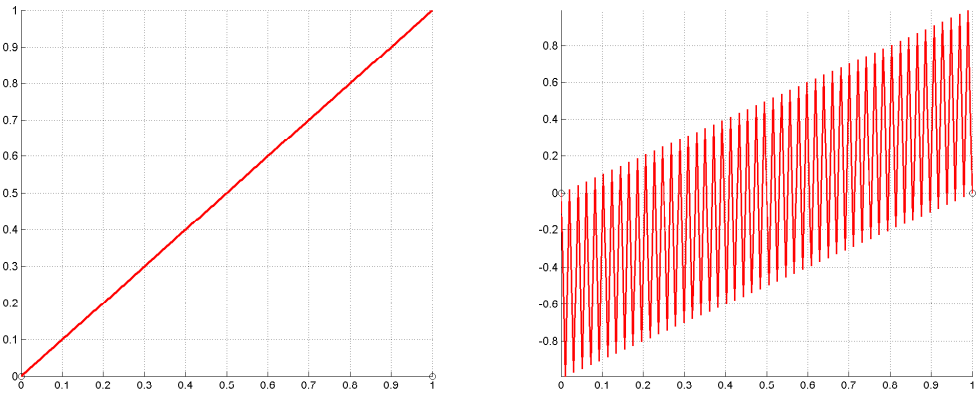

(a) (b)

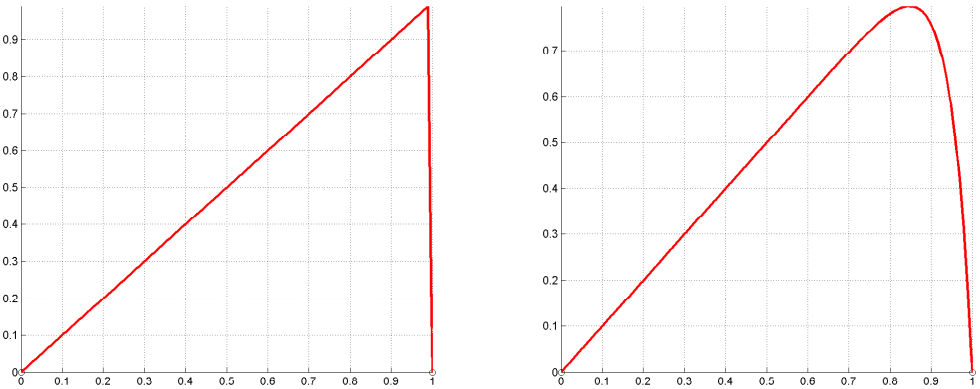

(c) (d)

Figure A.1: The solution of equation (A.2): (a) $\beta = 1$, $k = 0$ and $u(0) = 0$, $u(1) = 1$ (b) $\beta = 1$, $k = 0$ and $u(0) = 0$, $u(1) = 0$ (c) $\beta = 1$, $k = 1/194$ and $u(0) = 0$, $u(1) = 0$ (d) $\beta = 1$, $k = 10/194$ and $u(0) = 0$, $u(1) = 0$

APPENDIX B

Triangular Mesh Based MRCDI and MREIT

B.1 Methods

B.1.1 Background Information

Let f be a scalar function defined on the nodes of a triangular mesh, then the function can be approximated in a triangular element as

$$f(x,y) = \sum_{i=1}^{3} f_i \alpha_i(x,y) \tag{B.1}$$

where f_i is the value of function at the i'th node and $\alpha_i(x,y)$ is the linear shape function for the i'th node which is defined as $\alpha_i(x,y) = a_i + b_i x + c_i y$. The coefficients a_i, b_i and c_i can be obtained by using the definition that $\alpha_i(x_j, y_j) = 1$ if $i = j$ and $\alpha_i(x_j, y_j) = 0$ otherwise where (x_j, y_j) is the coordinates of the j'th node $(i, j = 1, 2, 3)$. Once the coefficients are known, it is easy to see derivative of f with respect to x and y as

$$\frac{\partial f(x,y)}{\partial x} = \sum_{i=1}^{3} f_i b_i \tag{B.2}$$

$$\frac{\partial f(x,y)}{\partial y} = \sum_{i=1}^{3} f_i c_i \tag{B.3}$$

inside an element.

B.1.2 The Triangular Mesh Based MRCDI

As discussed in Section 3.1.1, the actual current density ($\mathbf{J}$) consists of two components, namely $\mathbf{J}^0$ and $\mathbf{J}^d$, where $\mathbf{J}^0$ is the current density distribution for the homogenous conductivity distribution and $\mathbf{J}^d$ is defined as the difference current density such that $\mathbf{J}^d = \mathbf{J} - \mathbf{J}^0$. Since $\nabla^2 B_z = 0$ for $\mathbf{J}^0$ (refer Equation 1.5) with the algorithms which utilize $\nabla^2 B_z$ data, including the triangular mesh based MRCDI, only an estimation to $\mathbf{J}^d$ can be reconstructed. However $\mathbf{J}^0$ can be calculated by solving the forward problem given in Section 1.2.1 for homogeneous conductivity.

Two relations are utilized in the triangular mesh based MRCDI for reconstructing an estimation to difference current density. As discussed in Section 1.3, this is an estimation because only one component of the magnetic flux density is available. The first relation which is between the current density ($\mathbf{J}$), and the Laplacian of the B_z ($\nabla^2 B_z$) was derived in Section 1.2.2 as

$$\frac{\partial J_x}{\partial y} - \frac{\partial J_y}{\partial x} = \frac{\nabla^2 B_z}{\mu_0}. \tag{B.4}$$

The second relation is derived as follows. Let $\mathbf{J}^0$ be the current density distribution obtained from solving 3D forward problem defined in Section 1.2.1 when a uniform conductivity is assumed in the object. It is clear from Equation 1.5 that $\nabla^2 B_z$ is zero when the conductivity distribution is uniform. Thus, (B.4) also holds for the difference current density which is defined as ($\mathbf{J}^d = \mathbf{J} - \mathbf{J}^0$) and Furthermore, it is known that the difference current density holds the divergence-free condition:

$$\frac{\partial J_x^d}{\partial x} + \frac{\partial J_y^d}{\partial y} + \frac{\partial J_z^d}{\partial z} = 0 \tag{B.5}$$

Assuming that the conductivity change in the z direction is negligible, third term in on the left-hand side of (B.5) can be omitted. In this case, a current density holding (B.5) and (B.4) can be defined. This current density will be an estimation to the actual difference current density and named as $\mathbf{J}^*$ by Park *et al.* [19]. Therefore $\mathbf{J}^*$ is the solution to

$$\frac{\partial J_x^*}{\partial y} - \frac{\partial J_y^*}{\partial x} = \frac{\nabla^2 B_z}{\mu_0} \tag{B.6}$$

and

$$\frac{\partial J_x^*}{\partial x} + \frac{\partial J_y^*}{\partial y} = 0 \tag{B.7}$$

In the triangular mesh MRCDI method, (B.6) and (B.7) is solved on a triangular mesh on the imaging plane: Let J_x^* and J_y^* is defined on the nodes of the triangular mesh, then both of the two can be approximated inside a triangular element using (B.1). In this case, using (B.2) and (B.3), derivatives of J_x^* and J_y^* with respect to x and y can be obtained in terms of nodal J_x^* and J_y^* . Next, assuming $\nabla^2 B_z$ is constant inside an triangular element, (B.6) and (B.7) is written as

$$\sum_{i=1}^{3}(J_{x,i}^* c_i - J_{y,i}^* b_i) = \frac{\nabla^2 B_z}{\mu_0} \tag{B.8}$$

$$\sum_{i=1}^{3}(J_{x,i}^* b_i - J_{y,i}^* c_i) = 0 \tag{B.9}$$

where $J_{x,i}^*$ is the value of J_x^* at the i'th node and $J_{y,i}^*$ is similarly defined. Using (B.8) and (B.9) for each triangular element, an matrix equation is formed where the nodal J_x^* and J_y^* are unknowns. Since $\boldsymbol{J}^*$ is an estimation to the difference current density, it is known that the normal components of J_x^* and J_y^* on the boundary is zero and this condition is also considered by adding extra equations into the matrix system. The matrix system is then solved using the singular value decomposition.

B.1.3 The Triangular Mesh Based MREIT

The relation used for the triangular mesh based MREIT is the same with the relation used for the MREIT based on the solution of the convection equation (Equation 3.2) and given as

$$\nabla^2 B_z = \mu_0 (J_x \frac{\partial R}{\partial y} - J_y \frac{\partial R}{\partial x}). \tag{B.10}$$

where $R = \ln \sigma$. Using a similar strategy as the triangular mesh based MRCDI, R function can be approximated inside an element with nodal R values of the element using (B.1), and its derivatives with respect to x and y may be computed using (B.2) and (B.3). In this case, Equation B.10 can be written as

$$J_x(x,y) \sum_{i=3}^{3} R_i c_i - J_y(x,y) \sum_{i=3}^{3} R_i b_i = \frac{\nabla^2 B_z(x,y)}{\mu_0}. \tag{B.11}$$

In order to solve for nodal R, J_x and J_y must be known. Since the actual current density cannot be recovered from one component of magnetic flux density, projected current can be used. Projected current density is simply $\mathbf{J}^P = \mathbf{J}^* + \mathbf{J}^0$ and it may be calculated on nodes using the triangular mesh based MRCDI algorithm. Integrating $\mathbf{J}^P$ over the area of a triangle, one obtains the average of the three nodal $\mathbf{J}^P$, which may be assumed as the value for that element. (B.11) is then written as

$$\sum_{i=1}^{3} R_i (b_i J_y^P - c_i J_x^P) = \frac{\nabla^2 B_z}{\mu_0} \tag{B.12}$$

Writing (B.12) for all elements one can obtain a set of equations for nodal R values which then can be converted into a matrix equation. In order to obtain absolute values of conductivity distributions, the value of the conductivity must be known on at least one node. The obtained matrix equation may be modified to take known conductivity values into account. It was shown that at least two independent current injections are needed in order to reconstruct distinguishable conductivity distribution [29]. Thus, the obtained matrix equations for each independent current injections may be solved together in order to reconstruct a

unique conductivity distribution. For the solution of the matrix singular value decomposition is used.

B.1.4 Simulation and Experimental Methods

For both simulations and experiments, the same methods with *MREIT based on the solution of the convection equation* algorithm are used. Please refer Sections 3.1.2 and 3.1.3 for further information.

B.2 Results

B.2.1 Simulation Results

Simulated $\nabla^2 B_z$ data, actual difference current density distribution ($x-$ and $y-$ components), and $\mathbf{J}^*$ reconstructed using both the method proposed by Park *et al.* and explained in Section 3.1.1 and the triangular mesh based MRCDI are shown in Figure 3.2 for the simulation phantom. All images are drawn for the center transverse slice of the simulation phantom where $z = 0$ (named as imaging slice hereafter) and when current is injected in $\mathbf{I}_1$ direction shown in Figure 3.1(c). The relative L^2-error made in the reconstructed $\mathbf{J}^*$ is 23.59% for Park's method and 22.44% for triangular mesh based MRCDI. For other current injection direction ($\mathbf{I}_2$ direction shown in Figure 3.1(c)) the last two given L^2-errors are 23.18% and 22.05%. The proposed algorithm gives similar L^2-errors as Park's algorithm.

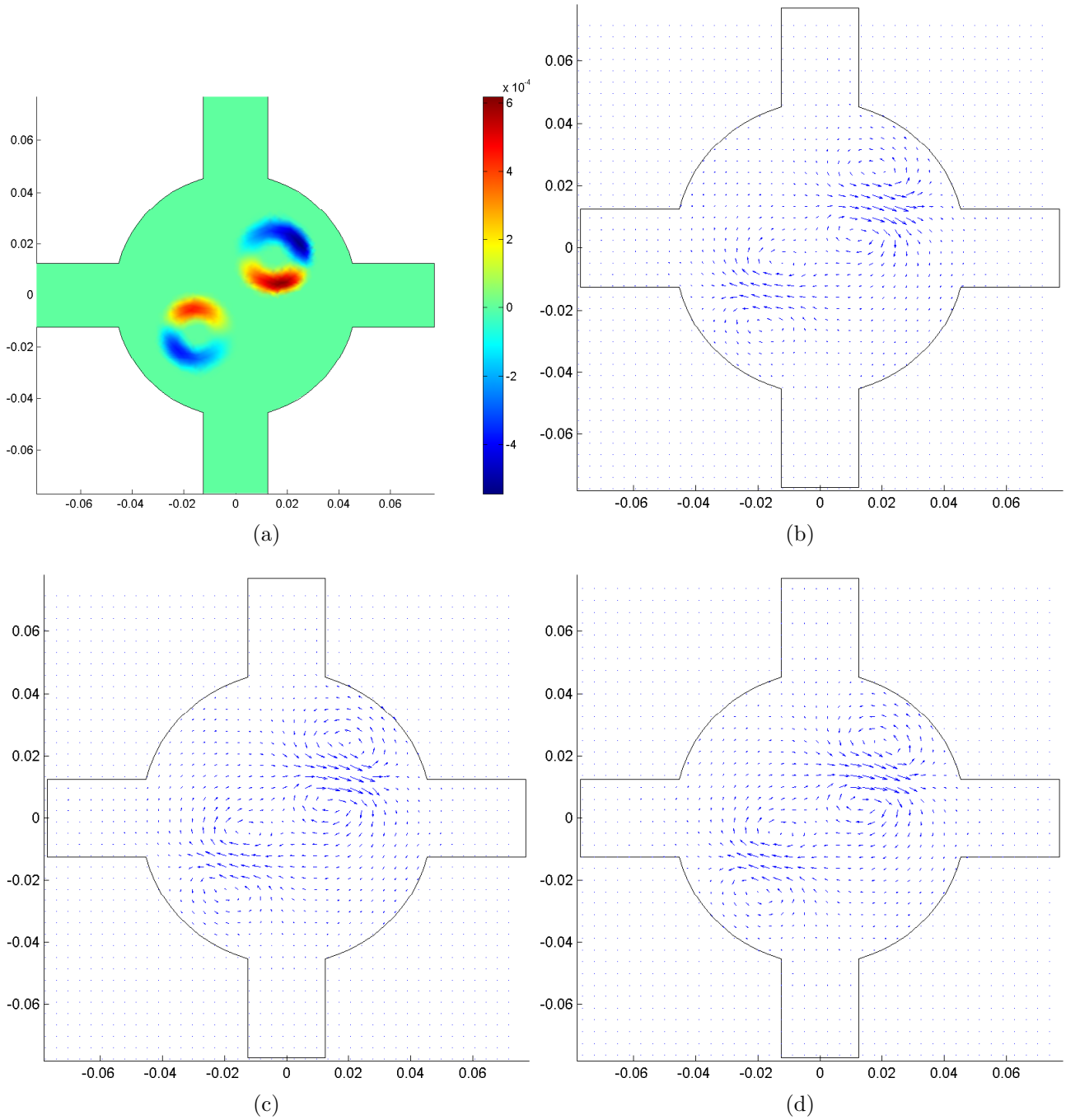

Figure B.1: Simulation results for the triangular mesh based MRCDI: (a) simulated $\nabla^2 B_z$, (b) quiver plot of the actual difference current density distribution ($x-$ and $y-$ components), (c) quiver plot of the $\mathbf{J}^*$ reconstructed using the method proposed by Park *et al.* , (d) quiver plot of the $\mathbf{J}^*$ reconstructed using the triangular mesh based MRCDI method.

Once $\mathbf{J}^*$ is reconstructed using the triangular mesh based MRCDI, the projected current density is calculated and the conductivity distribution is reconstructed using the triangular mesh based MREIT. Figure B.2(a) shows the reconstructed conductivity distribution at the imaging slice when two current injections are utilized. Conductivity values on the boundary are assumed to be 1 S/m ($R = 0$ since $R = \ln \sigma$). Figure B.2(b) show the reconstructed conductivity profile on the $x = y$ line of the imaging slice. The relative L^2-error made in the reconstructed conductivity is 2.12%. Since the projected current density is used, rather than the actual current density, this amount of error is reasonable in the numerical simulations (it is known that the conductivity distribution cannot be fully recovered from projected current).

Performance of the triangular mesh based MRCDI and MREIT against noise in B_z data is also investigated. The noisy B_z is calculated using the procedure explained in Section 3.2.1. Noisy $\nabla^2 B_z$ and $\mathbf{J}^*$ obtained from the noisy $\nabla^2 B_z$ using Park's method and triangular mesh based MRCDI are given in Figure B.3 when $SNR = 180$ and $T_C = 50ms$. The relative L^2-error made in the reconstruction of the $\mathbf{J}^*$ is 42.46% when Park's method is used and 43.05% when triangular mesh based MRCDI is used. For other current injection direction the last two given L^2-errors are 41.00% and 44.74%. When $\mathbf{J}^*$ reconstructed from the noisy $\nabla^2 B_z$ using triangular mesh based MRCDI is used, the reconstructed conductivity distribution and conductivity profile on the $x = y$ line are given at the imaging slice in Figure B.2(c) and (d). The relative L^2-error made in the reconstruction of the conductivity is 12.68% when SNR is 180, 15.47% when SNR is 120, and 17.08% when SNR is 90.

B.2.2 Experimental Results

Two experiment setup which are explained in Section 3.1.3 are also used for the triangular mesh based MRCDI and MREIT. While in the first experiment setup

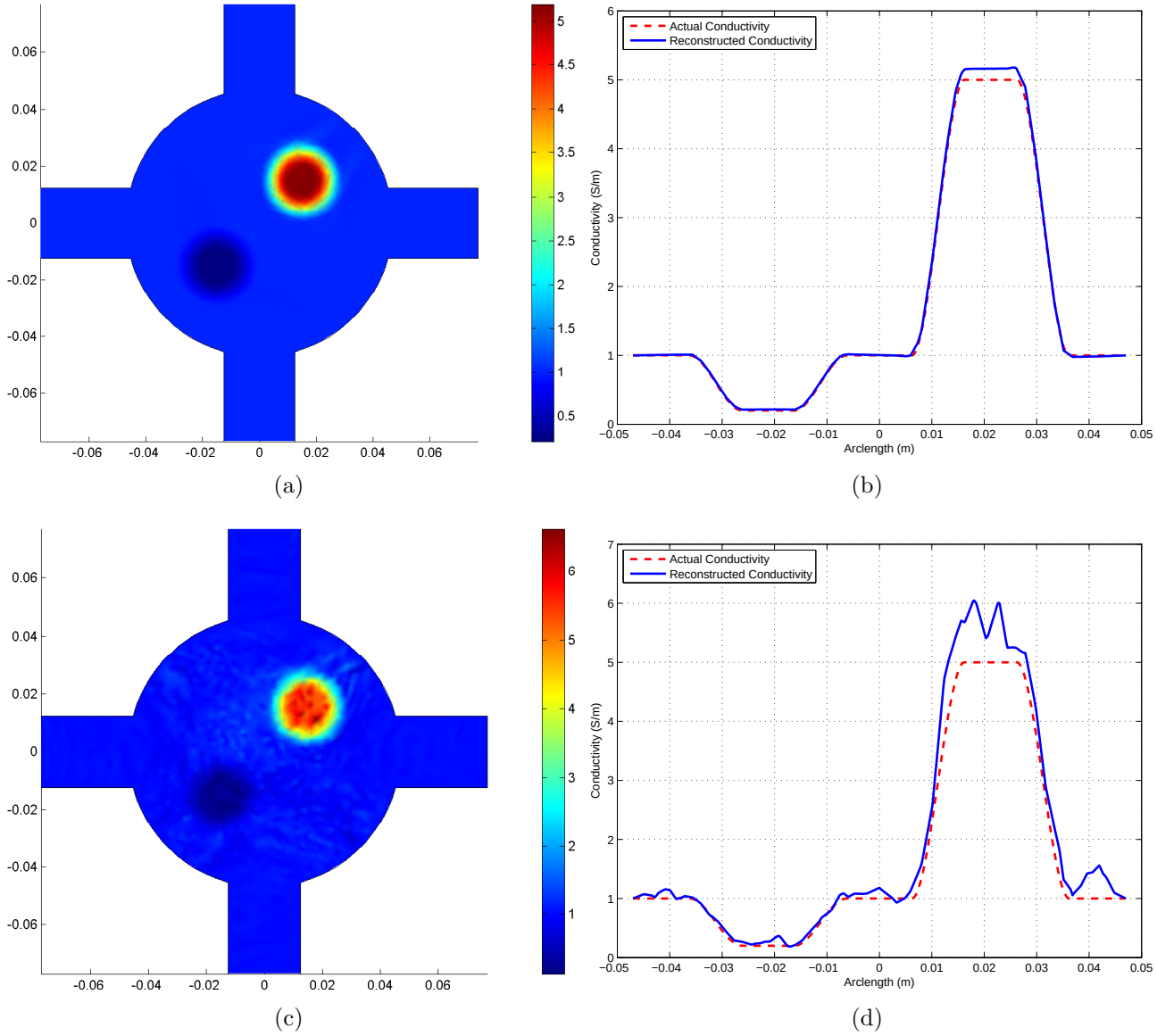

Figure B.2: Reconstructed conductivities using triangular mesh based MREIT in the simulations: (a) the reconstructed conductivity distribution at the center slice, (b) the reconstructed conductivity profile on the $x = y$ line at the center slice. (c) and (d) are same as (a) and (b) but reconstructions are made with noisy $\nabla^2 B_z$ ($SNR = 180$ and $T_C = 50ms$).

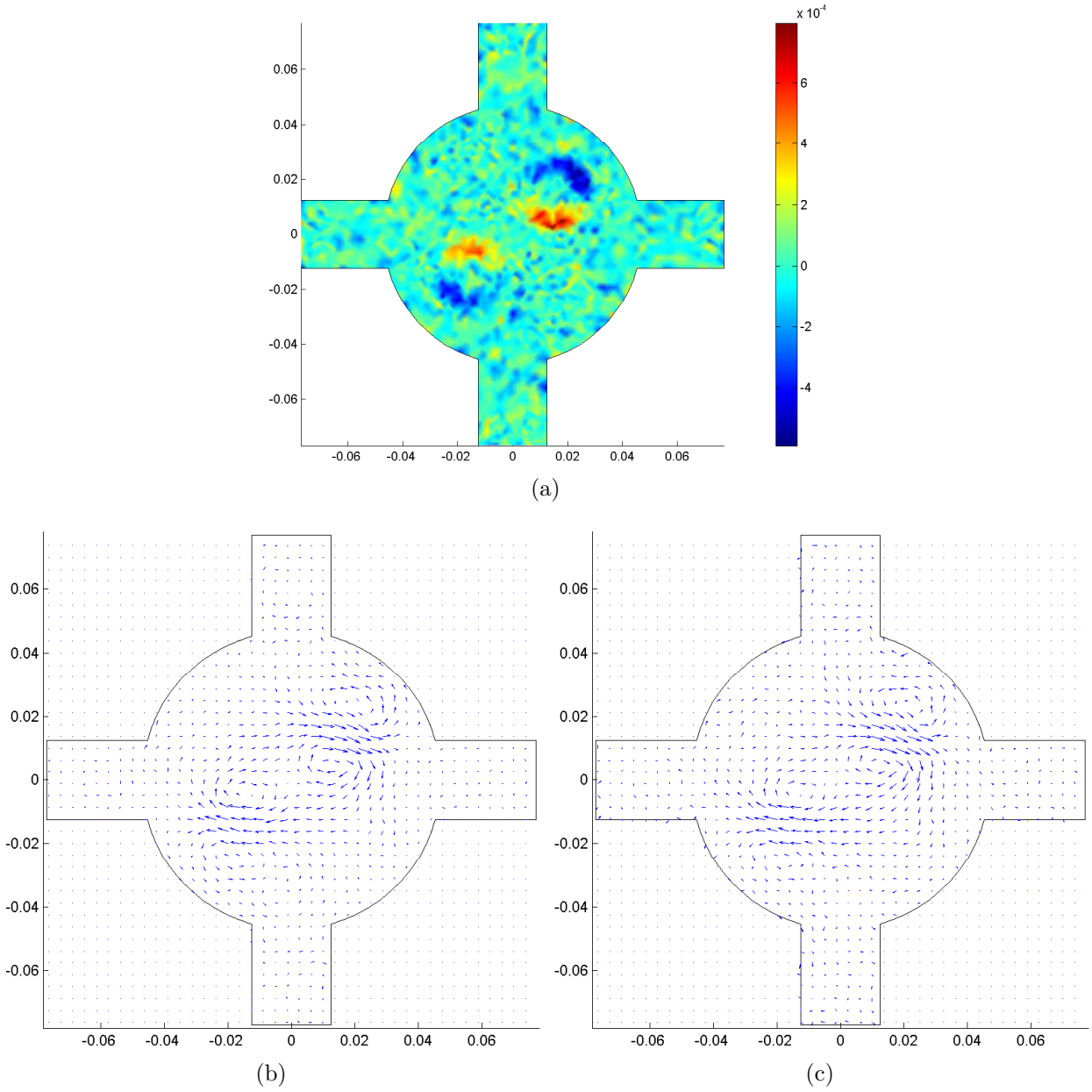

(a) (b) (c)

Figure B.3: Simulation results for the evaluation of the performance of the triangular mesh based MRCDI against noise: (a) Noisy $\nabla^2 B_z$ for $SNR = 180$ and $T_C = 50ms$, (b) quiver plot of $\mathbf{J}^*$ reconstructed using the method proposed by Park *et al.* from noisy $\nabla^2 B_z$, (c) quiver plot of the $\mathbf{J}^*$ reconstructed using the triangular mesh based MRCDI method from noisy $\nabla^2 B_z$.

an insulator object is used inside the phantom, in the second experiment setup two conductive agar objects are used in the phantom. Experimental results for the first experiment setup are given in Figure B.4. Figure B.4(a) and (b) show the $\mathbf{J}^*$ reconstructed using the triangular mesh based MRCDI for two current injection direction respectively and Figure B.4(c) shows the reconstructed conductivity using the triangular mesh based MREIT. Due to the reasons explained in Section 3.2.2, "masked" and filtered $\nabla^2 B_z$ is used for the reconstruction and k_{max} is taken as 400 m^{-1} for the first experiment setup and 300 m^{-1} for the second experiment setup. Masked and filtered $\nabla^2 B_z$ data for first and second experiment setups are shown in Figure 3.6 and 3.8 respectively. Experimental results for the second experiment setup are shown in Figure B.5. For the same experiment setup, the reconstructed conductivity, when MREIT based on the solution of the convection equation algorithm is used, was given in Figure 3.7. Comparing two algorithms we conclude that they give similar results.

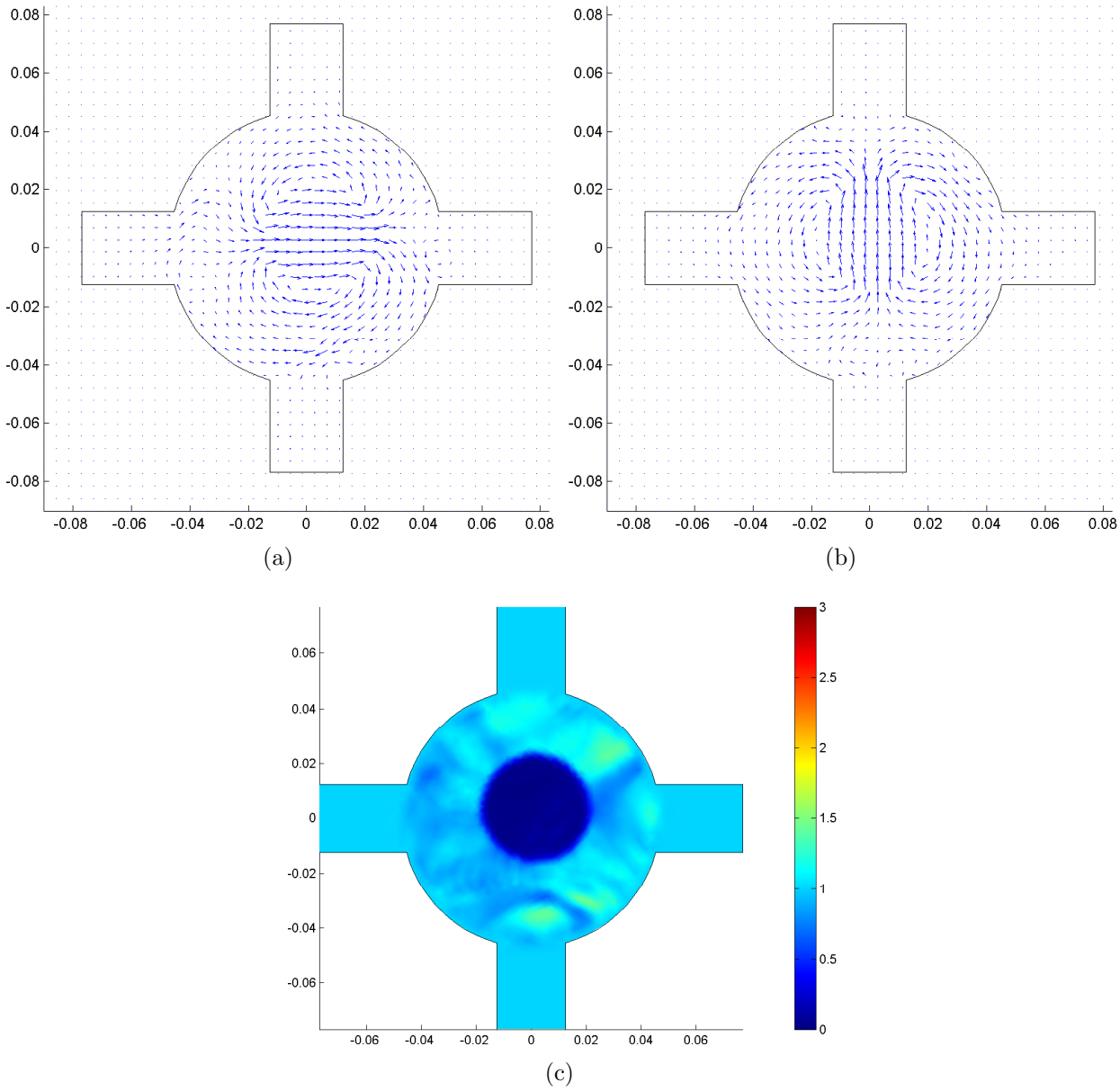

Figure B.4: Experimental results for the first experiment setup explained in Section 3.1.3: (a) and (b) are quiver plots of $\mathbf{J}^*$ at the center slice reconstructed using the triangular mesh based MRCDI method from noisy $\nabla^2 B_z$ for two current injection directions respectively, (c) is the conductivity distribution at the center slice reconstructed using the triangular mesh based MREIT.

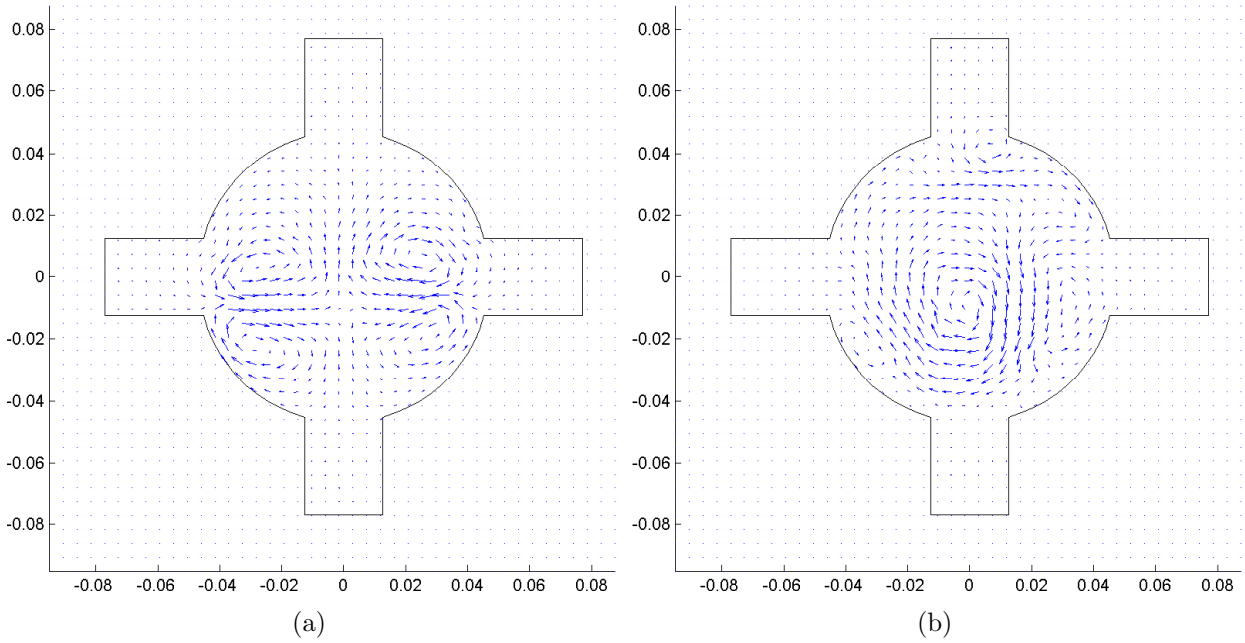

(a) (b)

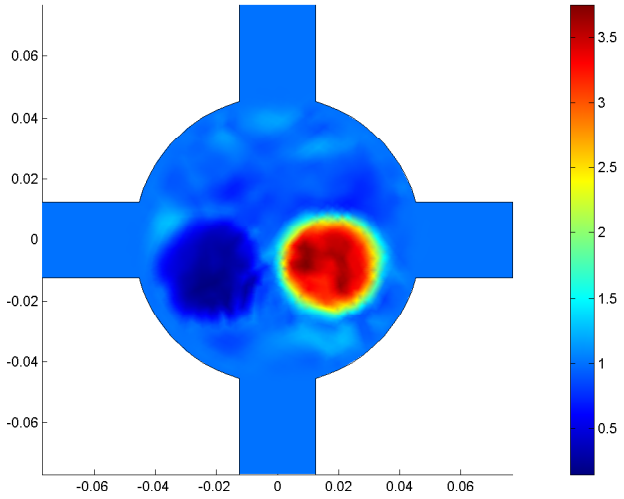

(c)

Figure B.5: Experimental results for the second experiment setup explained in Section 3.1.3: (a) and (b) are quiver plots of $\mathbf{J}^*$ at the center slice reconstructed using the triangular mesh based MRCDI method from noisy $\nabla^2 B_z$ for two current injection directions respectively, (c) is the conductivity distribution at the center slice reconstructed using the triangular mesh based MREIT.

Bibliography

[1] R. Pethig and D. B. Kell, "The passive electrical properties of biological systems: their significance in physiology, biophysics and biotechnology," *Physics in Medicine and Biology*, vol. 32, pp. 933–970, 1987.

[2] C. Gabriel, S. Gabriel, and E. Corthout, "The dielectric properties of biological tissues: I. Literature survey," *Physics in Medicine and Biology*, vol. 41, pp. 2231–2249, 1996.

[3] S. Gabriel, R. W. Lau, and C. Gabriel, "The dielectric properties of biological tissues: II. Measurements in the frequency range 10 Hz to 20 Ghz," *Physics in Medicine and Biology*, vol. 41, pp. 2251–2269, 1996.

[4] L. A. Geddes and L. E. Baker, "The passive electrical properties of biological systems: their significance in physiology, biophysics and biotechnology," *Medical and Biological Engineering*, vol. 5, pp. 271–293, 1967.

[5] A. Surowiec, S. Stuchly, J. Barr, and A. Swarup, "Dielectric properties of breast carcinoma and the surrounding tissues," *Biomedical Engineering, IEEE Transactions on*, vol. 35, pp. 257–263, 1988.

[6] S. R. Smith, K. R. Foster, and G. L. Wolf, "Dielectric Properties of VX-2 Carcinoma Versus Normal Liver Tissue," *Biomedical Engineering, IEEE Transactions on*, vol. BME-33, pp. 522 –524, 1986.

[7] D. Haemmerich, S. T. Staelin, J. Z. Tsai, S. Tungjitkusolmun, D. M. Mahvi, and J. G. Webster, "In vivo electrical conductivity of hepatic tumours," *Physiological Measurement*, vol. 24, pp. 251–263, 2003.

[8] G. C. Scott, M. L. G. Joy, R. L. Armstrong, and R. M. Henkelman, "Measurement of nonuniform current density by magnetic resonance," *Medical Imaging, IEEE Transactions on*, vol. 10, pp. 362–374, 1991.

[9] R. Yoon, T. DeMonte, K. Hasanov, D. Jorgenson, and M. Joy, "Measurement of thoracic current flow in pigs for the study of defibrillation and cardioversion," *Biomedical Engineering, IEEE Transactions on*, vol. 50, pp. 1167 –1173, 2003.

[10] K. Beravs, D. White, I. Sersa, and F. Demsar, "Electric current density imaging of bone by MRI," *Magnetic Resonance Imaging*, vol. 15, pp. 909 – 915, 1997.

[11] K. Beravs, A. Demsar, and F. Demsar, "Magnetic resonance current density imaging of chemical processes and reactions," *Journal of Magnetic Resonance*, vol. 137, pp. 253 – 257, 1999.

[12] H. Gamba and D. Delpy, "Measurement of electrical current density distribution within the tissues of the head by magnetic resonance imaging," *Medical and Biological Engineering and Computing*, vol. 36, pp. 165–170, 1998.

[13] H. R. Gamba, R. Bayford, and D. Holder, "Measurement of electrical current density distribution in a simple head phantom with magnetic resonance imaging," *Physics in Medicine and Biology*, vol. 44, pp. 281–291, 1999.

[14] I. Sersa, K. Beravs, N. J. F. Dodd, S. Zhao, D. Miklavcic, and F. Demsar, "Electric current density imaging of mice tumors," *Magnetic Resonance in Medicine*, vol. 37, pp. 404–409, 1997.

[15] M. Joy, V. Lebedev, and J. Gati, "Imaging of current density and current pathways in rabbit brain during transcranial electrostimulation," *Biomedical Engineering, IEEE Transactions on*, vol. 46, pp. 1139–1149, 1999.

[16] M. L. G. Joy, G. C. Scott, and R. M. Henkelman, "In-vivo detection of applied electric currents by magnetic resonance imaging," *Magnetic Resonance Imaging*, vol. 7, pp. 89–94, 1989.

[17] G. C. Scott, M. L. G. Joy, R. L. Armstrong, and R. M. Henkelman, "Sensitivity of magnetic-resonance current-density imaging," *Journal of Magnetic Resonance*, vol. 97, pp. 235–254, 1992.

[18] M. Eyüboğlu, R. Reddy, and J. S. Leigh, "Imaging electrical current density using nuclear magnetic resonance," *Elektrik, Turkish Journal of Electrical Engineering and Computer Science*, vol. 6, pp. 201–214, 1998.

[19] C. Park, B. I. Lee, and O. I. Kwon, "Analysis of recoverable current from one component of magnetic flux density in MREIT and MRCDI," *Physics in Medicine and Biology*, vol. 52, pp. 3001–3013, 2007.

[20] S. Y. Lee, S. C. Lee, S. H. Oh, J. Y. Han, B. H. Han, and M. H. Cho, "Magnetic resonance current density image reconstruction in the spatial frequency domain," *SPIE*, vol. 5030, pp. 611–618, 2003.

[21] S. H. Oh, I. K. Chun, S. Y. Lee, M. H. Cho, and C. W. Mun, "A single current density component imaging by MRCDI without subject rotations," *Magnetic Resonance Imaging*, vol. 21, pp. 1023–1028, 2003.

[22] Y. Z. İder, O. Birgül, O. F. Oran, O. Arikan, M. J. Hamamura, and L. T. Muftuler, "Fourier transform magnetic resonance current density imaging (FT-MRCDI) from one component of magnetic flux density," *Physics in Medicine and Biology*, vol. 55, pp. 3177–3199, 2010.

[23] N. Zhang, "Electrical impedance tomography based on currrent density imaging," Master's thesis, University of Toronto, 1992.

[24] E. J. Woo, S. Y. Lee, and C. W. Mun, "Impedance tomography using internal current density distribution measured by nuclear magnetic resonance," *SPIE*, vol. 2299, pp. 377–385, 1994.

[25] O. Birgül and Y. Z. İder, "Use of magnetic field generated by the internal distribution of injected currents for electrical impedance tomography," in *Proceedings of the IX International Conference on Electrical Bio-impedance*, (Heidelberg, Germany), pp. 418–419, September 2007.

[26] O. Kwon, E. J. Woo, J.-R. Yoon, and J. K. Seo, "Magnetic resonance electrical impedance tomography (MREIT): simulation study of J-substitution algorithm," *Biomedical Engineering, IEEE Transactions on*, vol. 49, pp. 160 –167, 2002.

[27] O. Kwon, J.-Y. Lee, and J.-R. Yoon, "Equipotential line method for magnetic resonance electrical impedance tomography," *Inverse Problems*, vol. 18, pp. 1089–1100, 2002.

[28] O. Birgül, B. M. Eyüboğlu, and Y. Z. İder, "Current constrained voltage scaled reconstruction (CCVSR) algorithm for MR-EIT and its performance with different probing current patterns," *Physics in Medicine and Biology*, vol. 48, pp. 653–671, 2003.

[29] Y. Z. İder, S. Onart, and W. R. B. Lionheart, "Uniqueness and reconstruction in magnetic resonanceelectrical impedance tomography (MREIT)," *Physiological Measurement*, vol. 24, p. 591, 2003.

[30] M. S. Özdemir, B. M. Eyüboğlu, and O. Özbek, "Equipotential projection-based magnetic resonance electrical impedance tomography and experimental realization," *Physics in Medicine and Biology*, vol. 49, pp. 4765–4783, 2004.

[31] K. Hasanov, A. Ma, A. Nachman, and M. Joy, "Current density impedance imaging," *Medical Imaging, IEEE Transactions on*, vol. 27, pp. 1301–1309, 2008.

[32] Y. İder and O. Birgül, "Use of magnetic field generated by the internal distribution of the injected currents for electrical impedance tomography MREIT," *Elektrik, Turkish Journal of Electrical Engineering and Computer Science*, vol. 6, pp. 215–225, 1998.

[33] O. Birgül, B. M. Eyüboğlu, and Y. Z. İder, "Experimental results for 2D magnetic resonance electrical impedance tomography (MR-EIT) using magnetic flux density in one direction," *Physics in Medicine and Biology*, vol. 48, pp. 3485–3504, 2003.

[34] J. K. Seo, J.-R. Yoon, E. J. Woo, and O. Kwon, "Reconstruction of conductivity and current density images using only one component of magnetic field measurements," *Biomedical Engineering, IEEE Transactions on*, vol. 50, pp. 1121–1124, 2003.

[35] S. H. Oh, B. I. Lee, E. J. Woo, S. Y. Lee, M. H. Cho, O. Kwon, and J. K. Seo, "Conductivity and current density image reconstruction using harmonic Bz algorithm in magnetic resonance electrical impedance tomography," *Physics in Medicine and Biology*, vol. 48, pp. 3101–3116, 2003.

[36] Y. Z. İder and S. Onart, "Algebraic reconstruction for 3D magnetic resonanceelectrical impedance tomography (MREIT) using one component of magnetic flux density," *Physiological Measurement*, vol. 25, pp. 281–294, 2004.

[37] H. S. Nam, C. Park, and O. I. Kwon, "Non-iterative conductivity reconstruction algorithm using projected current density in MREIT," *Physics in Medicine and Biology*, vol. 53, pp. 6947–6961, 2008.

[38] U. Mikac, F. Demsar, K. Beravs, and I. Sersa, "Magnetic resonance imaging of alternating electric currents," *Magnetic Resonance Imaging*, vol. 19, pp. 845–856, 2001.

[39] S. H. Oh, B. I. Lee, E. J. Woo, S. Y. Lee, T. S. Kim, O. Kwon, and J. K. Seo, "Electrical conductivity images of biological tissue phantoms in MREIT," *Physiological Measurement*, vol. 26, pp. S279–S288, 2005.

[40] C. Park, B. I. Lee, O. Kwon, and E. J. Woo, "Measurement of induced magnetic flux density using injection current nonlinear encoding (ICNE) in MREIT," *Physiological Measurement*, vol. 28, pp. 117–127, 2007.

[41] M. J. Hamamura, L. T. Muftuler, "Fast imaging for magnetic resonance electrical impedance tomography," *Magnetic Resonance Imaging*, vol. 26, pp. 739–745, 2008.

[42] L. T. Muftuler, G. Chen, M. J. Hamamura, and S. H. Ha, "MREIT with SENSE acceleration using a dedicated RF coil design," *Physiological Measurement*, vol. 30, pp. 913–929, 2009.

[43] Y. Q. Han, Z. J. Meng, W. C. Jeong, Y. T. Kim, A. S. Minhas, H. J. Kim, H. S. Nam, O. Kwon, and E. J. Woo, "MREIT conductivity imaging of canine head using multi-echo pulse sequence," *Journal of Physics: Conference Series*, vol. 224, no. 1.

[44] D. C. Ghiglia, and M. D. Pritt, *Two-Dimensional Phase Unwrapping: Theory, Algorithms and Software*. Wiley-Interscience, New York, 1998.

[45] A. J. Davies, *The finite element method - A first approach*. Clarendon Press, Oxford, 1980.

[46] A. N. Brooks and T. J. R. Hughes, "Streamline upwind/Petrov-Galerkin formulation for convection dominated flows with particular emphasis on the incompressible navier-stokes equation," *Computer Methods in Applied Mechanics and Engineering*, vol. 32, pp. 199–259, 1982.

[47] B. J. Roth, N. G. Sepulveda, and J. P. Wikswo, "Using a magnetometer to image a two-dimensional current distribution," *Journal of Applied Physics*, vol. 65, pp. 361–372, 1989.

[48] O. C. Zienkiewicz, R. L. Taylor, and P. Nithiarasu, *The Finite Element Method for Fluid Dynamics*. Elsevier Butterworth-Heinemann, Oxford, 2005.

[49] P. Knobloch, "On the choice of the SUPG parameter at outflow boundary layers," *Advances in Computational Mathematics*, vol. 31, pp. 369–389, 2009.

[50] T. H. Lee, H. S. Nam, M. G. Lee, Y. J. Kim, E. J. Woo, and O. I. Kwon, "Reconstruction of conductivity using the dual-loop method with one injection current in MREIT," *Physics in Medicine and Biology*, vol. 55, pp. 7523–7539, 2010.

[51] H. J. Kim, Y. T. Kim, A. Minhas, W. C. Jeong, E. J. Woo, J. K. Seo, and O. Kwon, "In vivo high-resolution conductivity imaging of the human leg using MREIT: The first human experiment," *Medical Imaging, IEEE Transactions on*, vol. 28, pp. 1681–1687, 2009.

[52] O. F. Oran and Y. Z. İder, "Triangular mesh based MRCDI and MREIT," in *Proceedings of Workshop on MR-based Impedance Imaging, co-sponsored by the IEEE EMBS and endorsed by the ISMRM*, (Seoul, Korea), p. 19, December 2010.

[53] R. J. Wijngaarden, K. Heeck, H. J. W. Spoelder, R. Surdeanu, and R. Griessen, "Fast determination of 2D current patterns in flat conductors from measurement of their magnetic field," *Physica C: Superconductivity*, vol. 295, pp. 177 – 185, 1998.

[54] A. Sezginer, "The inverse source problems of magnetostatics and electrostatics," *Inverse Problems*, vol. 3, pp. L87–L91, 1987.

[55] P. Pesikan, M. L. G. Joy, G. C. Scott, and R. M. Henkelman, "2-dimensional current density imaging," *Instrumentation and Measurement, IEEE Transactions on*, vol. 39, pp. 1048–1053, 1990.

[56] L. Özparlak and Y. Z. İder, "Induced current magnetic resonance electrical impedance tomography," *Physiological Measurement*, vol. 26, pp. S289–S305, 2005.

[57] O. F. Oran and Y. Z. İder, "Magnetic resonance electrical impedance tomography (MREIT) based on the solution of the convection equation using FEM with stabilization." submitted to *Physics in Medicine and Biology*, June 2011.

[58] Y. Z. İder and O. F. Oran, "3D FT-MRCDI: Phantom experiments," in *Proceedings of Workshop on MR-based Impedance Imaging, co-sponsored by the IEEE EMBS and endorsed by the ISMRM*, (Seoul, Korea), p. 14, December 2010.